Novel Engineering and Characterization of Sensing Materials and Fluidic Devices for Neuroscience

Melissa Hexter

A thesis submitted in accordance with the requirements For the Degree of Doctor of Philosophy at Imperial College London

Department of Bioengineering

Imperial College London

May 2023

Declaration of Originality

I, Melissa Hexter, declare that the original scientific content in this thesis is my own, unless otherwise stated or referenced. Experimental work or data analysis that was done in collaboration with others is acknowledged within the text and figure captions. The work presented in this thesis was performed at Imperial College London.

Copyright Declaration

Abstract

Many aspects of neurophysiology such as the pathophysiology of neuropsychiatric illness remain unclear due to challenges in non-invasively probing the brain while considering its chemical and physical heterogeneity. Further investigation of the neurochemicals responsible for neuropsychiatric illness, as indicated by the monoamine hypothesis of depression, is therefore limited without addressing these obstacles. The Hashemi lab studies these neurotransmitters and develops translational tools to minimize challenges associated with *in vivo* analysis while maximizing the predicative power of in *vitro* models of the brain. The work in this thesis furthers our understanding of the behaviour of carbon fiber micro-electrodes for serotonin measurement and the fluid dynamics of FSCV measurements. This information is critical for the acquisition of physiologically relevant measurements from translational models of neuropsychiatric illness. In this thesis, I begin by reviewing techniques that have been developed to monitor neurotransmitters in **Chapter 1**. Next, in **Chapter 2**, I outline the specific methods used to collect measurements with FSCV/FSCAV and to construct the electrodes and fluidic devices characterized in this work. In **Chapter 3**, I establish a design criterion for the development of fluidic devices for FSCV measurements. I then use this criterion to design a flow cell for FSCV measurements and challenge its reproducibility and stability. This work enabled the validation of the analyte specific decay and variability of CFMEs. **Chapter 4** introduced a simple and inexpensive fabrication protocol for a versatile carbon-based electrode with excellent electrochemical kinetics and sensitivity for serotonin measurements with FSCV. After characterizing the performance of this electrode, it was integrated into a simple polydimethylsiloxane (PDMS) based device to provide a preliminary platform for the optimization of measurements from cells using FSCV **(Chapter 5)**. This work identified adhesion, dead space, electrode geometry, and material rigidity as key parameters in the design of a microfluidic device with an incorporated capacity for FSCV measurements. **Chapter 6** concludes the thesis and highlights the future implications of the work.

 In sum, this work offers novel tools for characterizing sensors for FSCV measurement and a concept for a microfluidic device capable of sensor calibration and measurement from patient-specific in *vitro*

models of the brain. This type of analytical platform would permit the characterization of neurotransmission for preclinical pharmacological screening and/or elucidation of personalized therapies for neuropsychiatric illness.

Table of Contents

List of Figures

List of Tables

List of Abbreviations

CPE..Carbon Paste Electrode

CFME...Carbon Fiber Micro-Electrode

5HT..Serotonin (5-Hydroxytryptamine)

CV...Cyclic Voltammogram

DA...Dopamine

FSCV...Fast-Scan Cyclic Voltammetry

FSCAV...Fast-Scan Controlled Adsorption Voltammetry

FIA..Flow Injection Analysis

GPCR...G-Protein Coupled Receptor

fMRI...Functional Magnetic Resonance Imaging

PET...Positron Emission Tomography

NIR...Near Infrared Spectroscopy

PBP...Periplasmic Binding Protein

HPLC..High Performance Liquid Chromatography

LINC..Laser Induced Nano-Carbon

PEDOT:PSS..............................poly(3,4-ethylenedioxythiophene) polystyrene sulfonate

PEI..Polyethylenimine

CNT...Carbon Nanotubes

3-MT...3-Methoxytyramine

PAN...Polyacrylonitrile

iPSCs...Induced Pluripotent Stem Cells

PBS...Phosphate Buffered Saline

CMOS..Complementary Metal Oxide Semi-Conductor

PEEK...Polyetheretherketone

PDMS...Polydimethylsiloxane

SLA...Stereolithography

RMSE...Root Mean Square Error

ANOVA...Analysis of Variance

Re...Reynolds

Pe...Peclet

PI...Polyimide

PMMA……………………………………………………………………………………..Polymethylmethacrylate

SEM…………………………………………………………………………………Scanning Electron Microscopy

FDM………………………………………………………………………………….Fused Deposition Modeling

Acknowledgments

I would like to start by thanking my supervisor, Dr. Parastoo Hashemi, for taking a chance on me and giving me the opportunity to move across the world, build a new life, and grow into a better human being. You have always been supportive of my research ideas, my powerlifting, and most importantly, my personal development.

Next, I would like to thank the members of the Hashemi lab for supporting me every day through the rollercoaster that is my life. More specifically, thank you to Sergio, with whom I have shared most of my work, and who has always had invaluable patience with me in our friendship and in our research. Thank you to Lauren, who has always been loving, kind, willing, sends the cutest animal content I've ever received, and is an amazing listener. Thank you to Brenna, for our life saving coffee runs, tolerating every part of me, and being there for some of my darkest moments. Thank you to Bea, for your impeccable life advice and therapy sessions, your positive attitude, and for including me in all your exciting new work. Finally, thank you to Bettina, for keeping me company in the office on late evenings, and always being a supportive friend and colleague.

I would also like to thank members of the bioengineering department that have supported me along my PhD journey. I'd like to thank Joel, Larry, Paschal, Niraj, Florent, and Joseph. I can't forget about the amazing friends I've made along the way that have made me feel more at home in a foreign country than in Baltimore. Thank you, Gabe, Alex, Ghazel, Devyani, Louis, Sameer, Ramsay, Ellie, Patri, Victor, Julia, Carmel, Elena, Ben, Christy, and Jessica.

Finally, I would like to thank my family: my sister, my mother, my father, Elizabeth, Shelbi, Linda, and Wayne. I would not have survived these years without you. You are all the apple of my eye and my love for you is infinite.

Chapter 1 – Introduction

1.1 Tools to Probe the Brain

The brain is extremely difficult to probe when considering its physical intricacy, chemical complexity, and density of simultaneous processes. This challenge has led to many of its mechanisms and pathologies remaining widely unknown despite advances in sensing tools. The physiology of mental illnesses, such as depression, which affects more than 280 million people globally[1], is an example of one of these poorly understood pathologies. Furthermore, existing antidepressant treatments are only 20-30% more effective in reducing symptoms than placebo[2], highlighting an unmet clinical need. Optimization of sensing technology and the introduction of effective translational models to elucidate the chemical pathways of depression is essential to begin addressing this unmet clinical need.

The monoamine hypothesis of depression implicates a deficiency in norepinephrine, dopamine, and serotonin as the primary culprits of depressive symptoms based on pharmacological studies [3]. More recent work suggests the role of inflammatory responses *via* histamine, also a neurotransmitter, in the onset of depression. An array of non-genetic and genetic sensing techniques has been developed to further understand the dynamics and transport characteristics of these neurotransmitters in the context of depression. Genetic sensing techniques employ cellular machinery to express proteins of interest coupled to an optical reporter that is activated when the target analyte binds to the expressed protein. Non-genetic methods include microdialysis, electrophysiology, non-genetic optical imaging and electrochemistry, which are outlined below.

Microdialysis:

Historically, microdialysis was the technique of choice for monitoring neurotransmitters because of the selectivity provided by a semipermeable membrane and coupling to other analytical techniques. Microdialysis involves continuous sampling of the extracellular space *via* perfusion of physiological buffer causing passive diffusion of extracellular analytes into the dialysis probe for downstream analysis. Microdialysis is often paired with powerful analytical techniques such as capillary

electrophoresis[4] and liquid chromatography[5] to permit further separation of the dialysate with nanomolar to picomolar sensitivity. While advantageous, microdialysis does not have the temporal resolution to monitor neurotransmission in real time because of the time required for diffusion of the analyte into the probe for sampling. Furthermore, microdialysis probes are too large[6] to monitor the dynamic local concentrations of neurotransmitters from single neurons or small neuron populations. The size of the microdialysis probe also causes local tissue damage that may result in changes in neurotransmission that do not reflect homeostasis.

Electrophysiology:

Electrophysiological methods typically measure the electrical activity of a single neuron with a single micropipette electrode or multiple neurons with an electrode array. These micropipette electrodes are usually fabricated with a wire surrounded by an electrolyte solution such as saline. Electrophysiological measurements have single-cell spatial resolution, sub-second temporal resolution, and quantify either the change in membrane voltage or current in response to cell activation. Electrophysiology causes minimal damage to cells with picoampere sensitivity but does not have the specificity to determine the ligand responsible for electrical excitation. Specificity may be investigated by isolating specific types of neurons[7],[8] and/or with pharmacological validation [9]. Additionally, electrophysiological measurements are highly sensitive to the collection environment (i.e. vibrational and mechanical noise) and are therefore tedious to set up.

Optical Methods:

Optical methods harness optically active or radioactive probes to replace neurotransmitters [10], complex with relevant receptors[11], and/or interact with endogenous neurotransmitters[12] to indicate neurotransmission. Optical probes can be engineered genetically to target specific cell types, or non-genetically to avoid challenges associated with the control of gene expression[13] and off-target effects that may impact experimental viability[14]. Non-genetic optical methods require diffusion-based uptake of an optical reporter into surrounding tissues for imaging with techniques such as fMRI [12], PET[11],

NIR[15], and high-resolution microscopy. Non-genetic reporters include fluorescent dyes [16], radiolabelled drugs[11] or peptides, and engineered cells[17]. Genetic reporters are characterized by an encoded fluorescent protein (intensiometric) or protein pair (ratiometric) complexed to either a GPCR (G-protein coupled receptor) [18] or a PBP (periplasmic binding proteins) [19] that binds the targeted neurotransmitter. Optical reporters are less physically invasive than electrodes and microdialysis probes but may cause immunogenicity[17] in non-genetic cell-based probes or result in disrupted cellular function in the case of genetic reporters[20]. Furthermore, while optical probes may cause less tissue damage than microdialysis, optical imaging of the brain *via* microscopy, primarily used in optogenetic methods for its excellent and spatial temporal resolution, requires direct imaging that demands tissue excising. Other imaging techniques such as fMRI, PET, and NIR are less invasive but suffer from poorer spatial resolution, measuring in the mm to cm range [21].

Electrochemical:

Electrochemical monitoring of the brain using voltammetry was first performed with a glassy carbon electrode to measure oxygen in 1965 [22] followed by carbon paste electrodes with chronoamperometry and cyclic voltammetry to measure neurotransmitters in the 1970s[23, 24]. Similarly to electrophysiology, electrochemistry may be performed with excellent spatial and temporal resolution. However, electrochemical methods differ from electrophysiology in that the measured current is a result of a faradic reaction rather than the activation of a cell, therefore it is not possible to directly measure analytes that do not undergo electrochemistry. For electroactive analytes, electrochemical methods provide an element of specificity by distinguishing analytes by their redox potential. Where analytes cannot be distinguished by redox potentials using amperometry, voltammetry is preferred. Voltammetry allows the user to consider the kinetics of the reaction of interest to select a scan rate, scan limits, and waveform shape to improve specificity. While not as specific as voltammetry, amperometry has superior temporal resolution because the electrode is held at a constant potential which eliminates the time required to scan through potentials to apply a waveform. Balancing the needs for specificity and temporal resolution led to the development of fast

scan cyclic voltammetry in the 1980s [25]. Since then, fast scan cyclic voltammetry (FSCV) has been

adopted to make physiologically relevant measurements of neurotransmission *in vivo*[26-29].
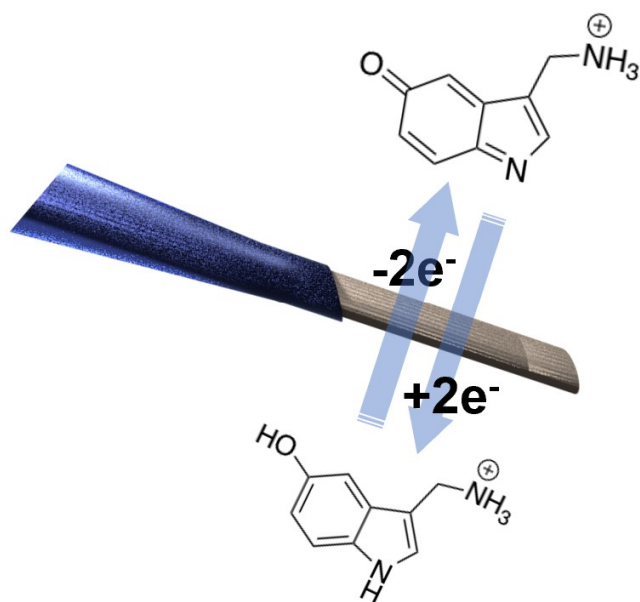
Figure 1

illustrates the two-electron oxidation of serotonin at a carbon fiber microelectrode (CFME)

1.2 Fast Scan Cyclic Voltammetry

Fast-scan cyclic voltammetry (FSCV) at carbon fiber microelectrodes (CFMEs) is an electroanalytical

technique adapted for the quantification of neurotransmission. FSCV possesses excellent temporal

resolution and better chemical selectivity than amperometry *via* the chemical signature provided by

the features of a cyclic voltammogram. FSCV measurements are multi-dimensional and provide both

cyclic voltammograms and current versus time plots, which are superimposed onto each other in

three-dimensional false colour as illustrated in Figure 2. Acquisition parameters such as the scan rate,

waveform application frequency, and holding potential allow the opportunity for analyte specific

optimization[30]. Fast scan rates kinetically limit undesirable reactions from occurring while permitting

rapid reactions such as the oxidation of serotonin or dopamine at the surface of the electrode.

Additional selectivity and sensitivity can be offered by functionally modifying the surface of the electrode with polymers[31] or renewing the surface of the electrode with oxidative etching[32].
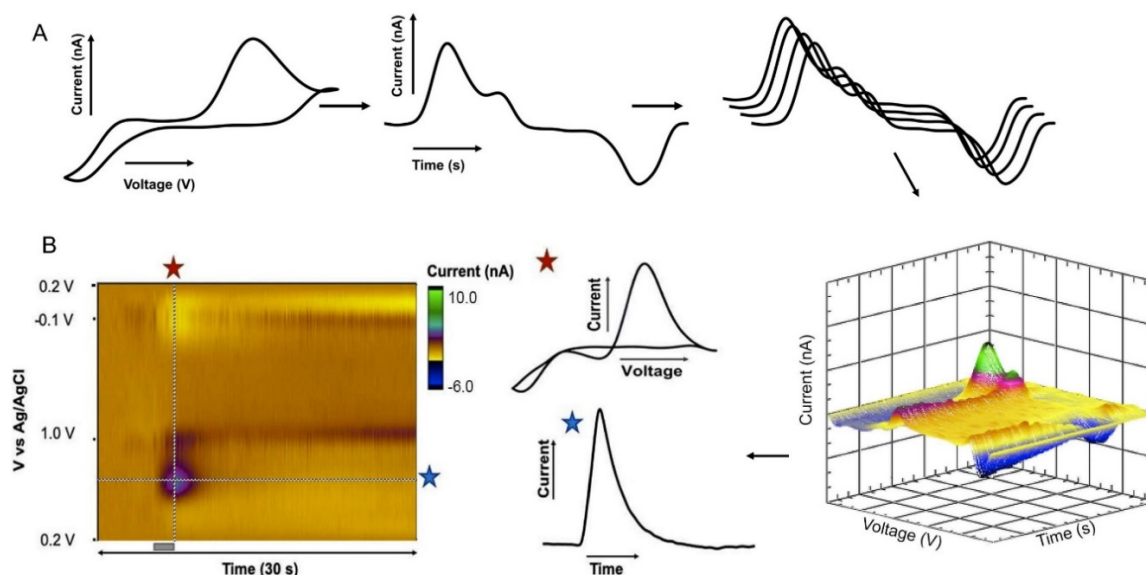
Figure 2

Shows (A) a cyclic voltammogram in current (y-axis) versus voltage (x-axis) that is then modified to (B) where time is on the x-axis, voltage is on the y-axis, and current is illustrated in false colour to create a "colour plot". This type of plot can be sliced vertically (as indicated by the red star) to yield a conventional cyclic voltammogram or horizontal (as indicated by the blue star) to generate a current versus time plot.

Unlike conventional cyclic voltammetry, FSCV can only quantify changes in analytes, which is fit for purpose because neurotransmission is a dynamic process that isn't appropriately described with tonic measurements alone. The fast scan rates of FSCV generate large charging currents that comprise the majority of measured current. This necessitates background subtraction to reveal the current created by the interaction of the analyte with the electrode. FSCV is performed with microelectrodes, typically CFMEs, that minimize tissue damage and inflammatory responses that may skew experimental results[33]. Furthermore, microelectrodes eliminate the requirement for a counter electrode because the generated currents are too small to compromise the stability of the reference electrode on the timescale of FSCV measurements.

FSCV has contributed to clinically relevant discoveries in neuroscience *via* its capacity to measure the dynamics of neurotransmission. For example, the dopamine transporter was discovered to be the target for psychostimulants as quantified by *in vivo* FSCV in rats[27]. Additionally, FSCV has characterized the sub-second release of dopamine prior to the administration of dopaminergic drugs, which revolutionized clinical strategies to treat addiction[34]. More recently, the development of FSCV to detect histamine revealed the mechanistic role of histamine in the inhibition of serotonin release [35]. FSCV may also be coupled with other techniques to address data acquisition challenges[36], provide complementary information [37], or to validate new techniques for the dynamic monitoring of neurotransmission [38].

1.3 FSCAV

FSCAV was developed to study diffusion-controlled adsorption of analytes to the electrode and to complement phasic measurements collected with FSCV with tonic quantifications of extracellular neurotransmitters[39]. FSCAV is a three-step technique using the principles of stripping voltammetry where the adsorption kinetics of the analyte are optimized to preconcentrate the analyte at the electrode surface prior to measurement. In FSCAV, a waveform is applied at high frequency to strip the electrode of analyte followed by a switch to constant potential to allow adsorption of the analyte on the electrode surface to reach equilibrium. Finally, the waveform is reapplied, and the first few CVs contain information rich measurements that are processed to permit quantification of the target analyte. FSCAV allows quantification of target analyte *via* integration of the CV to calculate charge, which is then related to concentration with calibration[40].

Though the technique has only existed since 2013, FSCAV is already responsible for significant physiological findings through quantification of tonic serotonin and dopamine. For example, FSCAV has been performed in parallel with FSCV to conclude that the efficacy of SSRIs is reduced in the presence of histamine based neuroinflammation[35]. FSCAV has also revealed that induced pain elicits

changes in dopaminergic tone highlighting the contribution of dopamine dysregulation in chronic pain[41].

1.4 Carbon

Carbon-based sensors have become a popular material for a range of electrochemical applications because of their wide potential window[42], versatile surface for functionalization[33, 43], biocompatibility[44], and low-cost. The fast electron transfer kinetics and optimized analyte adsorption necessary for FSCV of neurotransmitters can be achieved with the appropriate carbon material[45]. The electrochemical performance of a carbon material is heavily influenced by its physical structure and anisotropic orientation. More specifically, interplanar spacing, carbon atom hybridization, and defect prevalence are structural properties that define electrochemically relevant features like conductivity. FSCV of neurochemicals has been performed with graphite (sp2 hybridized) and diamond (sp3 hybridized) based materials[46], but CFMEs, (graphitic material), are predominantly used because of their excellent chemical properties and suitability for *in vivo* experiments[47]. Carbon composite, typically carbon paste, and pyrolytic carbon films are other graphite-based materials that have been investigated for FSCV[45] to address the disadvantages of CFMEs for *in vitro* applications[48].

CFMEs

Cylindrical carbon fibers are mechanically extruded precursor fibers, usually polyacrylonitrile (PAN), that are heat treated to pyrolytic temperatures for carbonization. This unique process exploits carbon's anisotropy to orient the a-axis (basal plane) of the graphene layers along the length of the cylinder and the c-axis (edge plan) at the circular base. This maximizes the low resistivity of the a-axis while exposing the c-axis for improved electron transfer kinetics and adsorption[49]. To fabricate CFMEs, the fibers are then sealed into a glass capillary and trimmed to expose the cylindrical fiber, or cut, epoxied, and bevelled to form a disk electrode where planar diffusion is preferred. CFMEs generate less noise per electroactive area and provide better sensitivity than bevelled disks[50]. Additionally, CFMEs are spatially and mechanically fit for sensing in *vivo* because the rigidity of the

glass allows penetration of tissue while the small diameter (7-10 microns) and flexibility of the fibers minimize localized inflammation that may perturb measurements. For *in vitro* applications, CFMEs are not ideal because they are tedious to make, fragile, and difficult to integrate into microfluidic devices and cell cultures. Furthermore, hemispherical diffusion characteristic to CFMEs is more likely to expose the electrode to more than targeted single cell secretions.

CFMEs are often exposed to surface modifications such as overoxidation or coating with polymers to improve the sensitivity or selectivity of the electrode for the target analyte [44]. Signal enhancing overoxidation can be achieved *via* flame-etching or electrochemical etching[32, 51, 52]. Negatively charged polymers such as Nafion may be electrodeposited onto the surface of CFMEs to preconcentrate local positively charged catecholamines for FSCV detection[53]. Anionic exchange polymers poly(3,4-ethylenedioxythiophene) polystyrene sulfonate (PEDOT:PSS) and polyethylenimine (PEI) modify electrode surfaces for sensing of negative analytes like 3-methoxytyramine (3-MT), a dopamine metabolite [31].Other common modifications include activation via laser ablation or addition of carbon nanotubes (CNT) to improve selectivity and sensitivity[43, 54].

Other Carbon Materials for FSCV

Carbon composite electrodes, usually, polycrystalline graphite with a binder, are an attractive alternative because they have low background current, are simple to prepare, and easily miniaturized and modified[55]. Despite these advantages, composite electrodes have heterogenous charge densities due to graphite islands resulting in slow electron transfer kinetics[56]. These properties may be acceptable for certain slow scan voltametric applications[57], but not for FSCV. Recent developments in thermoplastic-based carbon composites are promising[58].but still do not have proven compatibility with FSCV.

Pyrolysed substrates that form electroactive graphitic films are another opportunity for versatile microfabrication of FSCV electrodes. Pyrolysis of polymer substrates such as SU-8 photoresist can occur via heat treatment above 900˚C or laser photothermal transformation. Heat pyrolysis requires

thermally stable substrate carriers like silicon, which limits the potential for integration with flexible materials often used in microfluidics. Laser induced carbon is preferred where flexibility of substrate materials is required. Laser-induced nano-carbon (LINC) electrodes can be produced from substrates such as paralyne-C [59] and polyimide [60], and have already been developed for FSCV of neurotransmitters *in vitro* [61] and *in vivo* [62].

1.5 Calibration

Calibration of electrodes is necessary to generate physiologically relevant concentration of analytes *via* measured current[63]. FSCV calibration is performed with flow injection analysis (FIA) to mimic the dynamic changes in analytes that occur *in vivo*. Because calibration can't be performed *in vivo*, buffer solutions representative of physiological fluids are used to minimize error in current prediction generated by changing matrices. During FIA, the electrode is placed in a flow cell where a bolus of sample is introduced to the electrode at a specified time with an injection switching mechanism. A switching mechanism that does not significantly perturb the electrode response can be achieved with appropriate valving (air actuator[32], HPLC valve [48]) or fluidic control[64]. Calibration of CFMEs with FIA for FSCV is not standardized and the variability of in-house made flow cells render it a tedious process. This has led to the use of generalized calibration factors[65] or single-point calibrations [66] instead of performing multi-point calibrations for each electrode. Generalized calibration factors are particularly problematic because CFMEs are hand-fabricated so individual electrode responses vary both in sensitivity and stability. Furthermore, the electrode response is analyte specific [66], varies with chemical matrix [67], and exhibits range-dependent linearity[53].

The mass transport of the analyte to the electrode significantly impacts the reliability of electrode calibration, which requires optimization of fluid dynamics in the design of the flow injection system. Ideally, a flow injection system can reproducibly generate a square-like injection of sample resulting in a signal that indicates that the electrode has reached a steady state. A steady-state response indicates that the reaction of the electrode with the analyte has reached equilibrium and is therefore

suitable for collection. In early systems, the end of HPLC tubing functioned as the flow cell, but this simple configuration led to variation in the electrode response due to irreproducible positioning of the electrode in the tubing (Figure 3A) [68]. Since then, this configuration has been adapted to HPLC fittings (Figure 3B)[69], but still suffers leaks and difficulties in integration with the CFME. These issues have been addressed with microfluidic solutions (Figure 3C-D)[64, 70], but standardization of calibration has not yet been achieved. Other important fluid-controlled parameters include the electrode response time within the FSCV acquisition window and the volumes of used reagents, which has led to the use of microfluidics in FSCV calibration.
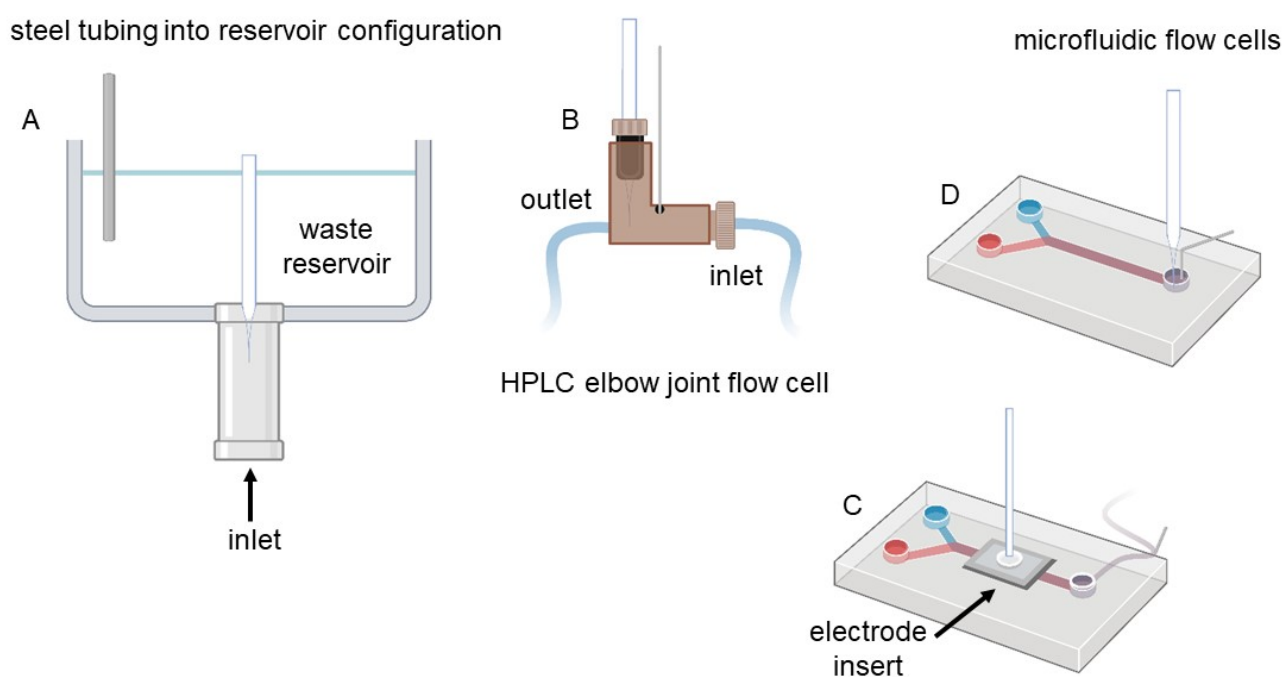
Figure 3

    (A) Earliest flow cell configuration where the electrode is lowered into a steel tube that is integrated into a waste reservoir and connected to inlet tubing. (B) HPLC elbow joint flow cell with electrode integrated into a compatible fitting. Holes are drilled for the outlet and reference electrode. (C) Semi-open microfluidic flow cell with on chip dilution (D) Microfluidic flow cell with electrode integrated into an insert.

1.6 Microfluidics with Carbon-Based Sensors

Microfluidic devices with seamlessly integrated carbon electrodes are a powerful analytical platform for a variety of applications because of the advantages offered by combining microfluidics with the versatility of carbon electrodes. The direct integration of carbon electrodes within microfluidic channels permits the precise control of fluid flow, efficient mixing, and the potential for automation. Carbon is also easily modified with nanoparticles[71] and polymers[72] to enhance electrochemical detection. Such devices are most commonly coupled with amperometry to detect small molecules, such as dopamine[72, 73], or large molecules such as antibodies[71]. Some platforms have also been optimized for cyclic voltammetry[74] and square wave voltammetry[75], but none have been integrated with FSCV. Previously designed microfluidic devices for FSCV require manual implementation of fragile CFMEs into the device[64, 70] indicating an unmet need for hassle-free integration. Microfluidic platforms with integrated carbon-based sensors have been primarily focused on calibration or offline detection from perfused fluids. Microfluidic chips encompassing direct electrochemical analysis from cells has predominantly been performed with platinum or platinum-modified electrodes[76] to measure oxygen. The literature would benefit from the exploration of a wider range of analytes from microfluidic devices with integrated cell cultures, which may be permitted by the versatility of carbon.

1.7 Translational Models

Monitoring the brain with FSCV *in vivo* is currently only possible in animal models due to the invasiveness of the technique. Other, less-invasive techniques such as fMRI are not suitable to monitor dynamic neurotransmission, therefore it would be clinically powerful to create a translational model of the brain to enable FSCV measurements in a human context. Translational models for the brain have been made possible by protocols to transform somatic cell types such as dermal fibroblasts into induced pluripotent stem cells (iPSCs) [77]. These cells can then be differentiated into neurons, glia, and progenitor cells that self-assemble into structures, known as organoids, that function similarly to developing brain tissue[78]. Brain organoids may also be engineered to recapitulate psychiatric

pathologies such as Parkinson's disease and schizophrenia[79]. Furthermore, organoids recapitulate donor specific features, which creates an opportunity for precision/personalized medicine tools [80].

Translational models of Parkinson's disease using human midbrain organoids have been electrochemically probed for dopamine as proof of concept for drug screening in Parkinson's patients[81]. A similar approach could be applied for the development of a serotonin-based precision medicine platform for depression patients. Recently, a voltammetrically validated model of serotonin neurotransmission was developed that shows promise as a precision medicine tool and preclinical screening tool[82]. This single cell-type model maintained many features of serotonin neurotransmission observed *in vivo* but suffered differences in evoked signal amplitude and response to pharmacological treatment, indicating the need for a more representative model. More complex models with greater functionality are difficult to culture because of imprecise control over environmental cues for regionalization and maturation and issues with supply of oxygen and nutrients due to the lack of vascularization. These challenges can be addressed with microfluidic devices that improve microenvironment control and introduce flow to enhance medium turnover mimicking tissue vascularization[83]. Microfluidic platforms can also be implemented to streamline organoid assembly and proliferation providing the potential for upscaling to commercialization [78].

1.8 Scope of Dissertation

This thesis addresses problems with the calibration of FSCV and proposes a concept for an integrated platform for measuring neurotransmission for translational models of neurotransmission.

Chapter 2

This chapter describes the methods used to perform FSCV, FSCAV, and to fabricate the fluidic devices and electrodes.

Chapter 3

This chapter reflects a published article introducing a novel flow cell for easy and reproducible measurements with CFMEs for FSCV.

Chapter 4

Here I introduce a novel fabrication protocol for a carbon-based electrode capable of integration with a microfluidic device.

Chapter 5

This chapter reviews the development of a microfluidic platform with an integrated carbon sensor for easy calibration and direct sensing from cell culture.

Chapter 6

This conclusion chapter will highlight the major findings of this research. First, creating a standardized protocol for calibration of CFMEs for FSCV *in vitro*. Next a method for the fabrication of a novel carbon-based electrode will be explored. Finally, this work exhibits the foundation for an integrated platform for direct measurement of neurotransmission from *ex vivo* models of the brain. Furthermore, this research has elucidated the key parameters for sensor development and calibration for FSCV for future research to build upon. This chapter will also discuss future directions.

Chapter 2 – General Methods

2.1 Introduction

This chapter discusses the general methods used in the experiments performed in this thesis. These methods summarize the equipment, reagents, and fabrication protocols used for this work. More specific methods relevant to a given set of results will be discussed alongside the results of the relevant chapter. Furthermore, the specific methods used to create every unsuccessful design configuration of the laser induced carbon electrodes used in **Chapter 4** are not discussed in this chapter for brevity.

2.2 Electrochemical Methods

Fast-Scan Cyclic Voltammetry (FSCV)

All voltammetry was performed with a two-electrode system with a carbon-based working electrode (either CFME or carbon composite) and an Ag/AgCl pseudo-reference. The pseudo-reference was created by chloridizing an Ag wire (A-M systems, WA, USA) for 30 s in 0.1 M HCl at 5 V. FSCV was performed using a Pine Research head stage (Pine Research Instrumentation, Durham, NC, USA) connected to a potentiostat (Dagan Corporation, Minneapolis, MN, USA). The potentiostat was controlled by the WCCV 3.06 software (Knowmad Technologies LLC, Tucson, AZ, United States) via a USB-6431 DAC/ADC (National Instruments, TX, USA) device. Data was smoothed and treated using a Butterworth filter and a 5 kHz low-pass filter. For pre-treatment of the electrode during flow cell calibrations, an extended triangular waveform[84] scanning from 0.2 to −0.1 to 1.3 to 0.2 V, at a scan rate of 1000 V/was applied at 60 Hz for 10 min and then 10 Hz for 10 min in the physiological salts buffer with 1 μM L-glutamic acid. The waveform was then switched to the Jackson waveform[30], illustrated in Figure 4, and cycled at 60 Hz for 10 min and then 10 Hz for 10 min for a total of 40 min of cycling to permit the electrode to acclimate to the chemical environment.
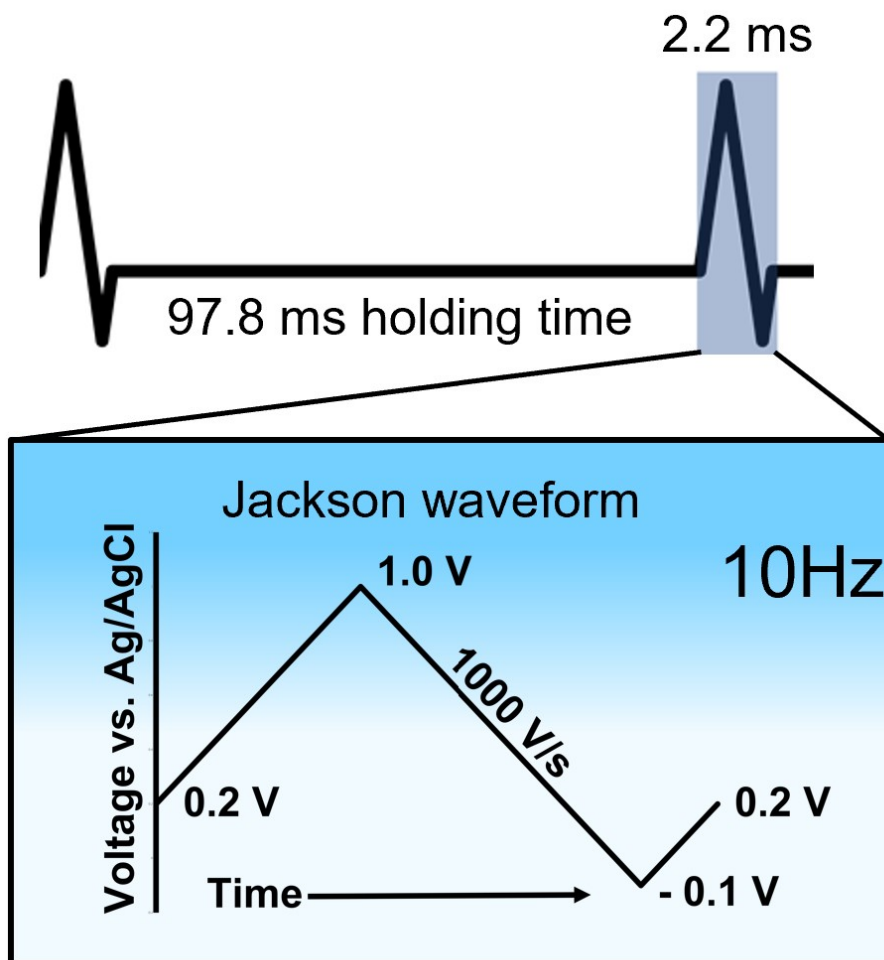
Figure 4

Illustrates the shape of the Jackson waveform and its 2.2 millisecond application period during each application cycle. Between each application of the waveform, a holding period of 97.8 milliseconds at 0.2V is executed.

Fast-Scan Controlled-Adsorption Voltammetry (FSCAV)

FSCAV was performed with CFMEs coated with Nafion using a CMOS precision analog switch, ADG419 (Analog Devices, Cambridge, MA, USA). This switch was coupled with a potentiostat (Dagan Corporation, Minneapolis, MN, USA) and the USB-6431 DAC/ADC (National Instruments, TX, USA) for waveform application with the WCCV 3.06 software (Knowmad Technologies LLC, Tucson, AZ, United States). The serotonin specific 'Jackson' waveform was applied at a frequency of 100 Hz for 2 seconds and then held at a potential of 0 V for 10 s followed by reapplication of the waveform until the total file collection time of 30 seconds. The third cyclic voltammograms following reapplication were used

for serotonin quantification *via* peak integration with the WCCV 3.06 software to determine charge. Data acquisition and treatment were performed the same as for FSCV.

Flow Injection Analysis (FIA)

The flow injection analysis system consisted of a syringe pump (Harvard Apparatus, MA, USA), in-house made flow cell, and six-port HPLC valve (VICI, Valco, Houston, TX, USA) with two configurations. Flow rates between 1–3 mL/min were explored during optimization of different flow cell iterations. The final flow cell functioned best with a flow rate of 1.7 mL/min to reduce the reagent used and rise time of the sample plug while minimizing tailing. Injection times between 5 seconds and 15 seconds were attempted, but the ideal injection was achieved with a 10 second injection time. 1mL volumes of sample from a 5mL syringe were introduced into the system with each injection. The ideal sample loop tubing was 22 in., the inlet Polyetheretherketone (PEEK) tubing length was 6 in., and the tubing inner diameter was 0.04 in. (Restek, PA,USA). This sample loop size guaranteed that the sample plug was long enough to reach a steady state. These parameters were optimized for this particular tubing size. Other sample loop lengths and inlet tubing lengths were investigated while building the FIA system.

Nafion Electrodeposition

Nafion was electrodeposited for on the exposed carbon fiber surface via application of a constant potential of 1.0 V vs. a pseudo-Ag/AgCl reference electrode for 30 seconds. The resulting microelectrode was dried at 70 °C for 10 min and stored for a minimum of 24 h before use[53].

Solutions

Stock solutions of serotonin HCL and L-ascorbic acid (Sigma-Aldrich, St. Louis, MO, USA) were prepared in a physiological salt buffer (15 mM Tris, 126 mM NaCl, 2.5 mM KCl, 25 mM $NaHCO_3$, 2.4 mM $CaCl_2$, 1.2 mM NaH_2PO_4, 1.2 mM $MgCl_2$, 2.0 mM Na_2SO_4) with a pH of 7.4. L-Glutamic acid was dissolved in the buffer solution to a concentration of 1 µM before electrode cycling. All electrode testing

experiments were performed in 1X phosphate buffered saline (PBS) that was diluted from a 10×

purchased buffer (Sigma-Aldrich, St. Louis, MO, USA).

2.3 Computational Methods

Modelling Flow Injection in Flow Cell

The fluid domain was generated in Autodesk Inventor software and imported into ANSYS Workbench

software. An unstructured tetrahedral mesh was generated using ANSYS Workbench meshing tool.

Five prism layers with a growth rate of 1.2 were added at the outer walls, needle and electrode, with

first layer heights of 10μm, 4μm and 2μm respectively. The resulting mesh had ~2.9M elements. Mesh

sensitivity analysis was carried out with meshes of ~0.7M and 5.3M elements.

ANSYS CFX was used to simulate the fluid flow using the Navier-Stokes equations and the transport of

a solute using the advection-diffusion equation with kinematic diffusivity of 600 μm^2/s, representing

serotonin[85]. The walls of the tubing, needle and electrode were modelled with the no-slip condition

and zero solute flux (no reactions at the electrode were included in the model). A uniform velocity

was applied at the inlet with zero pressure at the outlet. The initial serotonin concentration

throughout the domain was set to 0.0001, increasing to 1 at 0.1 seconds and returning to 0.0001 after

11.5 seconds (corresponding to 0.5 ml at 2.6 mL/min). A total of 20 seconds was simulated. The

simulation used the ANSYS CFX high-resolution differencing scheme for advection, which maximises a

blend-factor between upwind and second order differencing schemes, while keeping the solution

bounded. The transient scheme was Second Order Backward Euler, with adaptive time stepping (RMS

Courant number 0.1 with initial, minimum and maximum timestep of 0.02s, 0.0001s and 0.1 s

respectively).

2.4 Electrode Fabrication Methods

CFME

Each CFME was fabricated by hand. For each electrode, a single carbon fiber (diameter = 7 μm;

Goodfellow Corporation, PA, USA) was aspirated into a glass capillary (1.0 mm external diameter, 0.5

mm internal diameter, A-M Systems, Inc., Sequim, WA, USA). The glass capillary was then inserted into a vertical micropipette puller (Narishige, Tokyo, Japan) where the capillary was melted into two micropipettes, each with a carbon-glass seal. The electrode was back connected with a stainless-steel wire coated in silver paint. The stainless-steel wire was then secured with heat shrink. Finally, the exposed length of the carbon fiber was trimmed by hand to 150 µm under an optical microscope.

Carbon paste electrodes

Carbon paste electrodes (CPE) were prepared by mixing 1g of graphite (Sigma-Aldrich, St. Louis, MO, USA) with 20ml polyethylene into a homogenous paste. This paste was backfilled into a pulled micropipette and back connected with a stainless-steel wire and sealed with heat shrink. The filled micropipette was smoothed with sandpaper before being allowed to dry overnight.

Laser-induced carbonization

Either Polyimide tape (Kapton^{TM}) with a thickness of 30 µm (not including adhesives) or polyimide resin was used as a substrate for creating laser induced carbon for electrodes. When using the tape, the substrate was rinsed with isopropyl alcohol before being placed on clean glass slides. Polyimide resin was spin-coated at 3000 rpm for 60 seconds and then cured at 130˚C for 10 minutes prior to being introduced to the laser. A Universal VLS 2.30 CO_2 laser cutter/engraver system with 10.6 µm wavelength was used to laser write defined patterns onto the substrate. All laser shapes were created using CorelDraw software.

LINC electrode fabrication

Polyimide tape substrates were prepared as stated above and lasered using the "Kapton" setting in the laser software into 2mm wide x 5mm long rectangles. Polydimethylsiloxane (PDMS) was then prepared in a 10:1 ratio and degassed until evaporation of dissolved gases stopped. The PDMS was poured onto the carbonized substrates, degassed, and then cured at 130˚C for 2 minutes. If a thinner layer was desired, the PDMS would be spin coated at 500 rpm for 10 seconds prior to degassing. PDMS was then poured uniformly on a separate clean glass slide, put under vacuum for 5 minutes, and

allowed to cure at 130˚C for 2 minutes. The slide with PDMS was then laser etched using the "silicone rubber" setting in the laser cutter software to create empty tracks. The shapes for the tracks were designed in CorelDraw. These tracks were carefully filled with silver conductive paint using a 20μl pipette. The PDMS layer was carefully removed from the slide with the carbonized Kapton tape to graft the carbon onto the silver tracks. This PDMS layer was placed onto the slide with the tracks with the exposed carbon touching the silver. Another layer of PDMS was poured onto the resulting slide and degassed before curing at 130˚C for 5 minutes. A 1mm biopsy punch was used to expose one end of the encapsulated silver track where a steel wire could be inserted to create a back connection. Electrode surface area was defined by cutting with a scalpel to expose the PDMS sealed carbon.
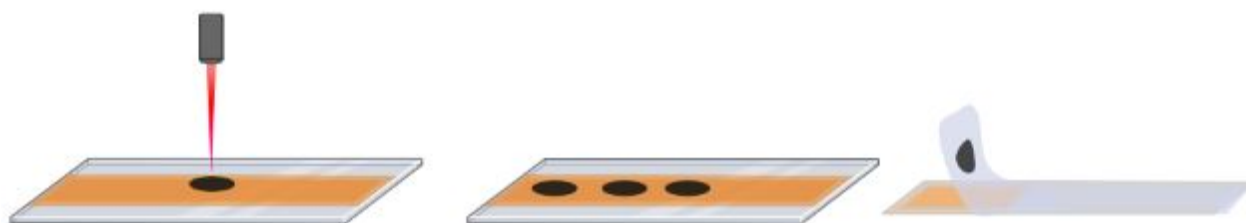

Figure 5

shows the process of laser carbonization of polyimide tape into a circular shape followed by the removal of the applied PDMS layer with encapsulated carbon. A good graft does not leave any visible carbon in the remaining tape.

2.5 3D Printing Methods

The macrofluidic flow cell was designed using Inventor (Autodesk, San Francisco, CA, USA) and 3D printed using both polyjet (Objet Pro with Veroclear resin, Stratsys, Gothenburg, Sweden) and stereolithographic (SLA) (Formlabs Form 3 with clear resin, MA, USA) printers. Microfluidic flow cells, armour, and screw inserts were designed in AutoCAD and printed via stereolithography (Formlabs Form 3 with clear resin, MA, USA). All printed products were washed in a 99% isopropyl alcohol (Sigma-Aldrich, MO, USA) bath and UV-cured for 10 min.

2.6 Casting Methods

Moulds for microfluidic

This multistep casting method is based on previous work in nanoscale engineering[86]. MoldMax25 silicon rubber (Bentley Advanced Materials, Worcestershire England) base and curing were mixed in a 100:5 ratio and then poured over the 3D printed negative. 3D printed negative was created with Blender software and printed with an SLA printer (Formlabs Form 3 with clear resin, MA, USA). The mixture was degassed for 10 minutes until cessation of bubbling and allowed to cure overnight. The resulting positive mould was removed from the 3D printed negative after curing. The components of another resin, Smoothcast-300 series (Bentley Advanced Materials, Worcestershire England), were then individually degassed for a minimum of 10 minutes before mixing. The mixed solution was degassed for 3 minutes only to avoid solidification before pouring onto the positive mould and allowed to cure for 2 hours at room temperature. After removing the cured negative, PDMS (Sylgard 184 Silicone Elastomer, Dow Corning Cop.) was mixed with a 10:1 base to curing agent ratio and then degassed for 10 minutes. Finally, The PDMS mixture was poured on the negative mould and cured for 2 hours at 80 Celsius or allowed to cure at room temperature overnight to minimize any bubbles.

Acrylic

Acrylic mould was created by micromachining an acrylic sheet to dimensions of 25mm length x 25mm width with the laser. Another acrylic sheet with exactly 2mm height was then laser etched into a 25mm x 25mm square with 2mm thick borders. Finally, a third acrylic sheet with a thickness of 0.5 mm was laser cut into a 14mm length x 2mm wide rectangle. The three pieces were assembled with acrylic glue to create a negative mould compatible with PDMS.

2.7 Miscellaneous Methods

Hardware for Macrofluidic flow cell

After printing, a nylon 1/4-28 UNF nut was inserted and bound to the inlet of the flow cell using an epoxy. The epoxy was allowed to cure overnight and an HPLC fitting was fastened into the nut to

create a watertight seal. The flow cell was assembled using stainless-steel standoffs, M3 dome nuts, M3 thumb screws, M3 hexagon nuts, and M3 countersunk screws. The inlet for the thumb screw on the head stage mount was hand-tapped to create 3 mm threads. The part quantity and supplier can be seen in Table 1 below.

part	quantity (per flow cell)	supplier
Stainless steel standoff, Male-Female, 40 mm, 46 mm	6	Farnell, Leeds, UK
M3 dome nuts	3	Accu Ltd., UK
M3 x 8mm thumb screws	3	Accu Ltd., UK
M3 x 6mm countersunk screw	3	Accu Ltd., UK
¼-28 hex nut	1	Zoro, Buffalo Grove, IL, USA

Table 1

lists the hardware needed for the assembly of the flow cell described in **Chapter 3**

Chapter 3 – The Development of a Macrofluidic Flow Cell for FSCV

This chapter describes work that was published as below and my flow cell design will be featured on the cover front of the journal in a future issue:

Hexter, M., J. van Batenburg-Sherwood, and P. Hashemi, Novel Experimental and Analysis Strategies for Fast Voltammetry: 2. A Troubleshoot-Free Flow Cell for FSCV Calibrations. ACS

3.1 Introduction

Fast scan cyclic voltammetry (FSCV) is an electrochemical method traditionally used to monitor neurotransmitters such as dopamine [29], serotonin[53], and histamine[87] because of its excellent spatial and temporal resolution. Researchers that use this technique consistently strive to improve its sensitivity[88], stability[89], selectivity[30], and analytical scope [90-92] to discover clinically relevant physiological mechanisms. These advancements are contingent upon characterization of the performance and behaviour of the electrode to inform measurements. Experimentation with FSCV parameters requires a reliable system that permits experimental controls. When maintaining all flow injection parameters (tubing sizes, flow rates, valving, solutions), the primary sources of variability are the electrode and the flow cell itself. By minimizing the variability caused by the flow cell, the electrochemistry at the electrode surface can be appropriately studied. In this chapter, we present an inexpensive, 3D-printed flow cell design that provides near-ideal injection profiles to probe serotonin FSCV at the electrode. This FSCV flow cell can easily be incorporated into new or existing FIA systems. Additionally, we use fast voltammetry to characterize the electrode response to serotonin under different pre-treatment and matrix conditions to reproduce previous work and elucidate changes to the electrode that may be observed *in vivo*.

FSCV quantifies the current in response to a change in the concentration of a given analyte *via* background subtraction from a specified cyclic voltammogram. A stable baseline current is therefore necessary for comparison with a stable maximum signal indicating the sample plug. The presence of

the analyte around the electrode dynamically changes in real systems, so a system such as FIA is ideal for FSCV calibrations because it introduces dynamic pulses of analytes to the electrode. The FIA system requires a flow cell to reliably produce a square-like injection signifying that the electrode has reached steady state [93]. Following an injection, the signal should quickly return to baseline to indicate that the analyte has passed the electrode. Deviations from an idealized square plug at a given concentration yields inaccuracies when relating current to concentration.

3.2 Results and Discussion

Fluids Theory

Once a functional flow cell had been designed, the nature of the flow and mass transport in the cycling well was determined with the Reynolds number and the Peclet number respectively. These parameters were considered to reveal which properties of the system most significantly affected the injection profile. The Reynolds number is calculated first to determine if the flow is laminar or turbulent because turbulence promotes analyte mixing that may impact the transport mode predicted by the Peclet number.

The Reynolds number (Re), defined by Equation 1, is a measure of the balance between the forces that keep a fluid moving smoothly (inertial forces) and those that resist its movement (viscous forces). The Reynolds number is calculated by dividing the product of the flow rate (Q), the density of the fluid (ρ), and the diameter of the well (d) by the viscosity of the fluid (μ). In this estimation, the viscosity of water is used (1mPa·s) due to the low concentration of solutes. The Reynolds number for the fluid entering the cycling well is approximately 0.0025, indicating that the flow is laminar.

$$Re = \frac{4\rho Q}{\pi \mu d} \qquad\qquad (1)$$

The Peclet number (Pe) was calculated with Equation 2 to evaluate the ratio of advective to diffusive transport of the analyte to the electrode. The Peclet number was determined by utilizing the diffusion coefficient of serotonin (D_{ser}=5.4 x 10^{-6} cm^2s^{-1})[85], and the fluid velocity (v). The fluid velocity was

obtained by dividing the flow rate of 1.7 mL/min by the cross-sectional area of the tubing. According to our estimation, the delivery of the analyte to the electrode is influenced by advection, with a Peclet number of 1400.

$$Pe = \frac{dv}{D_{ser}} \qquad\qquad (2)$$

Flow Injection Profiles

Figure 6A presents an idealized FSCV flow injection resembling an experimental injection. It is expected that diffusion and electrochemical kinetics will smooth the edges of the signal in experimental injections. If diffusion and electrochemistry are ignored, the sample plug will appear as shown in Figure 6C. Figure 6B illustrates a problematic injection profile collected with an earlier flow cell design that suffers fluctuations, artifacts, slow rise time, leaks, and dead space. The cube shaped flow cell resulted in droplet formation due to the pressure differentials caused by its edges. Addressing these issues requires consistent troubleshooting before each experiment. To achieve the desired flow cell response, we established strict design criteria to reduce flow inconsistencies, leaks, and dead volume. Dead volume is particularly problematic because it causes dispersion of the sample plug thereby reducing the steady-state concentration and increasing the time that the electrode is exposed to the analyte. Figure 6E highlights the distortion of the injection profile due to dispersion, which can extend the signal duration beyond the acquisition window of FSCV making calibration impossible.
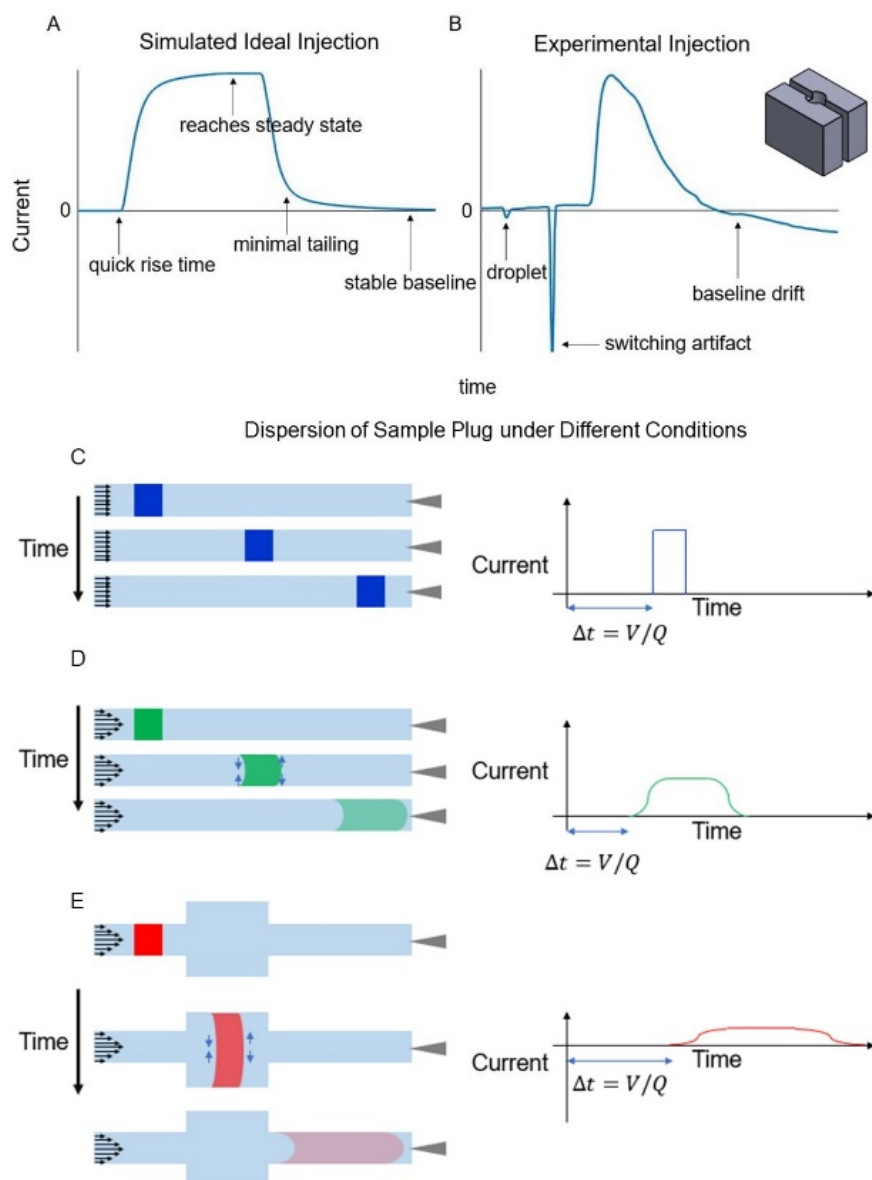
Figure 6

show (A) a computationally modelled ideal injection profile and (B) an injection profile characterized by droplet formation due to the edges of the depicted cubic flow cell. Figures 6C-E illustrate the changes in a sample plug over time due to variations in fluid characteristics and system parameters, emphasizing the role of dispersion in FIA systems. The blue sample plug in Figure 6C shows the evolution of a fluid with no viscosity and uniform velocity, which results in no dispersion. In Figure 6D, the green sample plug depicts a fluid with a non-zero viscosity and a no-slip condition that results in a parabolic flow profile. This flow profile causes solutes in the center to move faster than those at the edges, resulting in radial concentration gradients that promote Taylor dispersion. In Figure 6E, the red sample plug is a fluid under the same conditions as the green sample plug, but with additional dead space that increases the time required to reach the electrode. The increase in dead space warps the bolus due to added dispersion.

Flow Cell Design

Figure 7B illustrates the flow cell design. The electrode mount (2) centers the electrode accurately in the cycling well to ensure reproducible exposure to the peak concentration of analyte in the sample plug. This eliminates the need for an expensive micromanipulator and prevents dispersion of the electrode in the flow stream, which has been previously studied [68]. The head stage mount (3) fastens the head stage to the flow cell and prevents damage to the data acquisition wires and the electrode. After introduction to the electrode, the sample plug leaves the cycling well and flows down the dome-shaped flow cell to a waste reservoir (4). To minimize snaking and guarantee a stable flow, the dome of the flow cell contains a shallow channel that is visible in the aerial view of the flow cell shown in Figure 7B. Additional features include a tunnel for the reference electrode (5), a cycling well with a tapered inlet (6), and area for the hex nut to secure the inlet fitting (7).
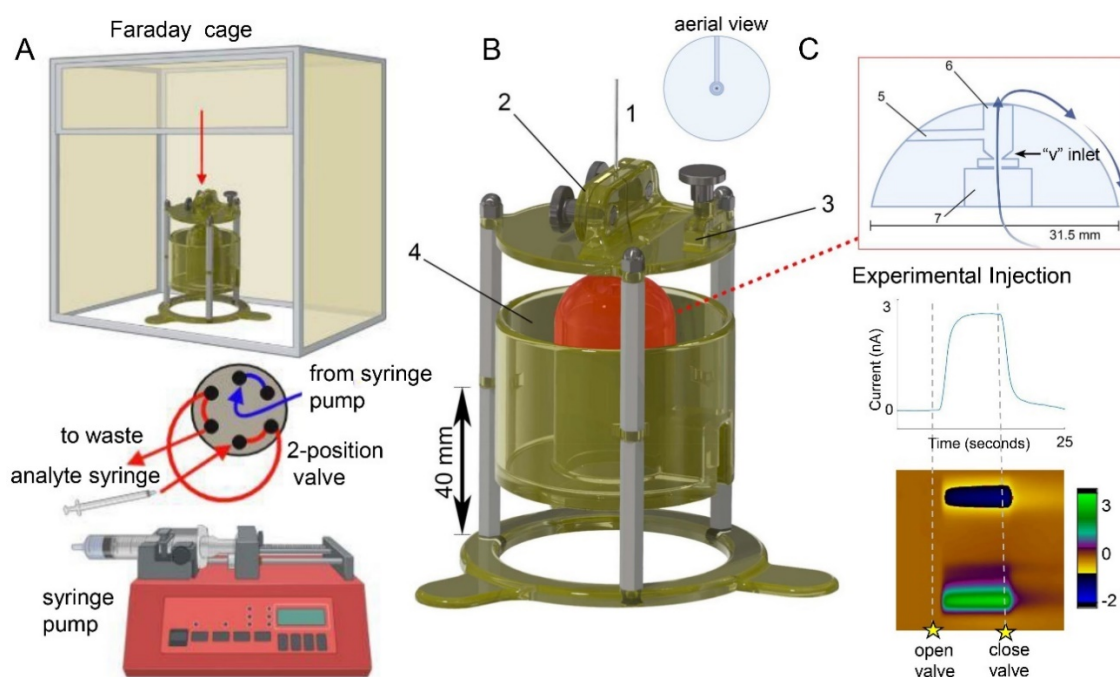
Figure 7

Shows the latest macro flow cell design in our flow injection system with a syringe pump, a valve, a sample syringe, and a faraday cage containing the flow cell (not shown to scale). The electrode is placed in the flow cell at the position indicated by the overhead red arrow in Figure 7A. The syringe pump delivers the buffer while the sample syringe introduces a known volume of the sample into the flow cell through the 2-way valve that results in a pulse of analyte detected by the electrode (Object 1 in Figure 7B).

Experimental Injections

With the most recent flow cell iteration, we achieved square injections exemplified in Figure 7C. The signal reaches steady state, rises, and falls without excessive tailing well before the end of the data acquisition window. Note that this flow cell is optimized for the geometry of a micropipette shaped carbon fiber microelectrode. Attempting injections with electrodes of other geometries, like a planar carbon paste electrode without a tapered end will result in a poor injection from the fluidics alone, which can be seen in Figure 8. The square shaped electrode does not reach steady state and has excessive tailing and is therefore not viable for calibration.

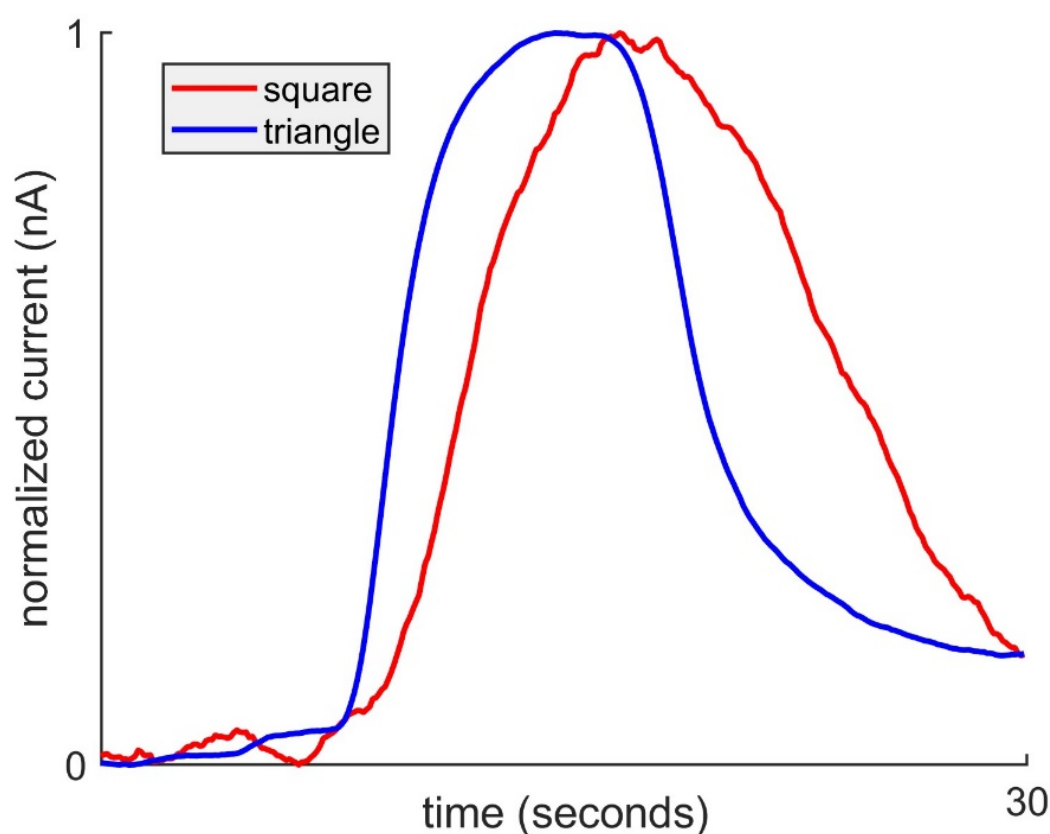*Figure 8*

shows a 1 µM injection of serotonin using the same electrode (LINC) that was cut with a scalpel from a square tip to a tapered triangular-like tip. The y-axis is current normalized to 1 because of drastic sensitivity differences in the injections caused by differences in the exposed electroactive area.

Design Features

After using the Re and Pe numbers to determine the flow is laminar and that advective transport dominates the system, it is determined that phenomena such as pressure gradients significantly impact the performance of the flow injection analysis system. Furthermore, the fluids in this system have a non-zero viscosity so dispersion of the sample plug is expected. Intuitively, pulsing and flow inconsistencies such as (A), leaks (B) in addition to dead volume (C) overwhelmingly influence the flow injection profile by distortion and pressure changes in the flow stream.

A.   Design features to reduce pulses and flow inconsistencies

The flow cell outlet was designed into a dome shape to mitigate pulses in the flow stream because curved surfaces minimize pressure drops in the flow stream, thereby improving injection reproducibility. The dome's curved shape enables minimal variation in the fluid velocity to maintain a smooth, uninterrupted flow. Moreover, designing a reservoir helps to reduce flow pulses caused by droplet formation that occur when using conventional tubing used as an outlet. Waste fluid is removed from this 60mL reservoir to prevent overflow. An earlier iteration had a reservoir of 30mL to allow easy access to the underside of the inlet but required frequent fluid removal. This reservoir-based design is an open fluidic system, which has the benefit of enabling near-instantaneous equilibration with atmospheric pressure in contrast to the large pressure drops that occur in closed systems. Pressure anomalies caused by valve switching in FIA can be rapidly dissipated with an open fluidic system. A less intuitive feature that improves reproducibility is the stands for the flow cell itself. The stands maintain the flow cell in the same position during experiments. Without the integrated stands, it would be necessary to fasten the flow cell to external stands prior to each experiment. Slight variations in the angle of orientation of the flow cell may change the way the fluid cascades down the side of the dome.

B.   Design features to prevent leaking

The 3D printing methods (polyjet and stereolithography) were chosen for their resolution and fluidic compatibility. Printing with other methods like fused deposition may not have the resolution to preventing leaking. Additionally, the photoresins used in polyjet and SLA printing are highly hydrophobic, which is ideal for aqueous-based fluidics because the solutions will not dissolve or warp the printed part. With both printers, a clear resin was chosen to allow visualization of the channels. This is particularly helpful during the optimization process to identify the source of a leak using coloured fluid. It is essential to ensure all fittings are compatible and do not degrade over time to minimize the possibility for leaks. High pressure male fittings and their female hex nut counterparts were chosen to guarantee a fluidic seal. An indentation was designed to house the hex nut to create a water-tight seal. Earlier flow cell iterations required tapping of the 3D printed part, which was problematic because the photoresin material cannot withstand the force of tapping. Additionally, tapping is manual which introduces an element of variability.

C.   Design features to minimize dead volume

Dead volume allows time for the sample plug to disperse thereby increasing the time to analyte detection and reducing injection quality (Figure 6C). In FSCV, it is critical to minimize the time to analyte detection because of the short acquisition window necessitated by background subtraction. A tapered inlet (labelled v-inlet on Figure 7C) was added to the design to focus the flow stream to minimize dispersion of the sample as it reaches the electrode. This inlet shape permits the use of a slower flow rate while reducing the internal volume of the channel to eliminate more dead space. Furthermore, this decrease in flow rate did not impact the time to detection of the electrode while reducing the amount of buffer solution needed for the duration of experiments. The smallest volume possible was used for the hex nut to minimize the distance between the end of the tubing from the HPLC valve to the electrode. Lastly, the cycling well diameter was reduced to 3mm from 5mm in earlier iterations to decrease the cycling well turnover time.

Robustness and Reproducibility

After the flow cell could produce ideal injections, we first looked at the variation between individual electrodes and then examined the robustness and reproducibility of the design itself. The design reproducibility was challenged by performing calibrations with two prints from the same printer and one from a different printer. These FSCV calibrations with serotonin were performed with concentrations of 10, 25,50, 75 and 100 nM on each electrode. Based on the results, the concentration of serotonin can be estimated with an uncertainty of 0.2nM in this range. Figure 9A shows a calibration curve with 3 injections averaged per concentration point. The spread of data is highlighted by shaded red indicated the bounds for a 95% confidence interval.

Figure 9B displays the residuals of the data for each calibration point from Figure 9A. A linear regression appears to be an appropriate fit for the data because the residuals in Figure 9B are primarily randomly distributed. Previous work with FSCV calibrations indicates the suitability of a linear regression in this concentration range[53]. The only peculiarity in the residuals is that the minimum and maximum concentration point residuals are both positive values. This is probably because of the order in which calibration point data was collected. Because electrode sensitivity decays with consecutive injections [67], the order in which the calibration curve is performed will change the current values collected. Because this data set is small (9 electrodes), the bias in the order of calibration standards introduced to the electrode is more apparent, even with a random number generator. Another important consideration is the solution matrix, which can substantially change the slope of calibration, even if it is only slightly different. Figure 10 shows a comparison of a calibration performed in glutamate versus the three amino acids (glutamate, gamma-aminobutyric acid, and glycine) all in physiological buffer. Even with large error from matrix effects, depicted in Table 2, calibration is an important tool to estimate the concentration of relevant analytes for biomarker development and the elucidation of physiochemical kinetics. Intuitively, prediction error will always be lower when comparing collected data from the same matrix. The magnitude of the error in the difference between the value predicted by a calibration curve and an experimental value was calculated via RMSE and

shown in Table 2. The magnitude of this error could not be due to using different electrodes or decay in sensitivity alone based on the estimated error based on Figure 10.

Figure 9

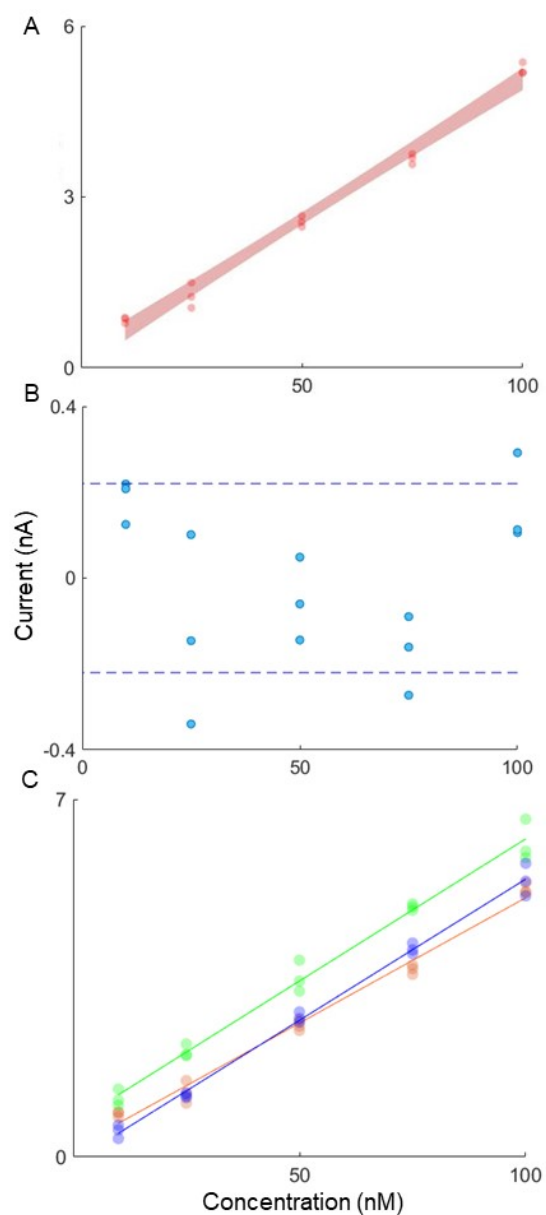Serotonin calibration curves (A) representative calibration curve with shaded 95% confidence bands (B) Residuals of the calibration with uncertainty as the standard deviation of the residuals indicated by dashed line. (C) Calibration curves for serotonin measurement with (n = 3) different Nafion electrodeposited electrodes in one flow cell. Electrodes were pre-treated with glutamate as stated in the methods section.
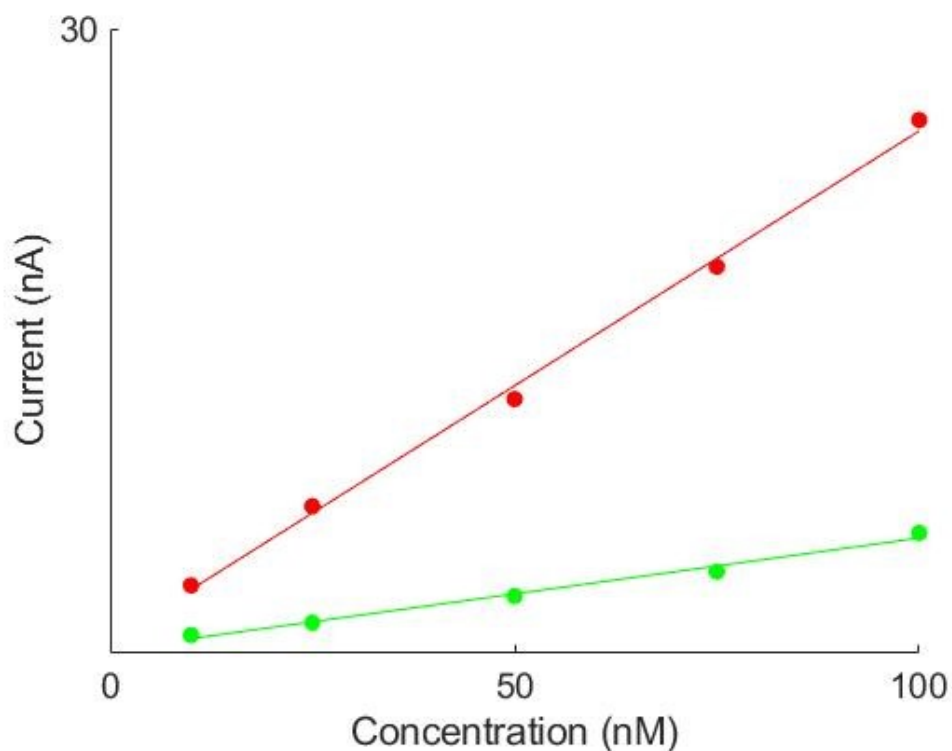
Figure 10

Calibration curve performed in glutamate only (red) versus glutamate, gamma-aminobutyric acid (GABA), and glycine (green) all in physiological salts buffer.

matrix	RMSE (nA)
same	0.288
different	226

Table 2

Root mean square error (RMSE) between the estimated and true values for concentrations in differing matrices.

To examine the variation between different electrodes in the flow cell, FSCV calibrations were done with 3 separate electrodes as illustrated in Figure 9C. These calibrations are reproducible despite the variation in sensitivity caused by hand-fabrication. The difference between the residuals for each concentration of each electrode was found to be insignificant ($p > 0.05$) when treated with a 2-way ANOVA. Furthermore, the uncertainty of the estimate (0.2nM) is the same for the representative

calibration in Figure 9A as the mean for all calibrations performed, which is additional evidence of the

reproducibility of these calibrations. This would not be possible without reliable individual injections

for each calibration point.

A

B

C
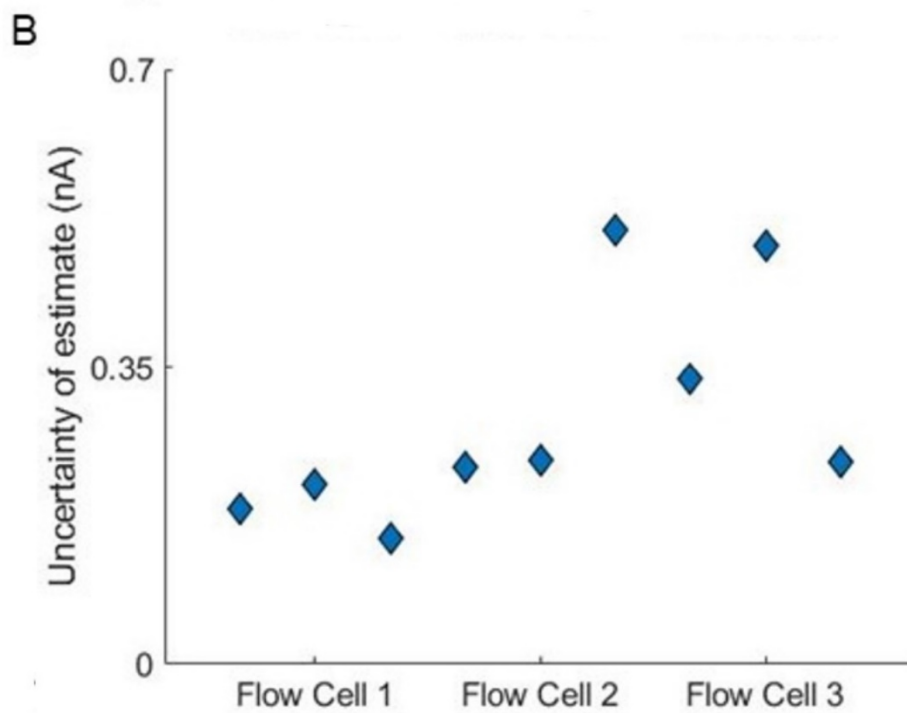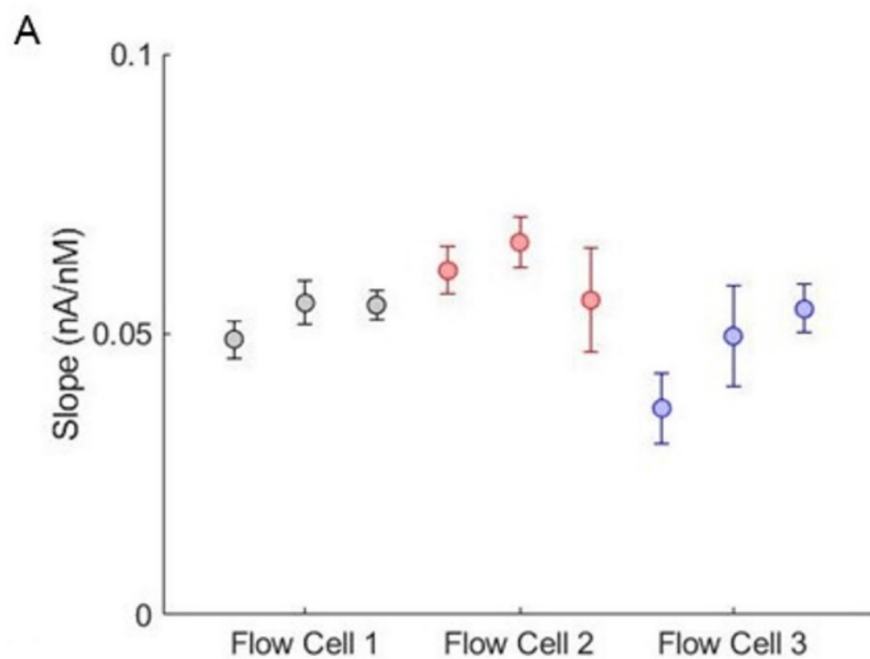
Figure 11

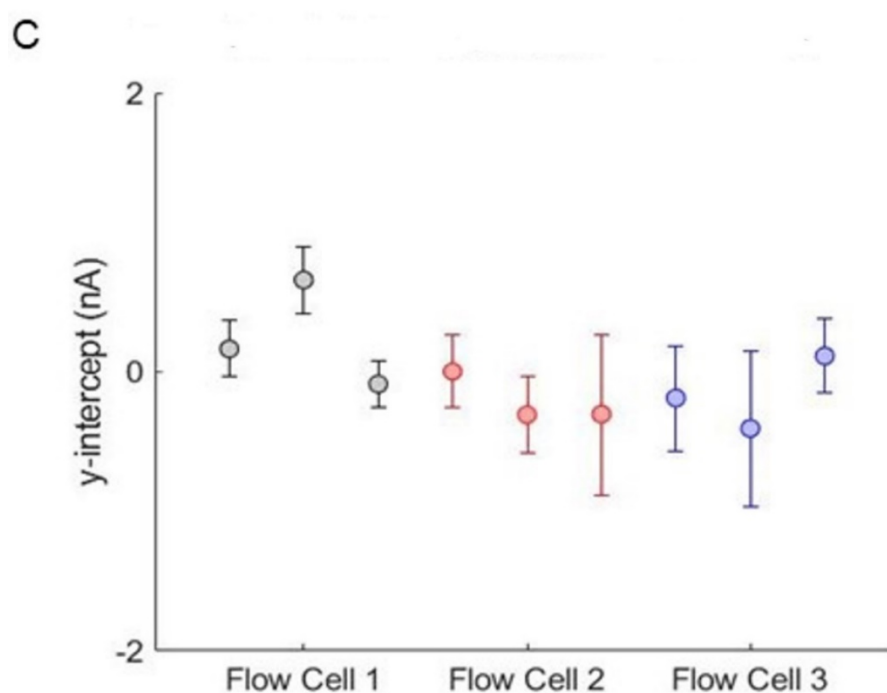95% confidence interval for given regression parameters and uncertainty of estimate for each calibration in each flow cell print. (A) slope for each linear regression with 95% confidence interval bounds. (B) Standard deviation of the regression for each calibration curve(C) y-intercept for each linear regression

After establishing insignificant variation between electrodes on the same print, we probed reproducibility between prints on the same printer and prints from a different one. Calibrations were performed with 3 electrodes per print. The print from a different printer was not only a different printer and printing method, but also a different material. It is important to note that each of these prints was easily assembled and did not require trouble shooting prior to calibration. The most difficult part of assembly is gluing the hex nut into the print, but this is only done once and then functional for the life of the print.

Figure 11A-C shows the variation in the slope (as defined by 95% confidence bounds), uncertainty of estimate, and y-intercept (also using 95% confidence bounds) across each calibration performed in each print. Using another ANOVA, it was found that there was no significant difference in any of these

parameters (p > 0.05) across prints, proving the robustness of the design across different printers and materials.

Stability

Following the evaluation of the reproducibility and robustness of the flow cell design, we evaluated the stability of the flow cell injections on a scale of hours and days. For each electrode, 1 µM serotonin was injected every 2 minutes for 40 injections (or 80 minutes). The red markers in Figure 13 illustrates the average of these injections. After these injections, the electrodes were stored dry, and the flow cell was cleaned. Electrodes must be stored dry to prevent a massive drop in sensitivity, likely due to the potential for auxiliary reactions to occur on the surface of the electrode in solution. The dry stored electrodes were used again every 24 hours (with 4 injections of fresh solutions) for the following 4 days. Figure 13 shows a significant decay in signal over the first 25 injections that becomes stable after 40 ± 2 injections based on an exponential fitting of the decay ($y = 78.25e^{-0.0201x}$) performed in Matlab. Interestingly, fitting a decay to a given electrode appears to predict the loss in current with successive injections. The decay in sensitivity can also be reversed by reoxidizing the electrode using the extended Jackson waveform, which can be seen in Figure 12. Figure 12 shows a 38% increase in sensitivity between an injection from an electrode that has reached stability after 40 and an injection with the same electrode following recycling with the extended Jackson waveform.

The loss in sensitivity observed is likely not an issue of reproducibility of the flow cell based on data analysis. We would expect to see changes in the way injections vary over time if the flow cell was the cause of the instability of sensitivity. In addition to a constant rate of decay fitting the data, the coefficients of variation of the first 10 injections are not statistically different (p >> 0.05 by f-test) from that of the last 10 or the injections over 96 hours. This suggests that the decay is likely due to a controlled phenomenon, such as an electrochemical reaction like electropolymerization, which has been previously observed [67]. In this previous work, serotonin and its metabolites have been shown

to polymerize on the electrode surface, which is less prevalent in vivo because of a complex interaction

of other ambient amino acids polymerizing on the electrode.

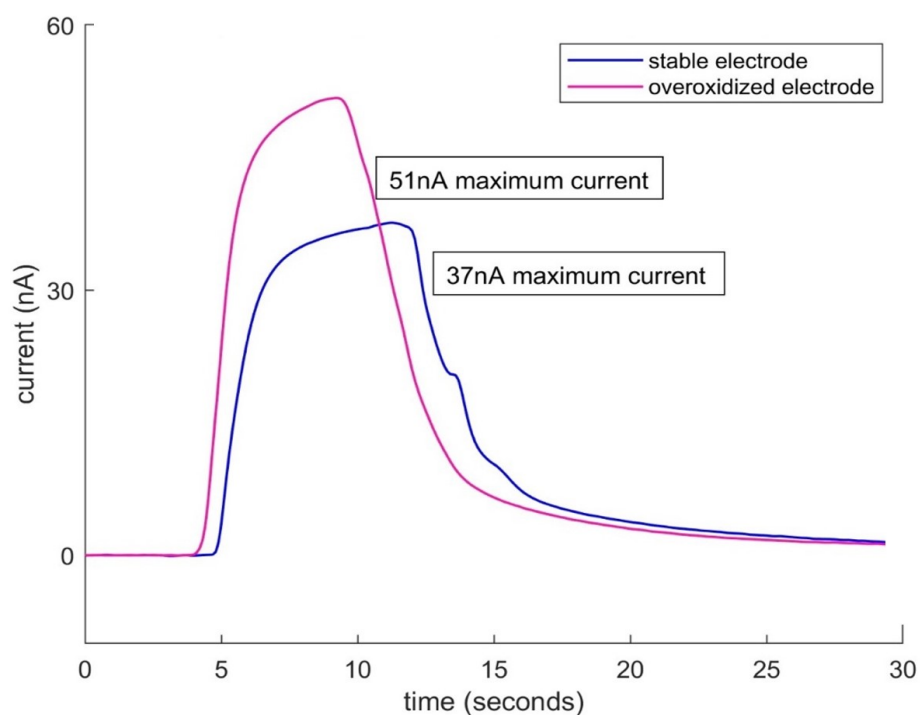*Figure 12*

shows 2 injections of 1 µM with the same electrode. The blue line depicts an injection after 40 previous injections of 1µM

serotonin. After this injection, the same electrode was cycled using the extended Jackson waveform as listed in the methods

section. The pink line indicates an injection with the same electrode after cycling.
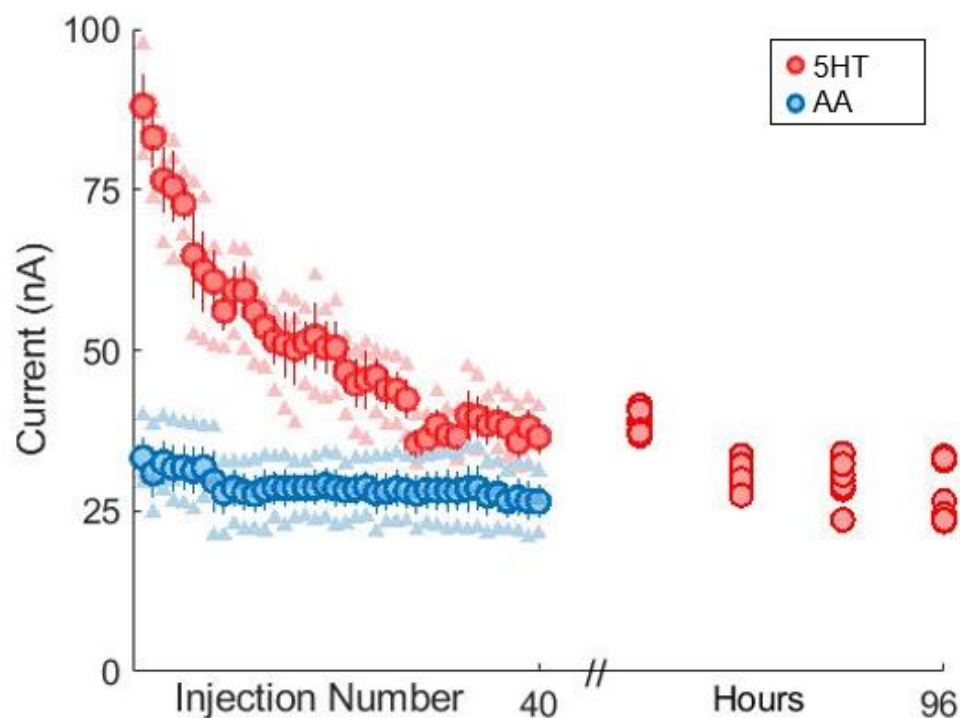
Figure 13

Three trials each of 40 successive injections of 1 µM serotonin (red) and 100µM ascorbic acid (blue) with corresponding current values. After each set of 40 injections, a single injection of 1 µM serotonin was introduced to the electrode every 24 hours for 96 hours.

To begin probing if the decay was an electrochemical phenomenon, we sought to determine if this drop in sensitivity was analyte specific by repeating the injection protocol with ascorbic acid (AA). Ascorbic acid doesn't have the same capability to electropolymerize on the electrode surface as serotonin because it lacks the terminal amine group required for the reaction. Figure 13 depicts the stark contrast in decay between serotonin and AA. AA stabilizes within the first few injections confirming that signal decay in serotonin analysis is due to the electrochemistry of serotonin with the electrode and not due to instability of the flow cell. Next day injections with AA were not performed because of the stability of the injections. Finally, the rate of decay is not only analyte specific, but also varies with the chemical composition of the buffer solution. It was observed that consecutive injections in PBS resulted in a slower decay, but started from a much lower initial current value[67].

FSCAV in the Flow Cell

A flow cell is not necessary to perform FSCAV because the technique can determine tonic concentrations unlike FSCV. Nonetheless, we sought to test the compatibility of the flow cell with FSCAV to streamline consecutive experiments with the two techniques. Like FSCV, the peak current and integrated charge extracted from the cyclic voltammograms (CVs) decay with successive data acquisition files. Unexpectedly, it was found that when the flow cell was static (to mimic a beaker), no serotonin oxidative peak at 0.65V was observed, which is depicted by the purple expanded CV in Figure 14. Interestingly, the peak was partially rescued when introducing a flow of 1mL/min of the sample in the system. It is possible that the material of the flow cell, which is proprietary information, impacts the holding window in FSCAV where the analyte is allowed to adsorb to the surface of the electrode prior to reapplication of the waveform. The advective force introduced by the flow could potentially mitigate the interaction of the analyte and the electrode with the flow cell material. It is important to note that the FSCAV in this work was performed at a holding potential of 0V instead of the 0.2V stated in the literature due to a bug in the WCCV software that prevented the waveforms from being properly switched.
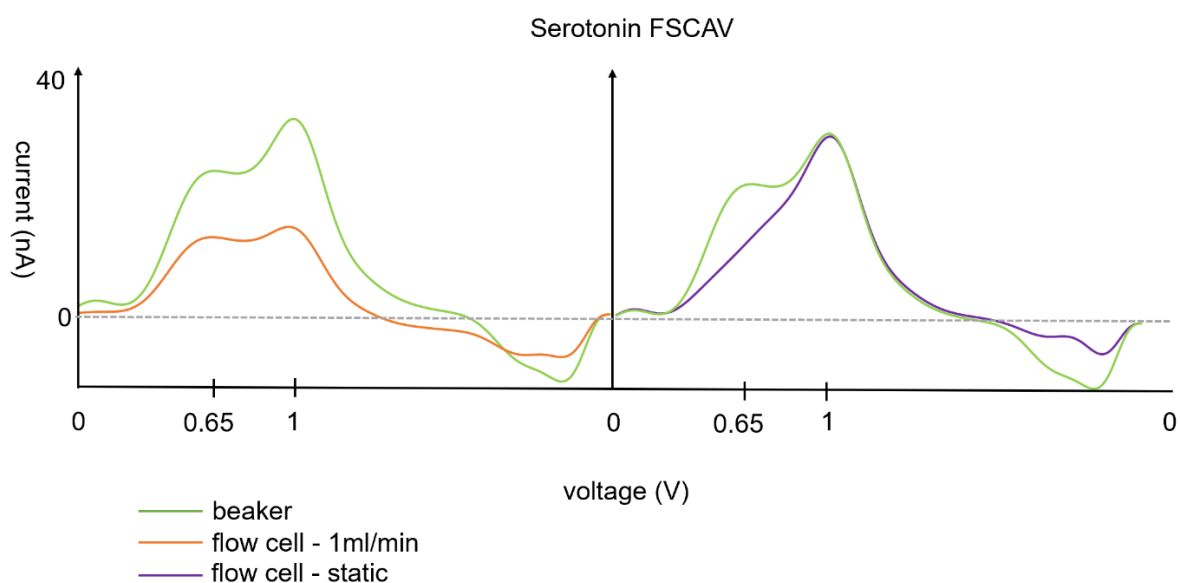
Figure 14

Expanded CVs of 1 micromolar serotonin FSCAV in either a beaker, the flow cell with a flow of 1ml/min, or static flow cell. The graphs are plotted against data acquisition point number (which is directly linked to a given voltage) to expand the CVs to better visualize the oxidative peak. The voltage ticks on the x-axis provide a reference point to the applied waveform.

3.3 Conclusions

Calibrating electrodes for FSCV measurements of neurotransmitters has been difficult because of a lack of standardization of the calibration process. This challenge also slows the process of inventing new electrodes and electrode modifications by making the testing process tedious. The flow cell itself is historically the most variable part of the flow injection system. There have been numerous problems encountered with in-house developed flow cells that include pulsing, leaks, inconsistent flow, and a large dead space, all of which result in unreliable flow injection profiles. However, evaluating the fluid dynamics of the system allowed us to create this flow cell design that all but eliminates these common problems. Several important features such as the v-inlet, dome-shaped outlet, electrode mount, and waste reservoir specifically address these common issues. This design enabled stable, low-error, and reproducible flow injection profiles, despite variations caused by the hand-fabrication of electrodes and complex electrochemical processes. Furthermore, the design is plug and play and inexpensive to print to encourage use across labs that use FSCV.

Chapter 4 – The Development of a Versatile Laser Induced Carbon Electrode Compatible with Microfabrication

4.1 Introduction

Dynamic processes that occur in the brain are difficult to examine due to the time frame in which they occur and the complexity of the surrounding chemical environment. FSCV has been employed to monitor these processes *in vivo*, however the technique is invasive, which necessitates the introduction of *ex vivo* models. Advancements in organoid technology have showed promise in recapitulating the chemical functionality of the brain, but present new analytical challenges. These obstacles include the fragility of CFMEs, which are the gold standard for *in vivo* FSCV. CFMEs exhibit superior electrochemical properties and physical suitability for this application. However, for *in vitro* applications, other graphite-based materials, such as carbon composite and pyrolytic carbon films, have been explored to address the physical limitations of CFMEs[94]. CFMEs are difficult to integrate with *in vitro* systems and are time consuming to make. In this work, we explore ways in which electrode materials can be integrated into *ex vivo* devices. Specifically, we consider carbon paste electrodes (CPE) and laser induced nanocarbon (LINC) electrodes for FSCV sensing. Finally, we introduce an inexpensive fabrication protocol for functional and versatile LINC electrodes with the potential for integration and commercialization.

4.2 Specific Methods

This section contains interim results that guided the methods.

Basic considerations when developing a fabrication protocol for electrodes with our FSCV system are the insulation, back connection, track material/geometry, and acceptable range for electroactive area. More specifically, the insulation must be structurally sound enough to encapsulate all conductive parts of the electrode, besides the desired electroactive area, for the duration of use to prevent shorts in the circuit and to minimize external noise. Additionally, the insulator must have sufficient adhesion to the electrode (termed "good seal" for CFMEs) or air pockets may form leading to excess noise. Next,

the back connection must reliably allow the electrode to make contact with the data acquisition system. The electroactive area must be large enough to generate a working signal, but small enough to prevent overloading of the data acquisition system and minimize ohmic drop. Critically, the electrode must not delaminate during its experimental lifetime.

Choice of Electrode Materials

CPE

Initially, we sought to determine the feasibility of CPEs enhanced with carbon nanotubes (CNTs) to address the poor signal to noise ratio normally encountered with the CPE[95]. While adding carbon nanotubes drastically improved the sensitivity of the electrode, it resulted in an overload of the data acquisition system. Because of difficulties in controlling the addition of CNTs, we sought other unsuccessful fabrication-based strategies to address the poor signal to noise ratio. After developing a production protocol previously stated in the general methods, we examined the properties of a polyethylene-graphite CPE. Like previous studies[49] with other types of carbon paste electrodes we observed lower electrical conductivity, due to the concentration of insulating binding agent, and slower electron transfer kinetics, leading to reduced sensitivity and response time for FSCV measurements. Furthermore, these CPE generated more noise, particularly in comparison with CFMEs, which creates a challenge for FSCV measurements.

LINC

Laser-induced nanocarbon (LINC), is another type of pyrolytic carbon, that has been used as an electrode material for voltammetry. Previously, pyrolytic carbon thin films have been created via heat treatment of substrates, such as SU-8, to temperatures >900 C in an inert atmosphere[96]. In contrast, LINC electrode fabrication only requires a laser to ablate a carbon target material, such as graphite or carbon fiber, in a controlled environment to produce a thin film of carbon on a substrate. The resulting carbon film has a unique microstructure, including high surface area and the presence of defects that make it well-suited for electrochemical reactions. Moreover, laser ablation of a carbon rich substrate

is quick and inexpensive. Laser-induced carbon electrodes have been shown to exhibit excellent electrochemical performance, including high sensitivity and selectivity [60], for the detection of neurotransmitters and other small molecules[61, 97]. Additionally, the laser-induced carbon can be functionalized with nanoparticles to enhance its electrochemical properties further[62]. The porosity of the generated carbon is the primary concern when building electrodes from this material because it makes the material mechanically unstable and causes uncontrolled background current [49], which was observed in the early trials performed in Table 3. Furthermore, when depositing substrate directly on top of a track, the porosity of the induced carbon led to exposure of the underside track resulting in a circuit short due to the lower resistivity of the metal track materials. Porosity can be addressed by physically pressing the material together, commonly by lamination, or by filling the holes with a stabilizing material. Despite these concerns, laser-induced carbon electrodes have the potential to become a formidable electrode material for FSCV of neurotransmitters.

Previous Electrode Configurations

A table illustrating the different electrode configurations that were trialled is provided as reference material for review in the subsequent sections of this chapter.

Trial	Pyrolysis substrate	Carrier	Track type	Wire connection	Insulator	Number of pyrolyzed substrate layers	Spin coat	Result
1	PI resin	PMMA 3D printed	carbon	Silver paint	silicone	1	no	Overloaded signal

2	kapton	glass	Metal sputtered	Silver paint + kapton tape	kapton	1	N/A	Minimal contact between carbon and metal/laser destroys tracks
3	PI resin	glass	carbon	copper	silicone	1	yes	Unstable back connection
4	kapton	resin	carbon	N/A	silicone	1	no	Unstable back connection/unable to control surface area
5	PI resin	resin	Silver paint	N/A	N/A	1	no	Not viable-laser doesn't reach silver paint
6	PI resin	resin	Silver paint	N/A	N/A	1	yes	Not viable cannot spin coat onto resin
7	PI resin	glass	Carbon and silver paint	Solder to	Silicone conformal	1	no	Laser depth issue
8	PI resin	glass	carbon	PI resin bonded	PI	1	yes	PI is a bad insulator w/out spin coat (exposed connection)

| 9 | PI resin | glass | carbon | Solder to | Silicone conformal | 1 | yes | Weak signal for 10 minutes that then disappears |
| 10 | PI resin | glass | carbon | Solder to | PI and Silicone conformal | 2 | yes | Unstable signal or overloaded signal |

Table 3

Early development stage trials of different configurations of electrode builds using either cured polyimide resin or Kapton tape as laser substrate, all with negative outcomes. Carrier refers to the surface on which the substrate was places. Track type indicates the connection material between the electroactive area and the wire to the data acquisition system. Wire connection signifies the way in which the wire to the data acquisition system was secured to the track.

Methods to Evaluate Electrode Candidates

Oscilloscope Signal

Electrode configurations can be initially evaluated based on their oscilloscope signals. The oscilloscope displays the resulting potential of the electrochemical cell during waveform application. The quality of the reference electrode and buffer solution may also distort the oscilloscope signal, but it is primarily influenced by the working electrode and the characteristics of the applied waveform. It can be observed that the oscilloscope signal of an electrode predicts its electrochemical performance to an extent when all other variables are controlled. This technique is particularly useful when deciding whether an electrode is viable prior to experimentation. The main 4 categories of oscilloscope signals with a resolution of 1 V/ms are depicted in Figure 15. Only the oscilloscopes of electrodes cycling with the Jackson waveform were used for evaluation because the majority of this work was performed for serotonin analysis. It is also common to acquire signals that depict combinatory transition states between the oscilloscope categories listed in Figure 15.
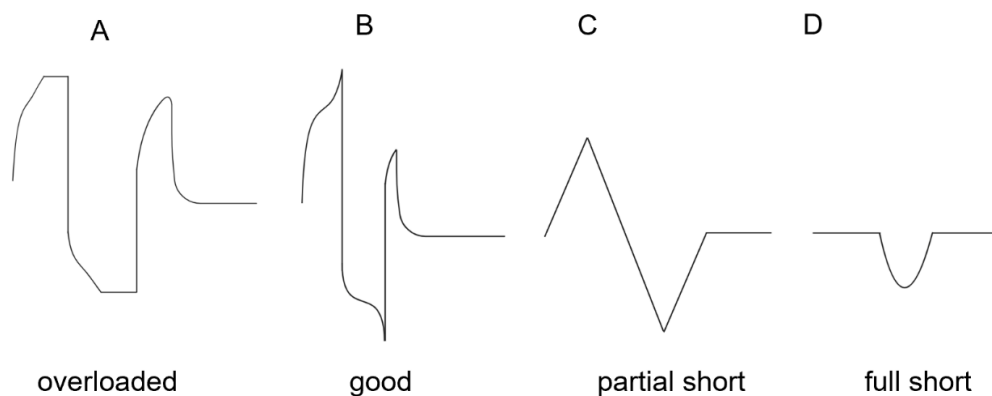
Oscilloscope Signals in WCCV at 1V/ms

| A | B | C | D |
| overloaded | good | partial short | full short |

Figure 15

The 4 main types of oscilloscope signals encountered during the evaluation of electrodes for their suitability for FSCV measurements. A "good" electrode signal indicates that the background current is within the bounds of the data acquisition system and reflects a signal exhibited by a well-performance CFME.

With CFMEs, non-viable electrodes typically exhibit a signal between Figure 15B and 15C indicating a broken seal or micropipette where some of the metal back connection is exposed to the solution. Figure 15C has also been observed when CFMEs are not fully submerged into the buffer solution in the flow cell. Figure 15D indicates that none of the background current is flowing through the desired electroactive area and is instead conducted through the metal back connection due to its lower resistivity. Electrodes with an overloaded signal, as illustrated in Figure 15A, indicate that there is an overexposure of the electroactive area of the carbon resulting in a background current that is too large for the data acquisition system. When a CFME presents an overloaded signal, it is usually because the carbon fiber has not been trimmed adequately. The oscilloscope signal may also reveal that the electroactive area is too small or not conductive enough via the amplitude of the signal. Low electroactive areas will require the magnification of the oscilloscope to be increased from 1V/s to the mV/s scale to visualize the signal and are not viable for measurement. Finally, an oscilloscope signal may evolve over time to reflect changes to the electrochemical cell that occur during cycling and experimentation. For example, the unstable oscilloscope signal resulting from trial 10 of table 3

occurred because the buffer solution slowly diffused through the layers of the electrode configurations exposing more electroactive area over time.

Project Considerations

Initially, strategies that were compatible with resin-based 3D printed designs were preferred due to their simplicity and inexpensiveness. Furthermore, many of the choices for materials in Table 3 were influenced by affordability and logistical convenience. The limitations of the laser were one of the first project considerations. It was observed that the laser did not have the resolution to reproducibly create shapes with total areas of less than 500 µm. Moreover, it was not capable of penetrating substrates beyond a few microns in depth, and it was only able to ablate planar substrates. The second major design limitation was the porosity of the pyrolyzed carbon. More specifically, it was difficult to define the electrode area while addressing the porosity, visible in Figure 16A, of the carbonized substrate to prevent unstable signals, which was a key design challenge in this work. The mechanical packing approach (lamination) to eliminate porosity was not possible due to the lack of an available lamination system. This prompted the encapsulation approach where the pores were filled with an insulator and then the electrode was re-exposed to define the electroactive area.

Substrate and Carrier Optimization

Substrates are typically situated on a glass slide because the surface of the slide is uniform and free of defects. However, glass slides are expensive for high volume use and cannot be easily fabricated into custom shapes for integration in a 3D printed microfluidic, so we initially sought to resin print carrier glass slides, which appeared to be a material similar to polymethylmethacrylate (PMMA). The resin material exhibited an increased surface roughness that was not conducive to spin coating. Furthermore, the material was not thermally stable enough for rapid heat curing of the polyimide (PI) resin, even after UV curing of the resin to improve thermal stability. Also, UV curing of the printed slide caused its shape to curve and distort. Trial 1, listed in Table 3, where a 3D printed carrier was filled PI resin for carbonization, coated with silicone insulator, back connected with direct insertion of

a stainless-steel wire, and exposed with a needle resulted in a briefly stable oscilloscope signal that became overloaded with time. After electrochemical cycling in phosphate buffered saline (PBS) solution, a residue appeared under the silicone on top of the uncarbonized PI resin indicating air pockets in this configuration, which were likely the culprit of the decay in the quality of this oscilloscope signal.

Kapton tape was the first material we chose to carbonize based on its use in previous work[98]. However, integrating the residual tape itself into a sensor was challenging due to unreliable contact between the carbonized substrate and underside track, which was also the primary culprit of unstable signals in most of this work. The use of PI resin was proposed to address the limitations of Kapton tape by inducing bonding to adjacent design layers. The PI resin was particularly compatible with the 3D printed resin used for early microfluidic designs discussed in **Chapter 5** as indicated by trial 1 in Table 3. While the PI resin added an element of design versatility, it required optimization of the curing process and spin coating to create a uniform thin film without defects or bubble formation to mimic the reproducibility of the Kapton tape substrate. Furthermore, the leftover uncarbonized resin poorly adhered to the silicone conformal coating and PDMS indicating the need to remove the carbonized product from the initial substrate or find a compatible encapsulation matrix to address the porosity visible in Figure 16. This phenomenon led to the decision to return to Kapton tape as the substrate where it was proposed that the tape be removed following grafting into a suitable material.

4.3 Results and Discussion

LINC Electrode Design

Functional electrodes were fabricated by transferring the carbonized Kapton tape onto a PDMS coated glass slide with laser-etched silver tracks. A rectangular area of Kapton tape measuring 2mm by 5mm was carbonized, sealed, re-exposed with a scalpel, and back connected *via* soldering a stainless-steel wire to the exposed silver track to create the electrodes depicted in Figure 16B and 16C. A surface larger than the desired electroactive area was carbonised to create a more reproducible product

based on the spatial resolution of the laser. It is essential to achieve a total electroactive area in the upper micron range for compatibility with our data acquisition system. Given these considerations, it was necessary to seal the carbonized area and then re-expose to create the desired electroactive surface area. To re-expose the sealed carbon, we attempted perforation of the top layer of PDMS with a needle, laser etching, and scalpel slicing. The first two of these methods were unsuccessful and resulted in a "no signal" oscilloscope.
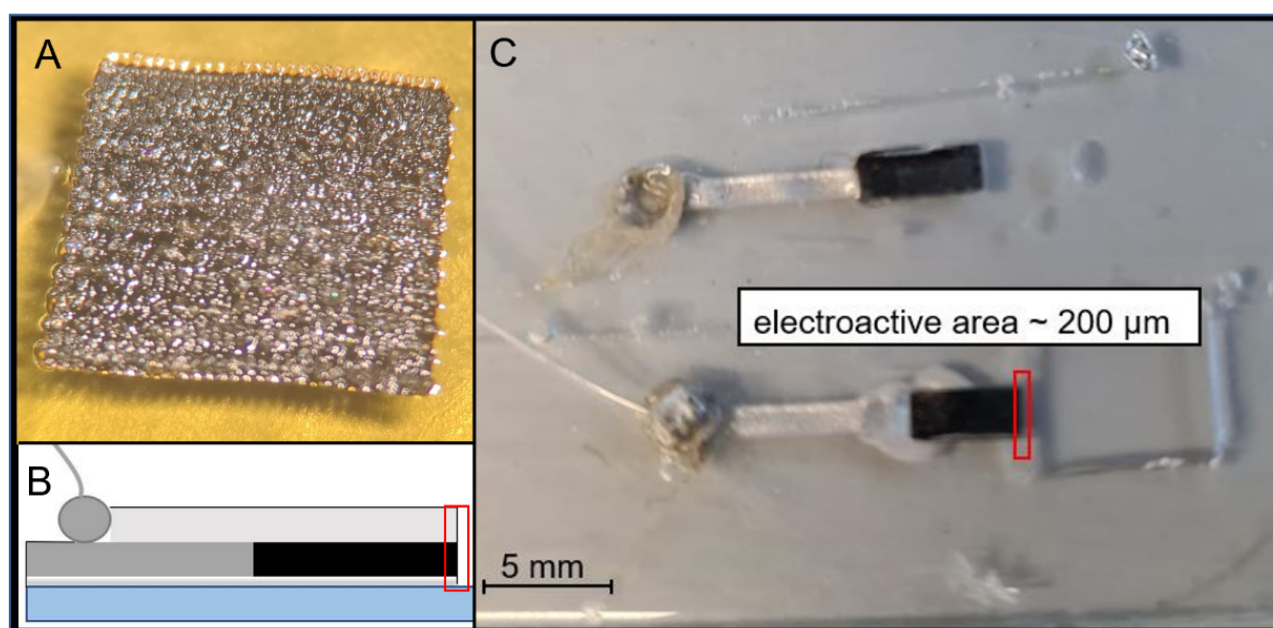

Figure 16

A) 40x image of a 2mm-by-2mm square of carbonized polyimide to exhibit its microstructure. It is clear that the resolution of the laser is not suitable to create exact shapes in the mid micron range. B) a lateral view of the materials layers of the C) LINC electrodes. The maximum geometrical area is determined by multiplying the length characteristic of the cut carbon by the thickness of the Kapton tape. Pyrolysis results in substrate shrinkage, so the true geometric area will be smaller, and can only be determined by high resolution microscopy or certain electrochemical experiments.

There was one trial of laser etching that resulted in an unstable and overloaded signal. It is also likely that needle perforation did not expose enough of the carbon to achieve the minimum sensitivity required for FSCV with our data acquisition as indicated by the oscilloscope signal. Furthermore, the polydimethylsiloxane (PDMS) is extremely hydrophobic, so it is also possible that the solution did not make contact with the carbon due to repulsion by the encapsulating PDMS. To address the

hydrophobicity of the PDMS, a laser exposed electrode was plasma treated, which resulted in an oscilloscope signal similar to Figure 15C. Many trials of laser etching were performed by optimizing the laser power and speed parameters. None of these resulted in a functional PDMS encapsulated LINC electrode. Finally, based on previous work[62], a scalpel was used to laterally re-expose the encapsulated carbon, exhibited in Figure 16B, which immediately produced a functional electrode with an oscilloscope signal like the one depicted in Figure 15B. The anisotropy of pyrolytic carbon has been well characterized[99], so it is possible that exposing the lateral plane as opposed to the aerial plane (in the case of laser etching/needle perforation) was key to the success of this method. Furthermore, the SEM of our LINC electrodes illustrated by Figure 18 reveals that this material resembles anisotropic carbon.

LINC Electrode Characterization

One a functional electrode configuration was achieved based on a healthy oscilloscope signal, the electrodes were evaluated via background scans, noise characteristics, and injections with serotonin. Background currents with CPE, CFME, and LINC electrodes were measured using the Jackson waveform for comparison and are depicted in Figure 17. Comparing these CVs elucidates some of the properties of the electrodes, such as capacitance, to permit further optimization. Blank files were collected for a CFME and a CPE to compare the characteristics of the noise for each material and to determine a performance criterion for the LINC electrodes. Blank files were also collected from different LINC electrodes to determine how slight changes to the fabrication protocol affected the noise of the electrode as exhibited in Figure 20. This work indicates that both the background current and the variation and magnitude of the noise suggests an electrode's suitability for measurements. Based on the excellent electrochemical performance of CFMEs, an ideal electrode would exhibit low background current, a signal to noise ratio at least that of a CFME, and noise variation of > 0.04 nA. A metric for signal to noise in this work was calculated by dividing the maximum current of a signal by the standard deviation of the noise.

Background Current and Cyclic Voltammograms

Cyclic voltammograms acquired in the absence of the analyte of interest reveal the background current of the system. The background current is characterized as the current resulting from applying a potential to the electrode in addition to residual currents caused by auxiliary reactions at the electrode surface. The background current (I_c) is proportional to electroactive area of the electrode A_e, the double layer capacitance (C_{dl}), and the scan rate (v) based on equation 3[49]. The background current is also proportional to the area of the CV, which leads to the relationships between the area of the background CV (A_{cv}), electrode area, scan rate, potential window (ΔV) and double layer capacitance illustrated in Equation 4. Note that the double layer capacitance is a specific capacitance, typically in the units of microfarads per centimetre squared.

$$I_c = A_e C_{dl} v \quad (3)$$

$$A_{cv} = A_e v(\Delta V) C_{dl} \quad (4)$$

It is not possible to determine the electroactive area of an electrode based on estimation with conventional geometric equations for surface area. For example, if we were to assume a perfectly smooth surface with the dimensions of a CFME with a radius of 7 μm and a length of 10 μm, the surface area of the CFME would be approximately 700 μm^2. Previous work determining the electroactive area of a CFME this size via background current estimated an electroactive area more than three times the estimation based on the calculation of the surface are of the cylindrical carbon fiber alone[100]. Using this ratio, the electroactive area of a CFME as fabricated by our methods would be 18000 μm^2, with the geometric area being approximately 6000 μm^2. This discrepancy is due to the surface topography and microstructure of carbon fibers where its length has been characterized as striated[101] and the tip has been characterized as rough. Previous work has described this discrepancy as a "roughness factor"[102].

The CFME had a larger background current than the CPE and the LINC electrode as depicted in Figure 17. This is expected because of its cylindrical geometry and size compared to the other two planar

electrodes. However, CFMEs do generate notoriously low background current per unit area and exhibit lower capacitance in comparison to other carbon materials due to the exposure of the highly ordered a-plane along the sides of the cylinder[103].
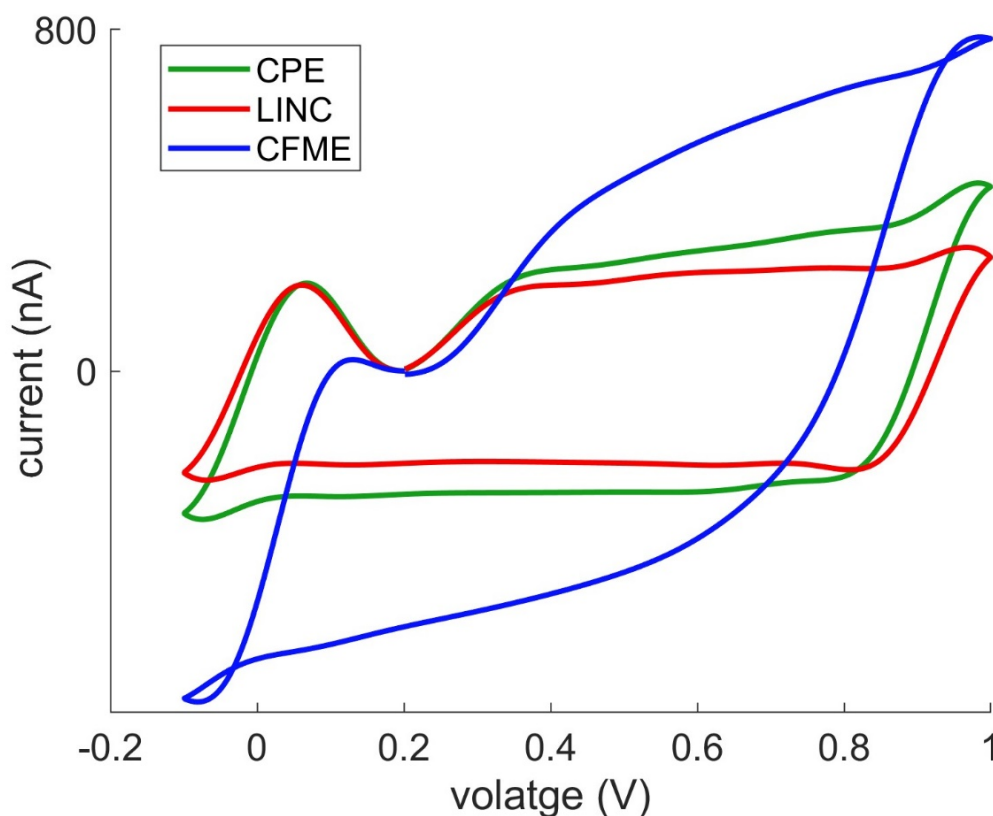

Figure 17

CVs showing the background currents of different carbon materials scanning with the Jackson waveform. Note that despite the fast scan rates, there is no background subtraction performed because no analytes are being measured.

The compositional heterogeneity of composite electrodes such as CPEs is associated with fewer electroactive particles per area, leading to a lower background current, conductivity, and capacitance[49]. The fabrication protocol of the LINC electrode also makes this electrode a composite, though it should still have a higher ratio of electroactive material to filler than the CPE. The similarity of the shape of the background CVs for the LINC electrode and the CPE suggests that the carbon material for these electrodes may be electrochemically similar in comparison to the CFME. The CPE should exhibit the lowest background current per unit of electrode area in comparison with other

carbon materials due to its high percentage of insulative filler. Reported capacitances for carbon materials vary within a range of approximately 70 µF/cm^2 with ordered materials such as boron-doped diamond having lower capacitances and disordered materials such as polycrystalline graphite having higher capacitances because of structural defects that add charge carriers [56]. Experimentally determined capacitances vary with the solutions used in the electrochemical cell, and hand-fabricated carbon materials vary greatly, therefore exact calculations using literature reported capacitances collected in different solutions are not relevant.

An estimation of the total geometric surface area of the LINC electrode yields a maximum of 200µm^2 (depicted by Figure 16) by multiplying the width dimension of the lasered rectangle by the thickness of Kapton tape. The true geometric area will be smaller because the laser does not penetrate the entirety of the tape. In comparison, the geometric area of the CPE will be larger than the LINC electrode given that buffing the tip of the micropipette with an abrasive leads to a diameter larger than that of a carbon fiber. If we assume similar capacitances, we can assume a larger geometric is responsible for the comparative increase the background current between the CPE and LINC electrode based on the CVs in Figure 17. However, without additional experiments to estimate the individual capacitances of each electrode material, we acknowledge that the area of the background CV may not be a good indicator of the relative sizes of the electroactive areas of these electrodes.

Scanning Electron Microscopy

High resolution imaging techniques such as atomic force microscopy, scanning electron microscopy, or scanning electrochemical microscopy can be useful in accurately determine the electroactive surface area of a microelectrode. Scanning electron microscopy (SEM) was used to image the rough surface topography and complex microstructure visible in Figure 18. This inherent variability in surface structure creates difficulty in characterizing the electroactive area of the material but is also responsible for its reactivity. This variability is caused by both the nature of the fabrication protocol and the introduction of the material intro the electrochemical cell. For example, when introducing a

CPE into solution, the liquid may penetrate through the carbon paste mixture over time. This permits the solution to make unintended contact with the surface area of unexposed graphite particles in the electrode, causing an uncontrolled increase in electroactive surface area. Fabrication protocol issues such as poor adhesion between the electroactive material and the insulator may also lead to unintentional exposure of a larger electroactive.
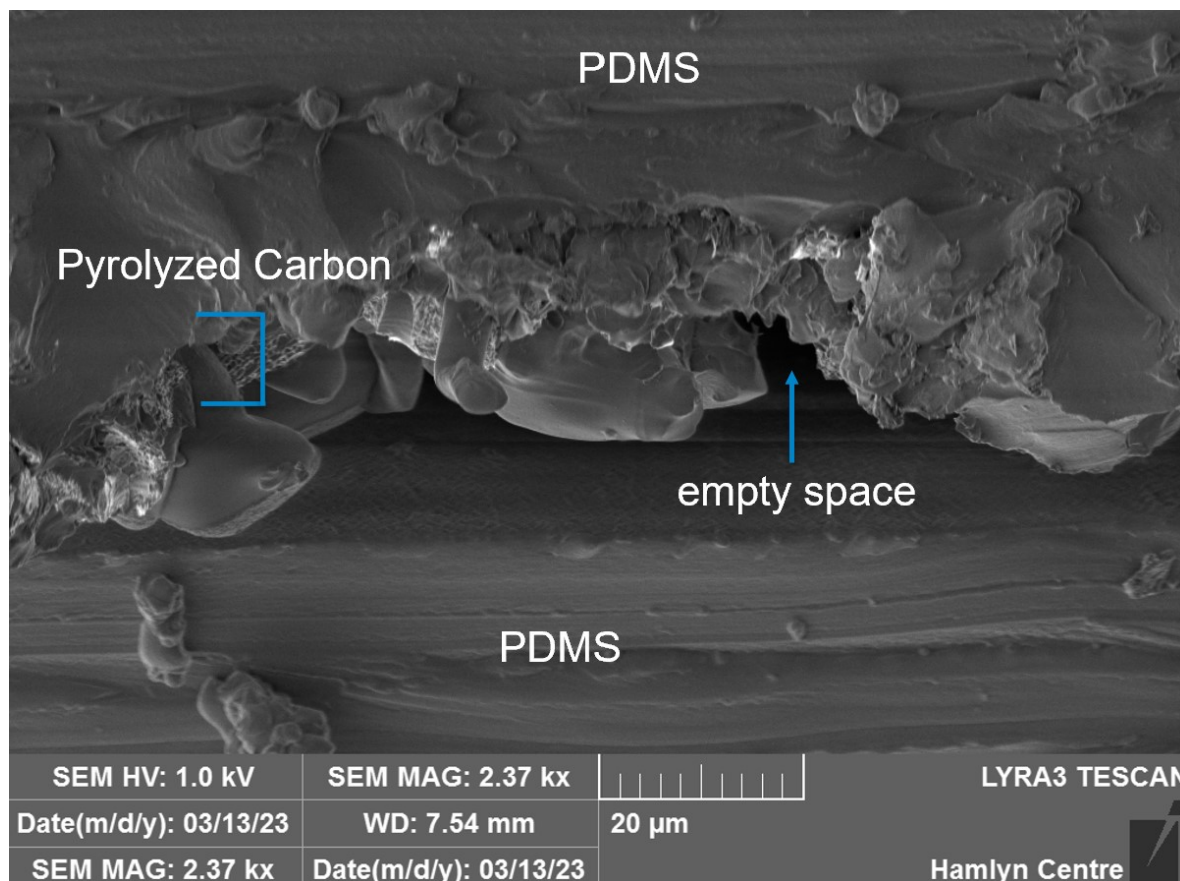
Figure 18

SEM of electroactive plane of LINC electrode. Layers of PDMS above and below the electroactive area are characterized by an ultra-smooth appearance. Empty space is indicated by the dark area under the layer of pyrolyzed carbon. The pyrolyzed carbon is illustrated by the curved band with rough surface morphology in the centre of the image. This morphology is indicative of cellular anisotropic networks, which has the ideal conductivity and surface characteristics for fast electrochemical kinetics[104].

Electrode Noise

Sampling the baseline noise of electrodes for comparison with electrodes of different configurations and with CFME is predictive of their quality for FSCV measurements. The noise of the electrode must be sufficiently low to facilitate measurements in the low nA range for acquisition with our FSCV system. When system parameters are controlled (including the electroactive area of the electrode), the noise of an electrode is primarily influenced by the capacitance of the material, or the ratio of the change of the electric charge in response to a change in an applied potential[50]. The capacitance of a material is affected by its molecular structure[105], density, and defect presence, all of which also influence parameters such as electroactive area and conductivity. This is supported by previous work comparing the capacitance and noise of CFME and carbon disk microelectrodes [50], which are both fabricated with carbon fiber, but exhibit different noise levels and capacitance. Though they are created from the same carbon fiber, these electrode types have different configurations where distinct planes of the carbon material are exposed. Furthermore, carbon disk microelectrodes inherently expose less electroactive carbon in comparison with CFME in how they are made, so the surface area does not account for the observed increase in noise. CFME have both the a and c planes exposed whereas carbon disk microelectrodes only expose the c plane, which has a higher defect presence and has a less ordered microstructure. It is therefore expected that any planar carbon with high defect density will produce more noise than a CFME, where the majority of the surface area of the cylinder is composed of the highly ordered a plane. This is observed in Figure 19 where the baseline of the LINC electrode is more variable than the CFME as calculated by the standard deviation of the baseline sample. In addition to the molecular structure of the carbon material, the organization of the insulator and the electroactive material also impact the baseline noise of the electrode. It has been previously observed that the capacitance of an electrode is increased by electrode porosity, roughness, and poor adhesion between the insulator and conductive material[49, 50].
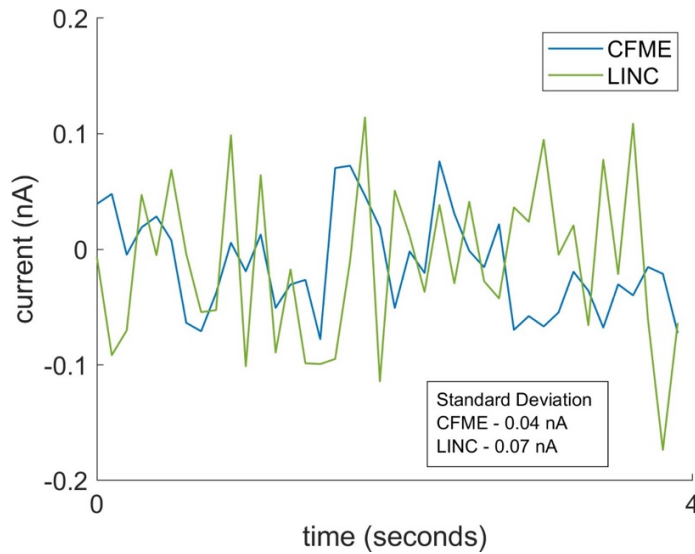
Figure 19

A 4 second sample of the baseline of either a CFME (blue) or a LINC electrode (green) with calculated standard deviation across the interval.

Given that an increase in capacitance causes a direct increase in voltage noise, based on equation 5, it is necessary to ensure a mechanically secure adhesion between the insulating material and the electroactive material. Voltage noise contributes to the variation in measured current as a result of electrode capacitance. In Equation 5, C in the electrode capacitance, f is the frequency, and $\sigma_e{}^2$ is the variance of the potential across the capacitive interface.

$$voltage\ noise = (2\pi C)^2 \int_{f_{lower}}^{f_{upper}} \sigma_e{}^2 f^2 df \qquad (5)$$

This is supported by the data in Figure 20 where baseline samples from electrodes of different configurations are illustrated. Electrode B is the same as electrode D, except that the PDMS encapsulation had been cut into a triangular shape for insertion into the flow cell. Simply cutting the PDMS perturbed the adhesion of the layers of the electrode leading to an increase in noise in comparison to electrode D, visible in Figure 20. Earlier electrode configurations using PI resin cured onto a 3D printed mould resulted in baselines A and C. The configuration of electrode A, listed in trial 1 of table 3, resulted in a broken oscilloscope signal indicating an exposed back connection. This electrode was likely not appropriately sealed between layers, allowing the buffer solution to make

contact with the metal back connection. Metal typically produces less noise than carbon because of its lower resistivity resulting in less thermal noise[106], which is apparent in baseline A. The configuration of electrode C, assembled similarly to electrode A, led to a low amplitude, but viable oscilloscope signal that later transformed into a signal indicating an exposed back connection, and was no longer viable. Baseline C, acquired while the oscilloscope signal was stable, exhibited the largest variation in noise of all electrodes in Figure 20.
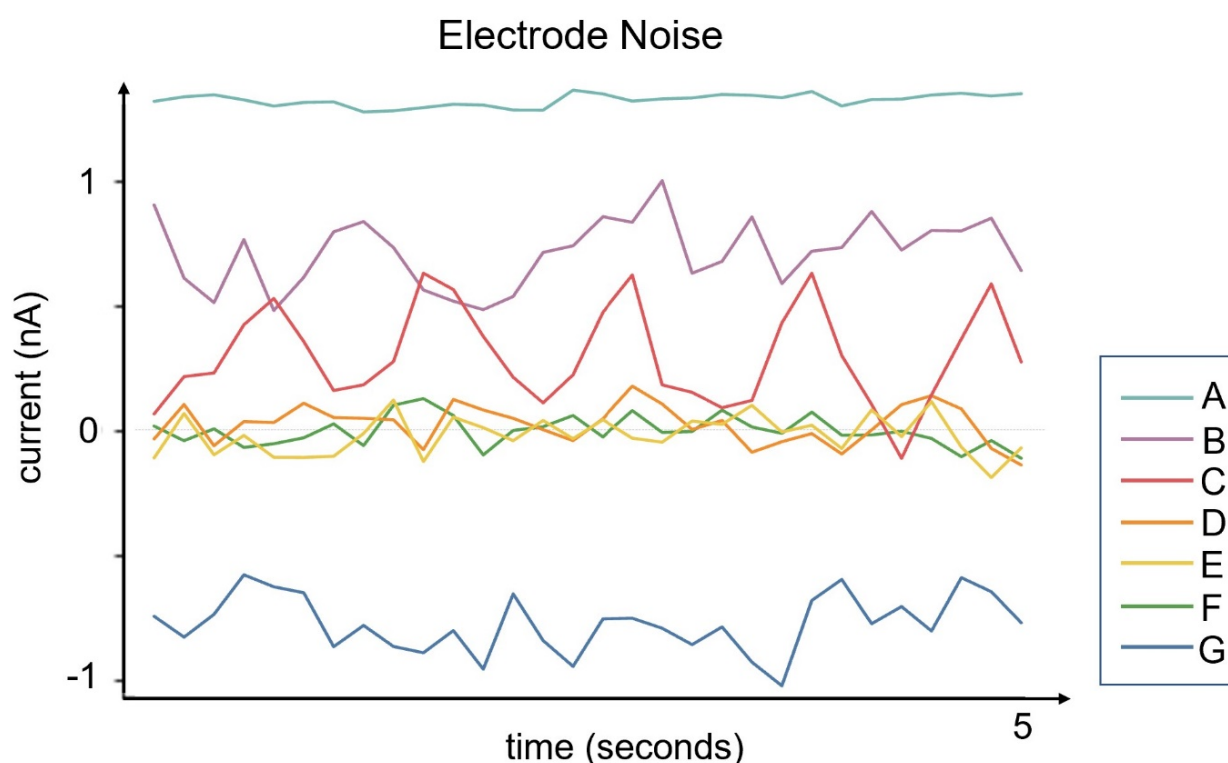

Figure 20

A 5 second sample of the baselines of different electrodes. A and C were noise samples collected from previous LINC electrode configurations, similar to trial 1 listed in table 3, that yielded a temporarily viable oscilloscope signal. B is the noise sample of a LINC electrode that was cut and modified for compatibility with the flow cell. D-F are samples from LINC electrodes that were suitable for calibration, while G is a baseline sample from the most optimized CPEs we fabricated.

Based on the instability of the signal over time, electrode C was likely not appropriately sealed like electrode A, but the change in electroactive area over time as the buffer percolated through the layers caused excess noise. The baselines for electrodes A-C were shifted above zero while electrode G, a carbon paste electrode, was shifted below zero. In contrast electrodes D-F were not shifted, and were

viable for serotonin measurement, suggesting that the baseline shift is also an indicator of electrode quality. In addition to shifting, the baseline of electrode G has a standard deviation of 0.64 nA, which is an order of magnitude greater than a functioning LINC electrode or CFME. The noise levels of D-F could be further improved by modifying the fabrication protocol to minimize or even eliminate the empty space visible under pyrolyzed carbon in the SEM image of the LINC electrode in Figure 18.

Measurement of Serotonin

After initial screening *via* monitoring the oscilloscope signal, acquiring background CVs, and sampling the noise of the electrode baselines, the electrodes were subjected to injections of 1 micromolar serotonin. Serotonin was the analyte of choice because of its use in previous work in the development of the flow cell in **Chapter 3**. It is important to note that despite using the same concentration of serotonin, there will be variability in the sensitivity between different electrode types (LINC, CPE, CFME) caused by differences in the electrode geometry. More specifically, the flow cell is optimized for the cylindrical shape of a CFME, not a planar electrode, therefore the acquired current is expected to be lower for the planar electrode. To minimize this effect, a direct injection onto the electrode was performed for the LINC electrode to recapitulate the optimized fluid transport encountered in the flow cell. The direct injection is visible in Figure 22 where it is clear from the colour plot that the current does not change for the duration of the injection.

Figure 21 depicts a cyclic voltammogram for a LINC electrode, a CFME, and a CPE in response to a 1 µM injection of serotonin. The maximum current for the CFME is 16nA, the maximum current for the LINC electrode is 15nA, and the maximum current of the CPE is 30.9. Using the integrated area of the background CVs depicted in 17 as a rough estimate of electroactive area (making the assumptions that the capacitances are similar for these materials), the LINC electrode has a sensitivity of 0.039 nA per unit area, the CFME has a sensitivity of 0.025nA per unit area, and the CPE had a sensitivity of 0.064 nA per unit area.
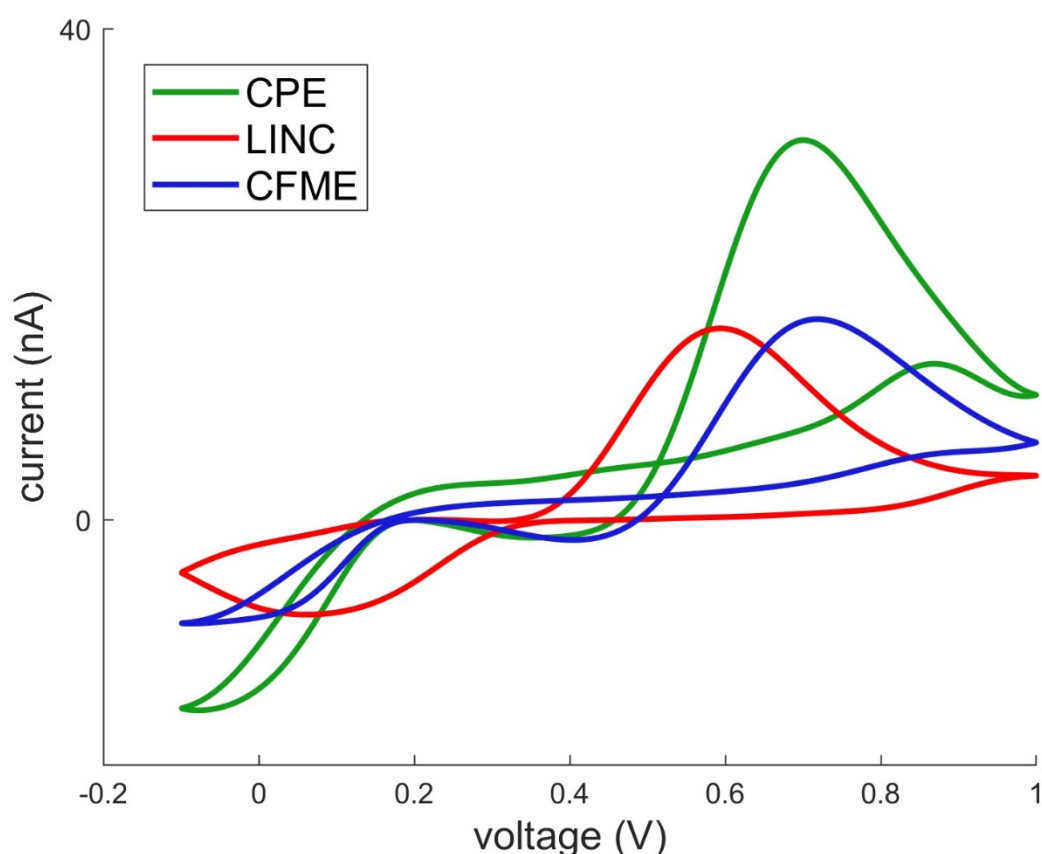
Figure 21

Cyclic voltammograms of unmodified CFME (blue), LINC (red) electrode, and CPE (green) in response to a 1 micromolar injection of serotonin using the Jackson waveform. The peak current of the LINC electrode CV occurs at 0.59V, the peak current of the CFME CV occurs at 0.71V, and the peak current of the CPE occurs at 0.69V.

It is expected that the sensitivity of the both the LINC electrode and the CPE would be higher than the CFME because of the higher proportion of c-plane carbon to promote the adsorption of serotonin. The rough surface and defect presence of the LINC electrode is likely also responsible for the catalytic downshift of the serotonin peak in comparison to the CFME, which is visible in Figure 21. In comparison with the CPE, the downshifted peak of the LINC electrode suggests that encapsulation with PDMS creates a composite with a lower percentage of filler than the CPE. Moreover, there is an increase in the magnitude of the reductive peak that suggests improved electrochemical kinetics from the CFME and the CPE. Though the magnitude of current is higher for serotonin with a LINC electrode and a CPE, the noise is higher leading to signal to noise ratios that are lower than a CFME. Considering

the standard deviation of the noise of the LINC electrode and the CFME listed in figure 17, the CFME has a signal to noise ratio twice that of the LINC electrode and 10 times that of a CPE for a 1 micromolar injection of serotonin.
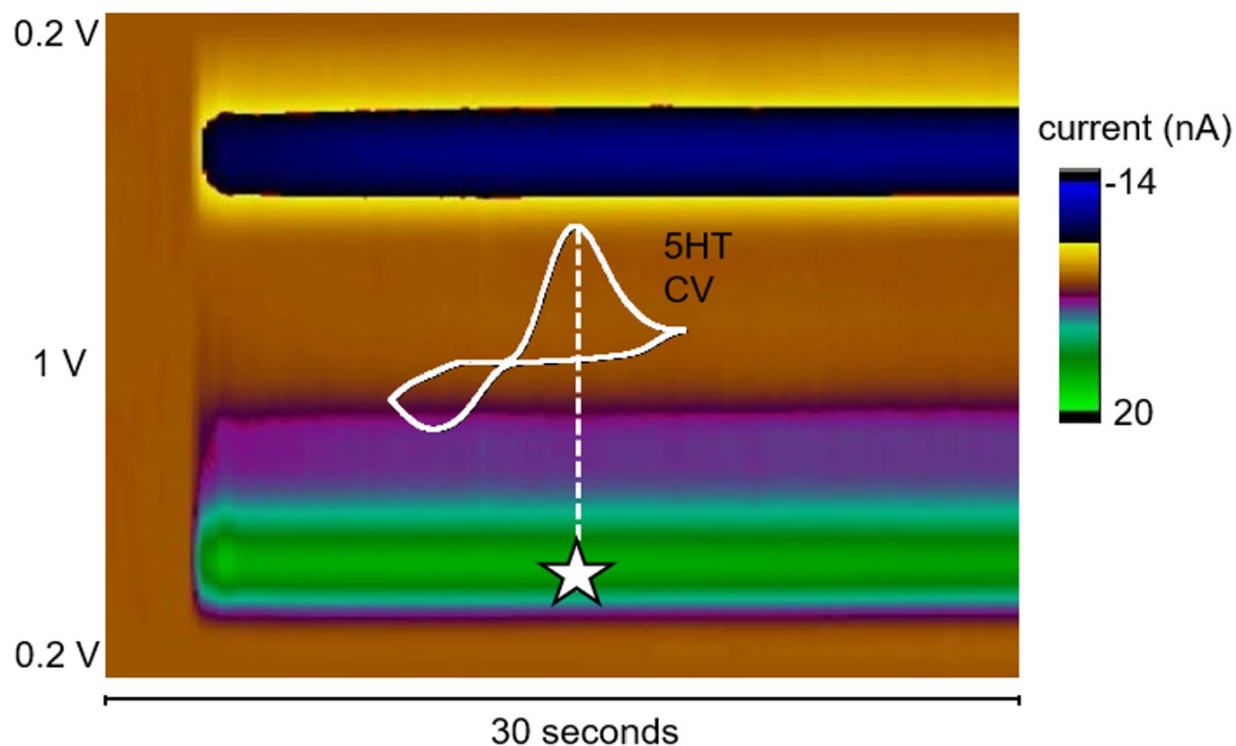

Figure 22

Shows the full colour plot of the serotonin injection on the LINC electrode depicted in Figure 16. Oxidative current is characterized by the bright green while the reductive current is characterized by royal blue. The corresponding cyclic voltammogram at the time point indicated by the star is superimposed onto the plot.

Figure 22 illustrates a direct injection of serotonin performed at a LINC electrode. As previously mentioned, a direct injection was performed for the LINC electrode for a better comparison to an injection at a CFME in the flow cell where the fluid transport is optimized. A beaker injection using a micromanipulator would have provided suboptimal transport of the analyte to the LINC electrode because it was mounted on a glass slide and because of the dimensions of the electroactive area. The LINC electrode has a length (~2 mm) that would prove disadvantageous for the diffusive transport characteristic to a beaker injection. A beaker injection would not have exhibited a stable current value

as depicted by the long green streak in Figure 22. The quality of the direct injection prompted its use in the calibration protocol of the LINC electrode. A calibration using a LINC electrode was performed after the successful injection of serotonin to further probe the electrode's behaviour in comparison to a CFME. A calibration curve was generated with concentrations from 50nM to 500nM, higher than the 10nM to 100nM range examined with CFMEs in the flow cell. The calibration was performed at higher concentrations because the larger magnitude noise of the LINC electrode did not permit reliable measurements below 50nM. The calibration is reasonably linear until 100nM after which the adsorptive sites of the electrode begin to saturate. This phenomenon is visible in figure 23 and is consistent with the well characterized behaviour of a CFME.
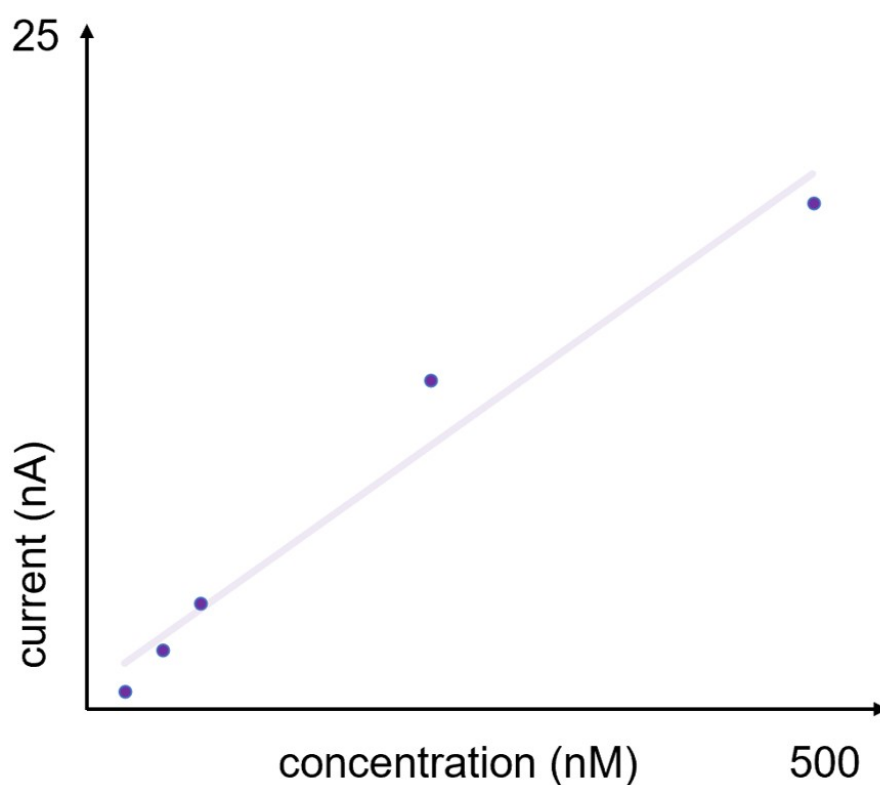

Figure 23

illustrates a calibration curve performed with an unmodified LINC electrode using serotonin concentrations of 50nM, 75nM, 100nM, 250nM, and 500nM. This calibration was performed in the physiological salts buffer listed in the methods section.

The sensitivity is lower than that of the injection performed to generate the CV depicted in figure 21 because many serotonin injections had already been performed on this LINC electrode. Previous work[107] has suggested that a rougher surface chemistry limits the electropolymerization of analytes onto the electrode surface, however a decay in sensitivity was still observed with successive injections. Further experiments are required to determine if the magnitude of this decay is significantly decreased from that of a CFME.

The electrode pre-treatment performed to acquire the flow cell calibrations in **Chapter 3** was repeated for a LINC electrode following its calibration as depicted in Figure 23. Interestingly, there was an increase in signal from 3nA to 56nA as illustrated in Figure 24, which is far larger than the signal increase observed in Figure 12 where the same experiment was performed with a CFME.
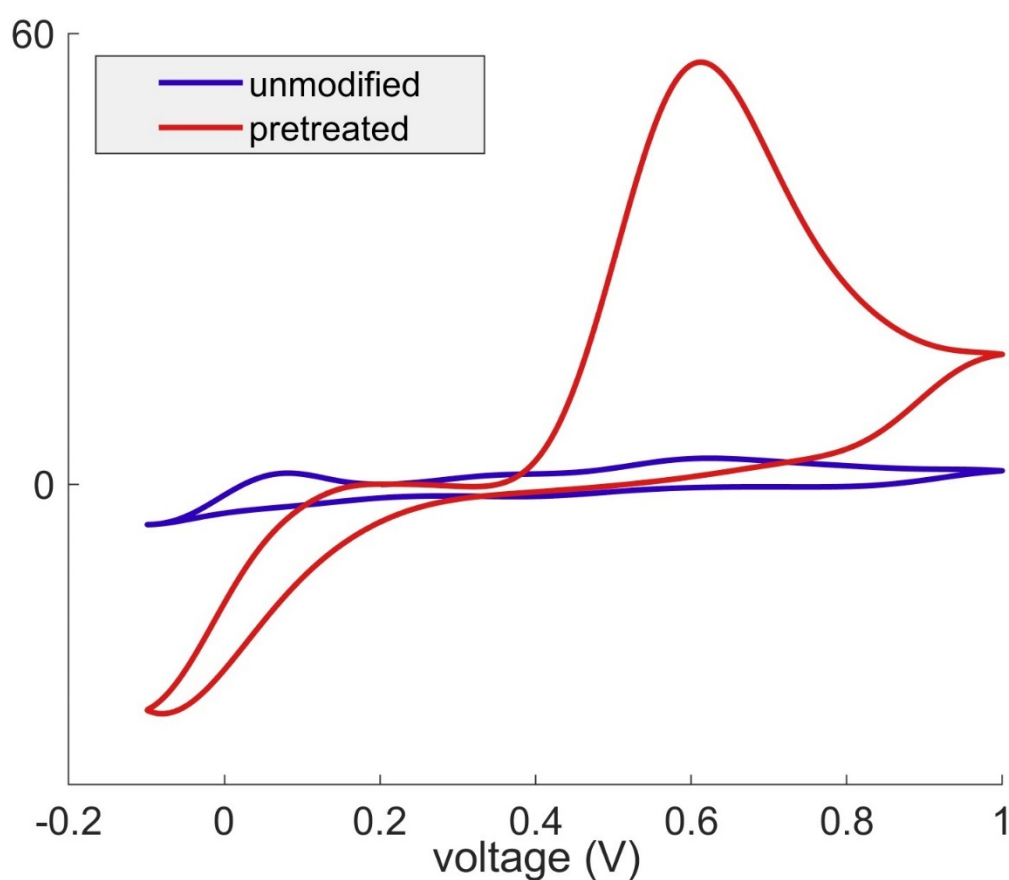

Figure 24

A comparison of the cyclic voltammograms of a 1 micromolar injection of serotonin at either an untreated (blue) or pre-treated (red) laser induced carbon electrode.

It is possible that more disordered materials are more susceptible surface functionalization caused by overoxidative etching. Additionally, there is a reduction of the magnitude of the reductive peak observed in CVs acquired with untreated LINC electrode suggesting that this changes the surface chemistry of the electrode to promote kinetic favourability of the oxidative reaction. Previous work states that edge plane graphite has an oxidative potential limit of 1.3V while the basal plane has an upper limit of 1.7V[108]. Based on these limits, the use of the extended Jackson waveform would oxidize an edge plane dominant material (laser induced carbon) to a greater extent than a material that is basal plane dominant (carbon fiber).

4.3 Conclusions

CFMEs do not have the capacity or versatility for simple integration with *in vitro* systems due to their fragility and need for manual placement. Furthermore, the process of fabrication for CFMEs is time consuming and prone to variability during production that is not suitable for commercialization. In this chapter, we presented the development of a LINC electrode that addresses limitations associated with fragility and ease of integration. This electrode design also exhibited improved sensitivity per unit area and electrochemical kinetics. Further optimization of the design process can further enhance these characteristics. Additionally, the fabrication process developed in this work is rapid and inexpensive in comparison to CFMEs. Finally, this work provided a feasible candidate for integration with a microfluidic device to create a screening platform for neurochemical mechanisms of psychiatric illness in organoid models.

Chapter 5 – The Development of a Microfluidic Flow Cell with Integrated Carbon Electrodes

5.1 Introduction

Comprehensive analysis of *in vivo* neurochemistry is challenging to perform non-invasively, which can be addressed with the development of *ex vivo* models of the brain. The use of organoid technology to replicate neurochemical functions of the brain has shown encouraging results[109, 110], however, it poses its own difficulties. More specifically, measurements from cells with FSCV is a tedious process that requires expensive micromanipulators, fragile CFMEs, and optimization of external stimulating electrodes. Furthermore, the analysed cells may begin to undergo apoptosis and release cytotoxic species if the duration of the experiment is prolonged beyond a few hours. Performing quick experiments with FSCV in cells is limited by the time required to position the electrode in a section of culture with a large enough release to generate a signal. Furthermore, sometimes this release is not suitably concentrated for differentiation from other chemical species. In previous chapters, we have created electrodes that are suitable for integration into microfluidic devices that may encompass these *ex vivo* models. In this chapter we actualize design concepts of integrated sensing devices for *ex vivo* models.

Microfluidics allows precise control over fluid flow, mixing, and reaction conditions, which is suited for mass-transport mediated electrochemical reactions[111, 112]. Microfluidic devices only require small sample volumes, which is advantageous where samples are limited or expensive, and reduces fluid turnover time in actuated systems. The size of microfluidic devices improves portability, which can be logistically crucial for clinical diagnostics. Calibration of electrodes for FSCV of neurotransmitters requires optimization of the flow injection profile[48]. The flow injection profile is primarily influenced by the time to signal acquisition, dead space, and dispersion. All these parameters may be controlled and minimized using appropriately designed microfluidics.

Microfluidic devices are also particularly advantageous for the development of *ex vivo* models such as organoids because the introduction of controlled flow permits constant fluid exchange. This alleviates some of the issues that arise due to poor transport of nutrients in static cell culture. These issues include abnormal or uneven growth, cell death, and deviation from *in vivo* physiology[113]. Many organoid models are therefore developed on a microfluidic platform termed "organ-on-a-chip"[114]. The development of an organ-on-a-chip platform would dramatically increase the viable duration of experiments for the monitoring of neurotransmission.

The ideal device would therefore harness the capabilities of microfluidics for both calibration and organ-on-a-chip, however at this stage our scope includes calibration and simplifying measurements from cells. In this chapter, we present the development of a microfluidic device that is compatible with the PDMS encapsulated carbon electrode developed in **Chapter 4**. This device provides a precursor for the development of a device capable of optimally positioning cells for direct measurement with FSCV depicted in Figure 25.
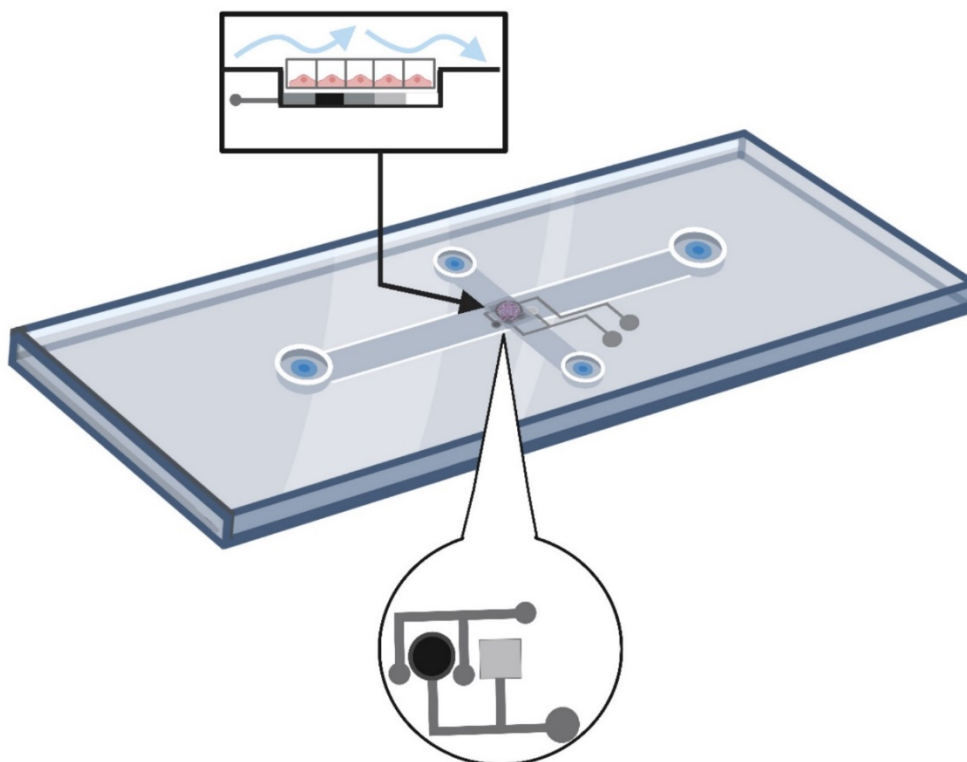

Figure 25

Design concept of PDMS based microfluidic device with integrated LINC electrode, reference electrode, and stimulation electrode electrodes The bubbles provide a closer view of the circuit design and the positioning of the cells into the indent of the cross section. There are 2 inlets and 2 outlets as shown at the ends of each channel.

In this design, the vertical channel permits the introduction of calibration standards and perfusion of drugs while the horizontal channel allows the cells to be fluidically positioned into an indent at the intersection of the channels. The premise of enacting fluidic control over the position of cells is key in many biologically relevant such as flow cytometry. First, critical design parameters are presented, then an overview of the iterations of produced devices is examined with relevant data, and finally, a foundation of an integrated platform is offered for application to future work.

5.2 Concepts in the Design of Microfluidic Devices

Fabrication Method

The fabrication method is a critical consideration in the design of a microfluidic device that is typically selected based on available resources and the desired functionality of the device. More specifically, the desired resolution and complexity of the features of a device and substrate materials dictate compatible fabrication protocols. Other factors such as the sought speed of production and biocompatibility are also relevant for devices with the potential for commercialization for clinical applications. Most fabrication techniques can be categorized into 3D printing, etching/lithography-based methods, machining, and moulding. Oftentimes, more than one of these techniques is used in a single fabrication protocol. Indeed, this is the case in our work where 3D printing is used to create custom fittings, parts, and/or a mould in addition to machining (creating taps for inlets) and moulding.

3D printing

There are numerous 3D printing techniques, however only those relevant to this work will be discussed. Stereolithography (SLA) and fused deposition modeling (FDM) based printers are widely available, with higher resolution SLA having a resolution in the hundreds of microns. SLA involves the laser curing of a photopolymer while FDM uses heat to melt a thermoplastic filament for deposition on the build platform. The Formlabs printer used in this work has a minimum feature resolution of 25 microns. A version of the flow cell presented in **Chapter 3** was printed with a benchtop FDM printer,

but the resulting product did not have the resolution required for compatibility with liquids. 3D printing is an attractive strategy because it permits rapid prototyping, which is evident from Figure 29 where 11 main prototypes were tested over a period of a year and a half. Many intermediary iterations characterized by minor design changes were not included in this list of prototypes. 3D printing also permits complex design features that are not as easily produced with photolithography-based techniques[115], which require flat patterns. The major disadvantage of directly 3D printing microfluidics is low resolution and resulting surface roughness that makes it nearly impossible to create devices that require good adhesion for sealing. This phenomenon is responsible for excessive leaking caused by differences in surface roughness of the glass bottom and the 3D printed top in prototype 1, pictured in Figure 26. Furthermore, many 3D printing materials are proprietary, which makes it difficult to predict the chemical compatibility of the printed material for the desired application where literature does not exist. For example, the Formlabs resin cannot be directly used to mould PDMS because its resin prevents curing. Certain commercial 3D printing systems, such as the Nanoscribe, use two-photopolymerization to achieve sub-micro resolution, but these systems are expensive and cannot create parts larger than a few centimetres.
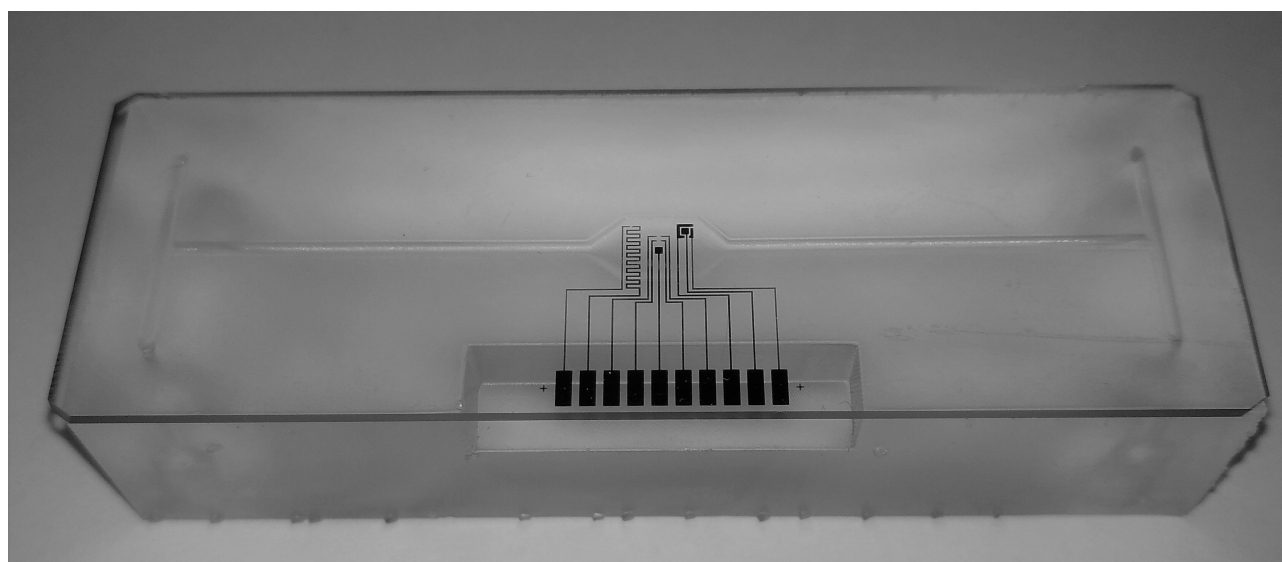

Figure 26

First prototype of 3D printed microfluidic device in this work with two T junctions, two inlets, two outlets, and a channel allow contact of introduced fluid to the metal sputtered circuit on the class slide. The glass slide functions as the bottom half of the channels while the 3D printed portion functions as the top.

Etching/Lithography

Etching/lithography-based techniques are more time consuming to perform than 3D printing because of training time, clean room requirements, and process complexity. These techniques may also be more expensive due to the number of reagents and equipment required. Etching can be achieved chemically[116], with plasma (specifically reactive-ion)[117], or a laser[118]. These techniques are best suited and well-characterized for silicon wafers or glass although instances of directly wet etching PDMS are reported in the literature with a resolution in the hundreds of microns[119, 120]. Chemical or "wet" etching is a more dated technique with a lower resolution than plasma etching or photolithography and creates inexact features. This is caused by isotropic etching of the substrate by the chemical responsible for etching resulting in indents that appear "droplet-like" as illustrated in Figure 27A. Furthermore, this technique requires the use of many reagents, some of which are harsh chemicals. Conventional photolithography can reach a resolution of 100nm[121] and produces the square-like indentations visible in Figure 27B.
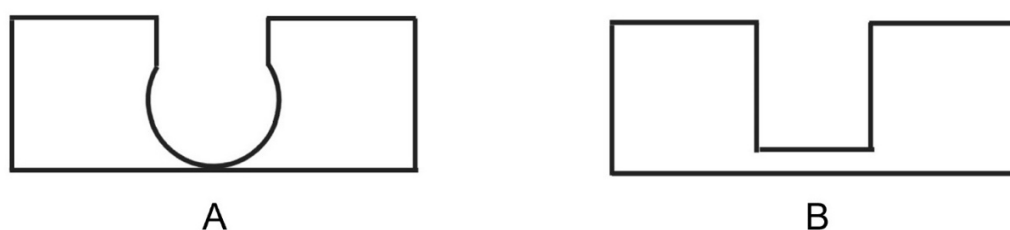

Figure 27

A comparison of the indentations produced by isotropic wet etching (A) versus anisotropic etching characteristic to conventional photolithography (B).

Commercial plasma systems produce three dimensional features in the low micron range and do not require a "mask", or stencil, to create patterns. Aligning the masks creates limitation on the size and orientations of potential devices that are not encountered with 3D printing.

Direct laser writing via vectorized graphics with a CO_2 flatbed laser cutter also does not require a mask but can only produce 2D structures with resolution in the hundreds of microns. Femtosecond lasers can achieve a higher resolution, but still suffer the two-dimensional limitation in most cases[122]. In this work, it was attempted to directly laser etch PDMS, but fine control of the shape of the channels were not possible. Furthermore, the resulting channels exhibited a rough surface that is not ideal for a device where the acquisition technique demands as rapid of a response time as possible.

Machining and Moulding

The first flow cell iteration depicted in Figure 6B was created by milling to create the channel, drilling to create the cycling well, and tapping to create the threads for the inlet. Drilling, cutting, milling, tapping, and boring are all machining techniques that occur on the macro-scale (down to the low mm scale) and are not suitable for creating microfeatures. All inlets and outlets in the 3D-printed devices were created via taping to permit the use of screw-in fittings that were already used in the flow injection system. The taps created more reliable threads than the 3D printer, which suffered from large variability.

Moulding techniques require the creation of a "master mould" that acts as the reverse or "negative" of the desired device. The master mould can be created by 3D-printing, lithography/etching, or machining depending on the desired size and feature resolution of the mould. When designing a mould, the rigidity of the material of the final device determines the rigidity of the moulding material. For example, PDMS is flexible therefore the negative must be rigid to allow separation of the positive from the negative. The compatibility of material stiffness may result in the need to create multiple moulding steps, called indirect moulding, which is the case in this work. Some moulds only require pouring and sequential curing of the moulding material, but others require additional steps such as

injection[123] or compression that add complexity to the process and are less common in the production of microfluidic devices. The "smoothness" of the master mould is another factor essential to the fabrication of quality PDMS devices and may dictate the technique used to create the master mould. Defects of the surface of a master mould create pressure differentials that often result in bubble formation, even with ample degassing, which is visible in the device depicted in Figure 28.
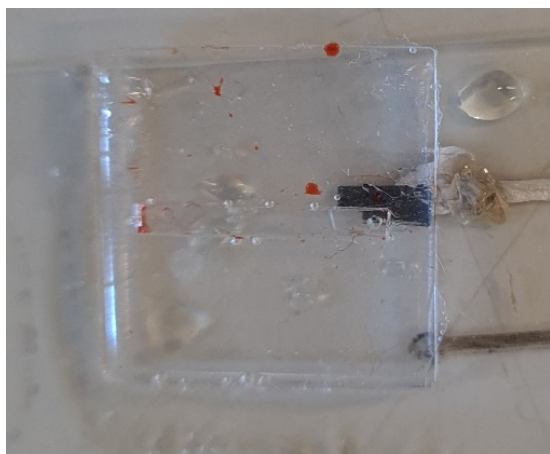
Figure 28

a PDMS Device with integrated electrode where bubbles are present at the interface between the channel and the surrounding material.

Sealing Technique

In cases where the fluidic device is assembled in layers, the selection of an appropriate sealing technique is required to prevent the device from leaking under the pressure demands of the system. A seal can be achieved by various chemical bonding or mechanical sealing strategies. Seals can be designed to be reversible or irreversible based on desired functionality of the device. Mechanical sealing can be accomplished with magnets or fitted parts that apply pressure onto the device to prevent leaking based on the strength of the magnetic field or mechanical force applied. Mechanical sealing is contingent upon the smoothness and the alignment of the separate parts and the distribution of pressure across the surface of the device. Furthermore, mechanical sealing can be challenging with highly rigid materials such as the cured resins used in 3D printing, and was not a successful sealing strategy in this work, which is apparent based on Figure 29.

Irreversible plasma bonding is the most commonly used chemical sealing technique for PDMS based devices onto glass, and typically tolerates higher pressure than reversible sealing techniques[124]. Other irreversible chemical bonding techniques include the use of adhesives, however the difficulty in ensuring a uniform application is a notable disadvantage[125] and was encountered during sealing attempts using silicone conformal coating of the device pictured in Figure 26. Materials such as PDMS that exhibit excellent self-adhesion can create a seal *via* a one-time application of manual pressure or vacuum sealing where only low pressures and flow rates are required for system operation[126].Sealing rough surfaces such as those that are characteristic of 3D printed parts requires the application of a coating to reduce surface roughness and promote adhesion to the material comprising the other side of the device[127]. Sealing both the electrodes fabricated in **Chapter 4** and the devices introduced in this chapter was a significant obstacle during the duration of this work and will be discussed in detail in the results section of this chapter.

Channel Dimensions

Though the overall channel routing of a microfluidic device is monumentally important, the minutia of the dimensions and shape of these channels are also influential on the performance of the device. Moreover, channel dimensions may be more relevant where mixing and droplet formation are not primary considerations. A device with the same routing configuration may perform drastically different with differing channel dimensions, which include the channel include depth, width, height, cross-sectional shape. These features dictate the pressure and forces within the system, which must be optimized to ensure the design does not leak or generate an excessive number of unwanted bubbles. Additionally, the channel dimensions impact the selection of material, compatible hardware/fittings/tubing, and range of appropriate flow rates. Potential channel shapes may be limited by the method used to fabricate the device. For example, when creating master moulds with conventional photolithography, channel shapes are limited to square or rectangular cross sections due to anisotropic etching of the photosensitive material. Furthermore, creating angles in channel depth and rounded channel shapes are precarious with lithography due to challenges in mask alignment.

The configuration of channel inlets are also critical design parameters that influence the performance of the device[128]. Experimentation with inlet configuration was a significant portion of the rapid prototyping in this work as listed in Figure 29. Inlets are often configured above/below and perpendicular to the channel, or above/below and in parallel to the channel. There is greater pressure in the system with perpendicular inlets due to change in direction of the flow stream upon entrance into the device, therefore all final 3D printed prototypes were designed with an inlet in parallel to the channel. This pressure is less significant in PDMS device due to the flexibility of the material.

Hardware, Fittings, and Tubing

PDMS is popular as a device material because its flexibility does not necessitate the use of inlet fittings to create a seal where pressures are below the elastic forces of the material. In certain cases, it is also not necessary to include inlet tubing in a PDMS device where a blunt needle may be directly used to introduce flow into the device. Rigid materials such as PMMA and 3D printed materials require fittings to create a seal between external sources of flow into the device. The tubing for a microfluidic device must be appropriately selected for a system. Tubing diameters that vary too greatly from those of the channels of the device result in pressure differentials that may impede the functioning of the device by compromising its seal or even damaging the device. It is just as important for the tubing materials to be chemically compatible with the fluids introduced into the system as the material of the device itself. All solutions in this work are aqueous and are of physiological pH, permitting a broad range of compatible tubing (Teflon, PEEK). However, FSCV is sensitive to micromovements of the data acquisition system, so rigid materials such as PEEK is preferable to softer plastic materials that move in response to fluid flow. Hardware such as screws, clips, magnets [129]can be added to microfluidic designs to create reversible seals[130, 131] or to orient the device for integration with external systems as is the case with the microfluidic flow cell introduced in **Chapter 3**.

Fluidic Configuration

Microfluidic devices can be designed as "open" or "closed" systems or even a combination of the two[132]. In closed systems, the channel is completely sealed from its externals whereas open systems can be partially or entirely exposed to the atmosphere. Closed systems are preferred where controlled internal pressures are required and are crucial for systems that require sterility where the device is to be stored in a non-sterile environment. Closed configured microfluidics often suffer issues with bubble formation because of the pressure differential between the system and its externals, which can be solved with open fluidic systems. Bubbles occur in open systems, but far less often because of the ability for all gases to equilibrate with atmospheric pressure. Open microfluidics typically use capillary forces[133] to drive flow through a system, but this greatly limits their application to systems that tolerate slow and variable flow rates. In open systems with actuated flow, the greatest challenge is preventing channel overflow where the channel is exposed to atmospheric pressure[134] because surface tension is providing the only confining force. Previous work has designed fine microstructures within channels to increase surface tension in a specific direction to prevent channel overflow[135].

This work encompasses experimentation with both open and closed microfluidic systems to determine the ideal configuration for our application. Furthermore, it is possible to have functional devices designed for each type of configuration as the design complexity increases to permit co-optimization of different desired features.

5.3 Results and Discussion

Overview of Design Iterations

Prototype (1)
3D-printed top
Glass slide bottom
Closed system
↓
Prototype (2)
Prototype 1 +
changes to inlet
orientation
partial open system
↓
Prototype (3)
prototype 2 + 3D printed
mechanical seal
↓
Prototype (4)
prototype 3 + altered inlet
orientation
↓
Prototype (5)
Prototype 4 with inlet
orientation of prototype 3
and added reservoir

removal of 3D printed mechanical seal

Prototype (5)
addition of screw in
electrode
↓
Prototype (6)
Prototype 5 + change in
outlet shape to reservoir
↓
Prototype (7)
change in outlet shape to
reservoir
↓
Prototype (8)
Addition of trumpet to
reservoir
↓
Prototype (9) ☑
prototype 8 +
shortened channel space

removal of reservoir

Prototype (10)
closed outlet
↓
Prototype (11)
change in device
thickness +
change in screw in
fitting dimensions

↓

switch to PDMS-based device

Prototype (12)
2 part device + acrylic
mould
↓
Prototype (12)*
single device + multi-
step moulding
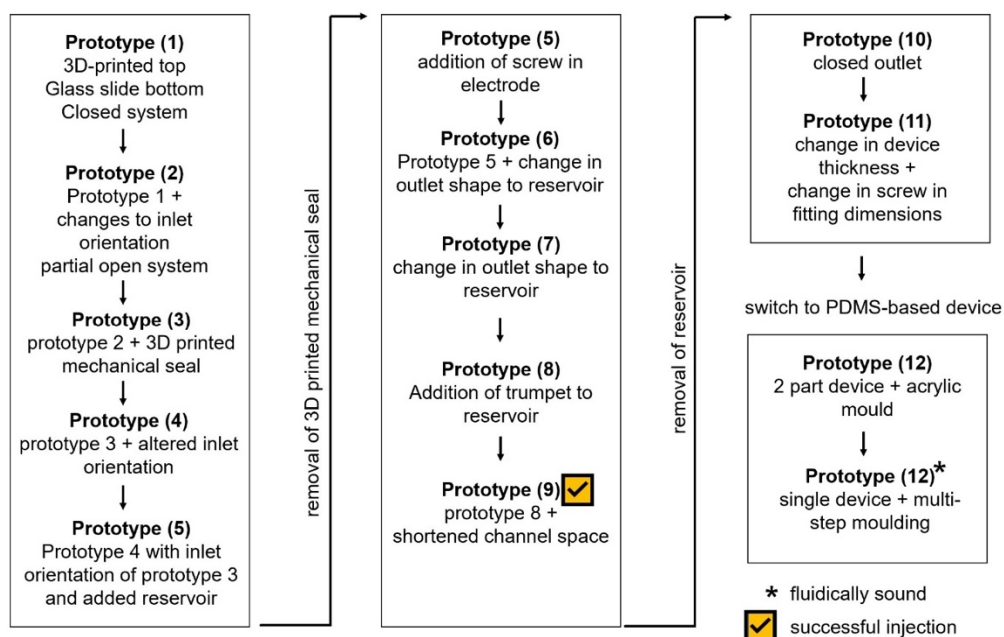
* fluidically sound
☑ successful injection

Figure 29

flow chart of design iterations and main structural changes throughout this work. All prototypes were 3D-printed until prototype 12 where the fabrication protocol was changed to create a PDMS based device.

Iteration Strategy

Figure 29 provides a work through of the iterations of the microfluidic design in this work. The listed "prototypes" represent timepoints where major design changes are made. There are additional intermediate iterations not listed in this flowchart that encompass smaller changes that don't directly affect channel function, such as changes to the thickness of the walls of the screw-in inserts or changes to the amount of material in each print to spare resin. The first method of device fabrication, 3D-printing, was chosen based on its success in the creation of the flow cell in **Chapter 3** and easy access to a printer to permit rapid prototyping. This choice led to the use of larger channel dimensions (500 microns to 2mm) for printer compatibility. Tubing and fitting were chosen based on materials that were already in the lab for the use of the flow injection analysis system. Additionally, the availability

of these tubing materials further influenced the design of channel dimensions in the upper limit of the microfluidic range. Once the facilities returned to pre-covid availability, the design strategy was shifted to a combination of 3D printing and PDMS moulding. Replication of the functionality of the microfluidic flow cell characterized in **Chapter 3** on a platform compatible with planar electrodes was the first design goal of this microfluidic device. This led to parallel development of the microfluidic device with the electrodes developed in **Chapter 4**. As soon as baseline measurement and calibration functionality were established, the integration of cell culture computability would be explored.

Microfluidic Testing Regime

Each device was leak tested at a range of rapid flow rates from 100mL/min to 3000mL/min as the first stipulation for further testing. With larger channel dimensions mandated by 3D-printed and available tubing, these were the range of flow rates necessary for the sample plug to be detected by the electrode within the FSCV acquisition window. If a design passed this initial screening, an electrode was then introduced into the device with buffer solution flowing through the device as illustrated in Figure 37. The resulting oscilloscope signal, discussed in **Chapter 4**, was used to determine the device's compatibility with the electrode for FSCV measurements. Because CFMEs are well characterized in the flow cell, this step of test was primarily performed with CFMEs for direct comparison. Some testing was also performed with CPEs and LINC electrodes to evaluate the effects of changing the electrode geometry. The presence of a "good" oscilloscope signal indicated that the fluid stream through the device made effective contact with the surface of the electrode, which is necessary for FSCV measurements. If the device was capable of reliably introducing the flow stream to the surface of the electrode, the device was then subject to injections of serotonin solutions to further probe the fluid dynamics of the device based on criteria for flow injection profiles developed in **Chapter 3**. Further testing would include calibrations; however, the duration of this project did not permit this step of device characterization. Finally, cells were briefly cultured on a sample of the 3D-printed resin to ensure biocompatibility of the material. The growth of iPSCs is visible in Figure 30 and indicated by red circles that surround the sparse circular stem cells.
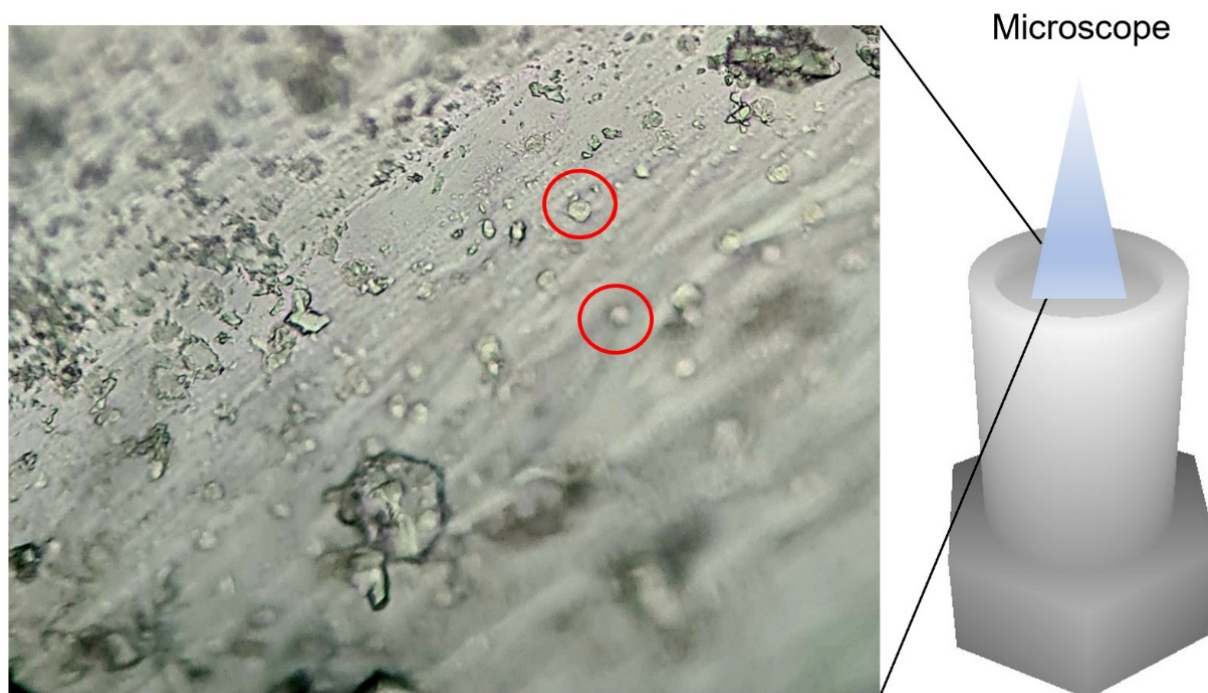
Figure 30

A 200X magnified image of cells imbedded in a 3D printed screw-in insert for a microfluidic device. The image is only resolved in certain sections because the center of the insert is not perfectly flat.

3D-printed designs

The first design concept, depicted in Figure 26, was conceived to include key design features while catering equipment accessibility and the availability of a few samples of metal sputtered glass slides. Prototype 1 includes a 3D printed top with a single channel and T-junction in both the inlets and outlets. It was proposed to use an adhesive coating to bond the 3D printed top with the glass slide containing the electrodes. This metal sputtered slide contained a microelectrode array of 4 working electrodes (one in use at a given time) and two other circuits capable of creating a temperature and pH sensor to monitor the cell culture, which were deemed key design features. A T-junction inlet was proposed to permit on chip mixing of calibration standards to streamline the calibration process and remove the need for the FIA system to prepare samples. The T-junction dual outlet was designed to permit a velocity increase at the designated waste outlet to draw fluid to the waste to function as an additional purging mechanism.
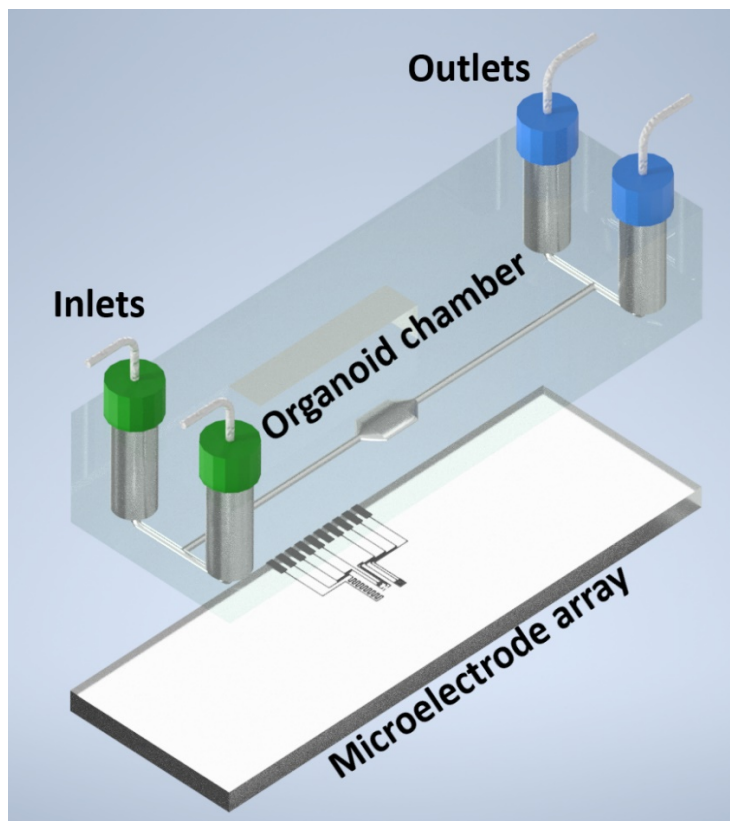
Figure 31

a schematic of prototype 1 described in Figure 26 This prototype failed the leak test and was promptly redesigned.

In this case, the pressures generated at the inlets and outlets at the desired flow rates resulted in serious challenges in finding a compatible adhesive. Primarily, the outlet pressures were high enough to cause backflow and subsequent leaking in the system. This led to the first major design change where an outlet with no fitting (exposed to the atmosphere) was introduced to reduce this pressure while creating a pressure differential to draw fluid through the system. Furthermore, the organoid chamber was removed to reduce dead space in the system to focus on the optimization of on chip calibration, prior to the introduction of cells. Finally, the inlet configuration was changed from a vertical perpendicular to a parallel vertical orientation to harness gravity to accelerate fluid flow through the device, which led to the creation of prototype 2.

To maintain dual functionality of on chip calibration and culturing while also addressing challenges with using an adhesive sealant, a reversible mechanical seal was integrated into the design to create prototype 3. Additionally, it was determined that a planar electrode prototype fabricated on a glass

slide would not be feasible at this stage due to covid related issues with clean room access, so all consecutive designs were adjusted for integration with CFMEs for testing adding complexity to the designs. The seal of this device was comprised of screws with 3D printed "armour", exhibited in Figure 32, to create a uniform pressure across the device to minimize leaking. The positioning and number of screws was varied in many intermediary prototypes of this design to attempt to achieve a water-tight seal but failed due to the rigidity and roughness of the resin. Furthermore, the amount of resin required to print this prototype added unnecessary expense to the project. The channel shape was changed from a diagonal, visible in Figure 32.2, to a rounded slope to minimize pressure variation in the channel that could cause turbulent flow. Finally, the exposed outlet in this design series (prototypes 2-4) led to droplet formation, which was seen to heavily impact the flow injection profile based on the data from **Chapter 3**. A reservoir was added to the design to mitigate droplet formation by taking advantage of the cohesive properties of the buffer and analyte solutions, which are mostly water.
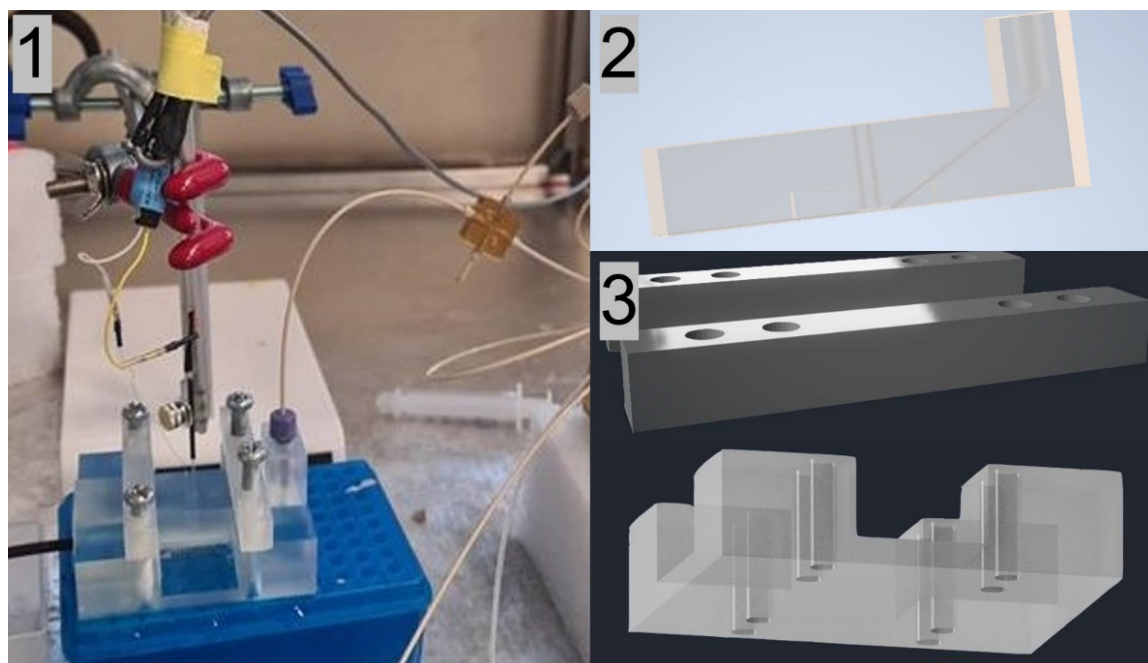

Figure 32

1) assembly and integration of the printed device with a CFME and the FIA system. 2) the portion of the device containing the working and reference electrode tunnels, vertical sample inlet, and open outlet. 3) The 3D printed armour with space for 8 screws to generate a reversible mechanical seal.

The reversible mechanical seal was removed for the next set of designs and therefore a device was printed with a full channel printed into the device to remove the need to seal the channel as depicted in Figure 32.2. This was made possible by the addition of a 3D printed screw-in part customized for integration with CFMEs visible in Figure 33.1 and Figure 33.4. Figure 33.1 illustrates the holes in this insert for the (A) reference electrode and (B) working electrode. This new design also initiated the possibility of a screw-in fitting containing the cultured cells. The (C) inlet to the channel is depicted in Figure 33.2 and (D) indent for the fitting is pictured in Figure 33.3. Previous iterations where electrodes were introduced directly into the channel resulted in leaking out of the electrode tunnels. It was impossible to print holes of the desired diameter with precision because of the inherent variability of the printer, which resulted in a seal that could not withstand the pressures of the system. Initially, the threads for the screws were included in the printed part, but the printer struggled to print threads that were close to specification, so the screws were printed slightly thick to allow creation of the threads with a die post-print. Finally, an (E) trumpet shaped indent, illustrated in Figure 33.3, was added to the space following the outlet to minimize flow perturbation caused by edges observed in the development of the flow cell in **Chapter 3**.
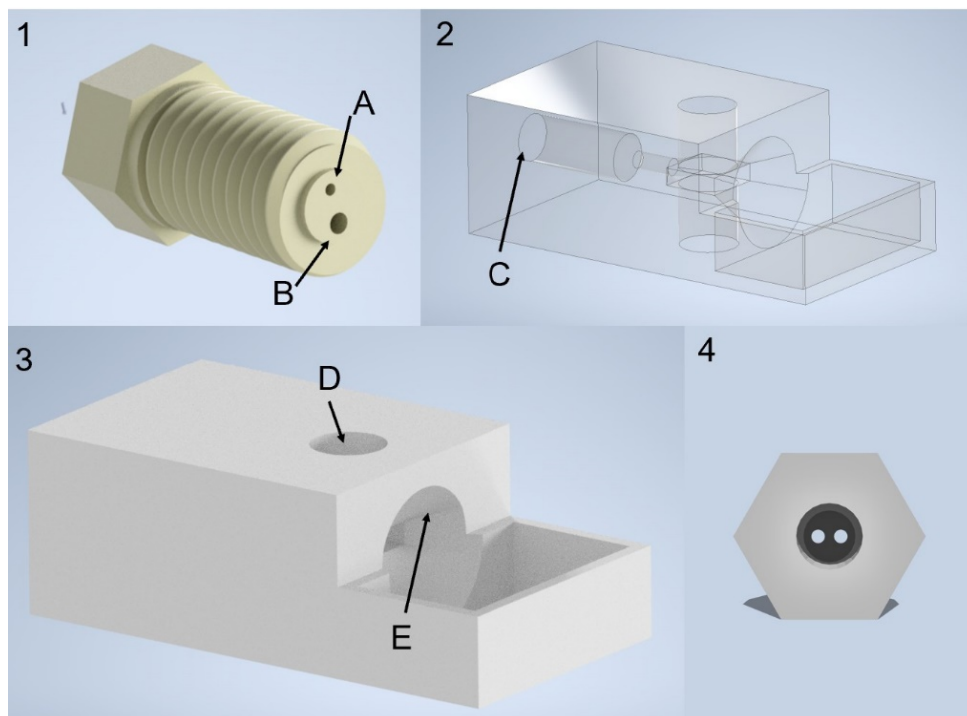
Figure 33

Depicts the (1) screw-in electrode insert with threads, (2) translucent prototype 9 design to highlight the internal channel, (3) prototype 9 with opaque material, and (4) aerial view of electrode insert.

The trumpet shape with screw ins generated successful injections profiles, however this design created negative pressure in the hollow insert that drew fluid into the electrodes, which may not be tolerable for cell measurements. When the inserts were printed solid, the lack of negative pressure at the insert prevented the electrode from reliably making contact with the solution. It was hypothesized that the lower pressure at the outlet was responsible for these challenges leading to its removal from the device's design features.

This design series (prototypes 5-9), visualized in Figure 33 did not leak, but many iterations of the screw-ins were required to achieve functionality. It was necessary that the inserts were hollow from the back as depicted in Figure 33.4 to create the negative pressure in the insert previously mentioned, or the flow stream could not make contact with the electrodes. Additionally, these inserts required a minimum thickness to survive the force placed upon them during both thread machining and insertion into the device. The thickness required for structural integrity of the inserts necessitated a wide

channel to ensure that the insert could be lowered flush with the flow stream. Despite using a clear resin, it was not possible to see the depth of the insert without submerging the device in isopropyl alcohol or acetone. Even submerged in these chemicals, it was difficult to screw in the insert without damaging the CFME.

The next set of prototypes (10-11), shown in Figure 34, returned to a closed fluidic system without the trumpet to permit sterilization for cell culture and to test the backflow hypothesis.
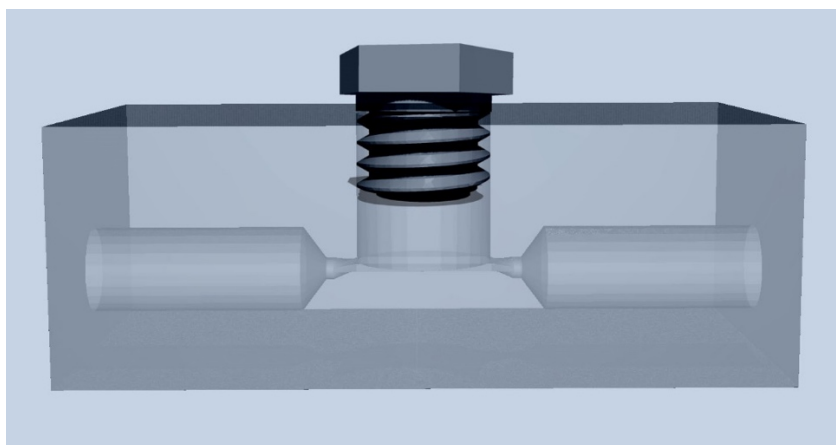

Figure 34

shows prototype 11 with a simple single channel single outlet configuration to test the feasibility of a closed system for this design. The electrode insert screws into the top of the device. The number of threads and the length of the fitting can be varied depending on the geometry and length of the integrated CFME or CPE.

Subpar injections were collected with prototype 11, however it is unclear if the injection profile is a result of the fluid dynamics or the performance of the carbon paste electrodes. Injections in this device with CFME electrodes are necessary to test the backflow hypothesis. Furthermore, the minimum width requirement of the insert adds dead space to the design that likely affected the quality of the injection profiles acquired with this prototype. This design series was discontinued for a protocol switch to PDMS based devices following the development of functional laser induced carbon electrodes that could be fabricated directly onto glass slides.

PDMS based designs

The focus on integration of a planar carbon-based electrode with a microfluidic prompted the switch from 3D printed resin designs to PDMS based designs. Planar electrodes are needed for FSCV measurements from cells to minimize the diffusion of off-target chemicals in the cell media to the electrode that may obscure measurements. The LINC electrode is encapsulated in PDMS, making fabrication with PDMS ideal, because the material adheres well to itself. Furthermore, this protocol allows a more simplistic approach to maximizing proximity between the cells and the electrode than the previous design series that was not possible using CFMEs. The use of PDMS also enables a greater range of compatible hardware such as the use of needles as inlet fittings.

The first PDMS based prototype was fabricated using a basic acrylic mould created by gluing together laser cut acrylic parts. This device could not be plasma bonded to the glass slide with LINC electrode because of the defects on the surface of the PDMS caused by a low-quality mould. The fabrication protocol of the LINC electrode itself creates a surface that is not perfectly flat, which also makes plasma bonding difficult, even when using uncured PDMS as an "adhesive". The challenge with bonding prompted the development of an open fluidic PDMS to permit collection of measurements with the integrated electrodes as proof of principle to develop more complex designs in the future. Final measurements with this device were not possible because the laser induced electrodes could not be exposed aerially with the time remaining in this project due to issues described in **Chapter 4**. The difference in flow regimes for lateral versus aerial exposure of the electroactive area is depicted in Figure 35. The electroactive area of these electrode was perpendicular to the channel as exemplified in Figure 35B, which made it difficult for the flow stream to reach the electrode surface, particularly because of the hydrophobicity of PDMS. A square indentation was forged into the channel with a scalpel to promote the contact between the laterally exposed electrode and the flow stream. This potentially compromised the adhesion between the PDMS channel layer and the electrode layer below. Additionally, the device, illustrated in Figure 36 was plasma treated to increase hydrophilicity to promote the contact of the flow stream with the electrode, which was successful, but the plasma

treatment compromised the integrity of the electrode seal as indicated by a broken oscilloscope signal.

Figure 35

shows electrodes where the electroactive area is exposed (A) parallel or (B) perpendicular to the flow. The electroactive area is indicated by the red line while the flow stream is indicated by the dark blue arrows. The silver tracks connecting the electrode to the FSCV system are indicated by the grey box to the left of the black electrodes.

Figure 36A illustrates prototype 12 where the inlet is forged by a laterally inserted needle, and the outlet is a hole at the bottom of the end of the channel that functions similarly to a drain.
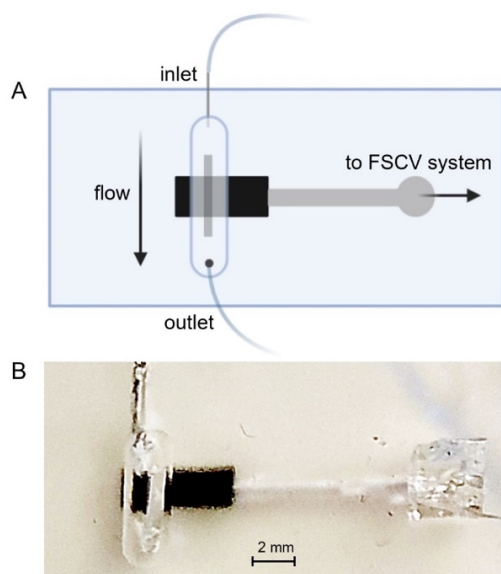

Figure 36

a (A) rendering of prototype 12 indicating the direction of flow, inlets and outlets, and indentation in the channel as represented by a darkened rectangle. A (B) photo of prototype 12 with scalebar.

It is also possible to pipette solutions directly onto the channel and use a syringe pump connected to the outlet to pull fluid out of the device. Future experiments may be performed to determine the ideal pump configuration.

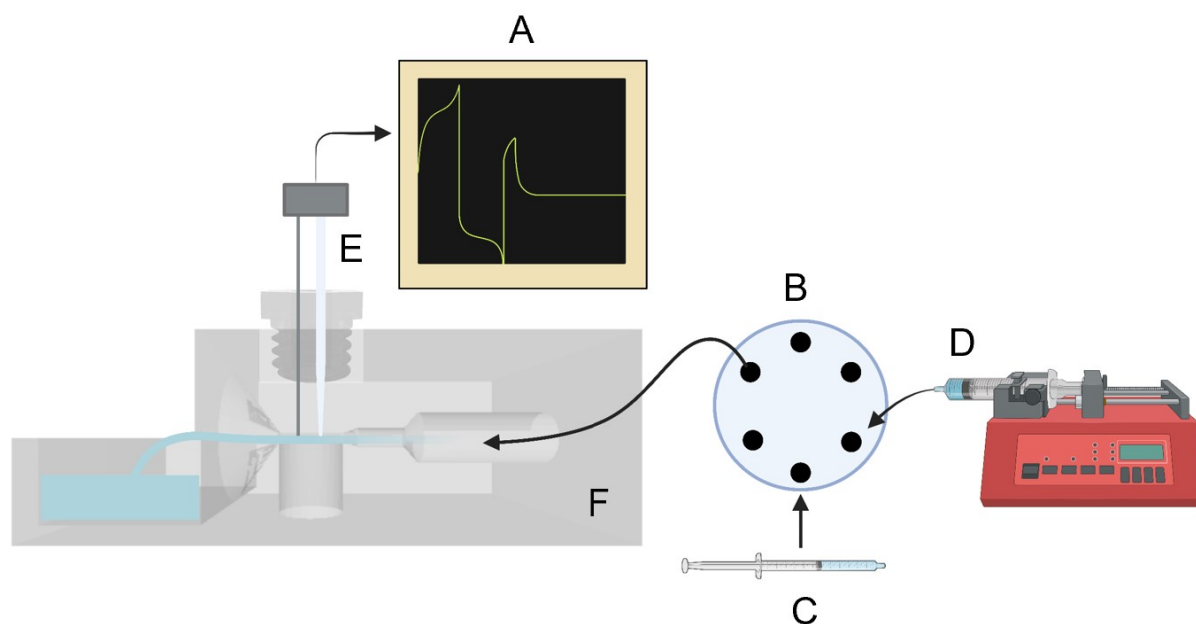## 5.4 Injection Profiles from Microfluidics

Introduction

Figure 37

Experimental set-up using the (A) oscilloscope to test compatibility of the (E) electrode with the (F) microfluidic device where (B) is the 6 port 2-way valve, (C) is the sample syringe, and (D) is the buffer in the syringe pump. Note that the figure is not to scale.

This section reviews serotonin injections performed with prototypes 4, 9, and 11, which passed primary leak testing and exhibited a stable electrode oscilloscope signal. Where the electrode response under controlled conditions is well characterized, examining the injection profiles of a given design elucidates critical information about the transport of the analyte through the device. For example, the microfluidic device itself can contribute noise to the current versus time trace as much as electrode material and geometry. Commonly, this noise is caused by pressure differentials in the flow stream that may occur due to channel roughness, channel geometry, and leaking. Baseline

artifacts that appear at regular intervals indicate phenomena such as droplet formation. All microfluidic devices were connected to the FIA system to perform serotonin injections. The highest quality injections were achieved with prototype 9, however prototype 11 was not tested with a CFME, which may have generated better results. Testing prototype 11 with CFMEs was not performed due to the discontinuation of 3D printed series to pursue promising PDMS based integration with LINC electrodes.

Prototype 4 Injection

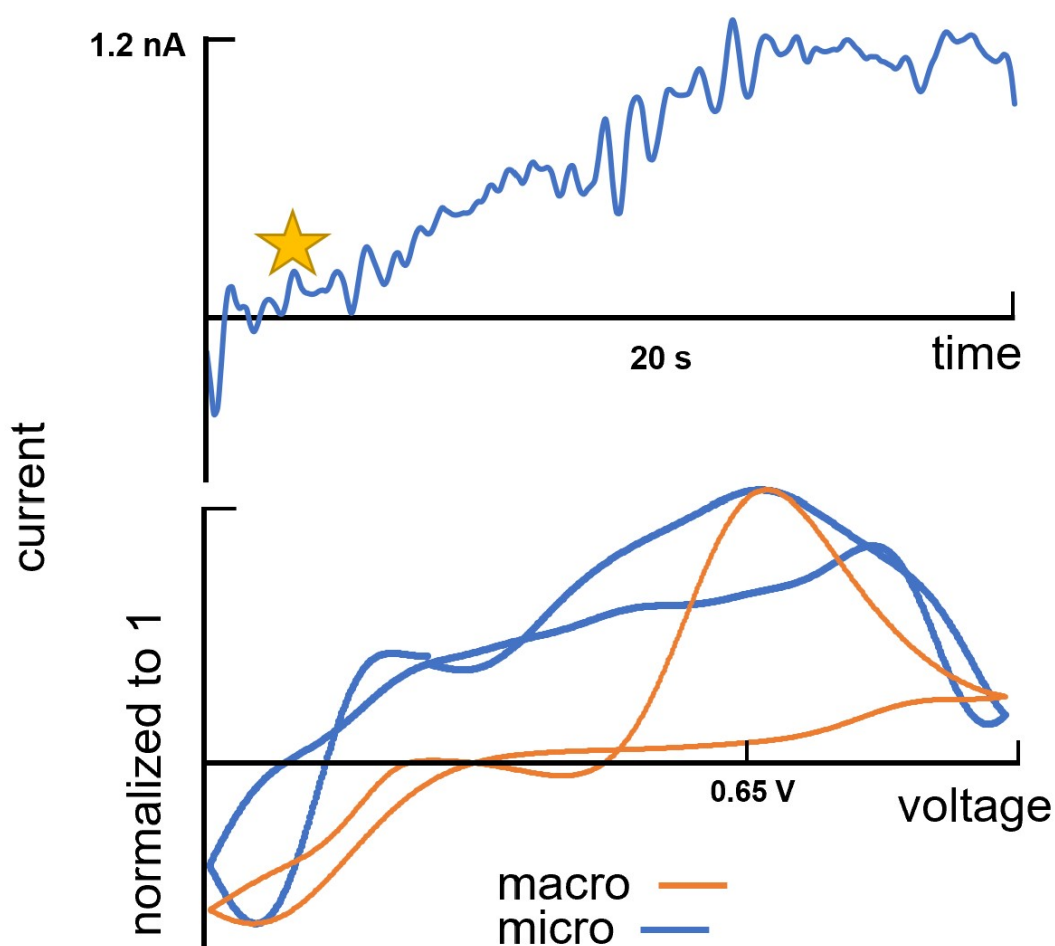The first serotonin injection performed with a CFME in prototype 4 is illustrated in Figure 38.

Figure 38

A current versus time trace (blue) of a 1μM serotonin injection (above) and corresponding CV compared to a 1μM injection in the flow cell (orange) with normalized current (below). The yellow star indicates the time point at which the sample of serotonin is injected into the system.

The injection profile, pictured in the top graph, exhibits a slow rise time, does not return to baseline, and is low magnitude in comparison to an ideal injection profile. The slow rise time indicates dispersion of the sample plug, which in this case is partially due to the distance between the inlet and the working electrode. Additionally, droplet formation was observed at the outlet of this device, which is visible in the current versus time trace. The droplets appear as regular, larger magnitude oscillations that occur at the beginning and at approximately 10 seconds into the signal acquisition. The system was properly grounded, and the electrode exhibited a noise variation of <0.04nA indicating these oscillations are of a fluidic nature. Furthermore, the serotonin oxidative peak exhibited at the bottom of Figure 38 is not shifted in comparison to a serotonin CV acquired in the flow cell, confirming that electrochemical phenomena do not contribute to artifacts in the current versus time trace. The Loctite adhesive used to seal this device did not create a uniform coating, which caused channel roughness and a slow leak that may have contributed to such a low magnitude injection. Serotonin analyte may have also become trapped in the rough surface of the channel minimizing transport to the electrode. This causes a broad signal due to sample dilution where infusion of buffer mixes with remaining analyte following the injection. Incomplete sealing of the electrode and reference electrode chambers can also allow an accumulation of analyte in these areas of the device that may contribute to this effect.

These observations led to design changes that include the reduction of the channel length from the inlet to the electrode, the introduction of a reservoir to eliminate droplet formation, and a fabrication change to exclude the use of an adhesive sealant. A more detailed sequence of changes in visible in Figure 29. These design changes resulted in successful injections with the next design series.

Prototype 9 Injection

Prototype 9, depicted in Figure 37, resulted in injection profiles illustrated in Figure 39.
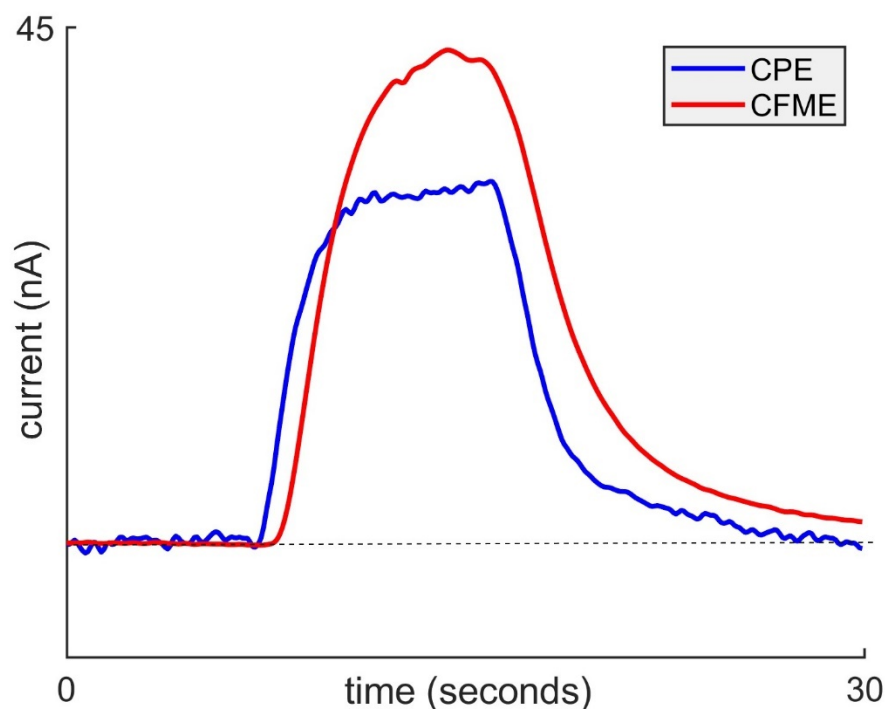

Figure 39

A 1 µM injection of serotonin onto a CPE (blue) or a CFME (red) in prototype 9. The dashed line indicates the baseline current at approximately at 0 nA.

Once a successful serotonin injection was performed in this microfluidic device (as defined by the injection criteria discussed in **Chapter 3**), a CPE was tested in this to ascertain the effect of electrode geometry on the injection profile. Both injections exhibit a rapid rise time and return to baseline, which indicates that the analyte has not become trapped anywhere in the device to induce tailing. The CPE electrode reaches steady state while it appears that the CFME does not, indicating that this issue is an electrochemical phenomenon. Finally, the noisiness of the CPE is clearly visible in comparison to the CFME in Figure 39, but unlike the noise observed in Figure 38, this noise is not a result of any fluidic artifacts.

In previous experiments with the flow cell, it was recorded that variation in CFMEs produces different shaped flow injection profiles, particularly at maximum current, which could explain this observation. This variation among CFMEs can be observed in Figure 40 where all 1µM serotonin injections were performed under the same chemical conditions and flow injection parameters. Even when considering the inherent variation in CFMEs, the CPE current maximum is stable for longer than the CFME.
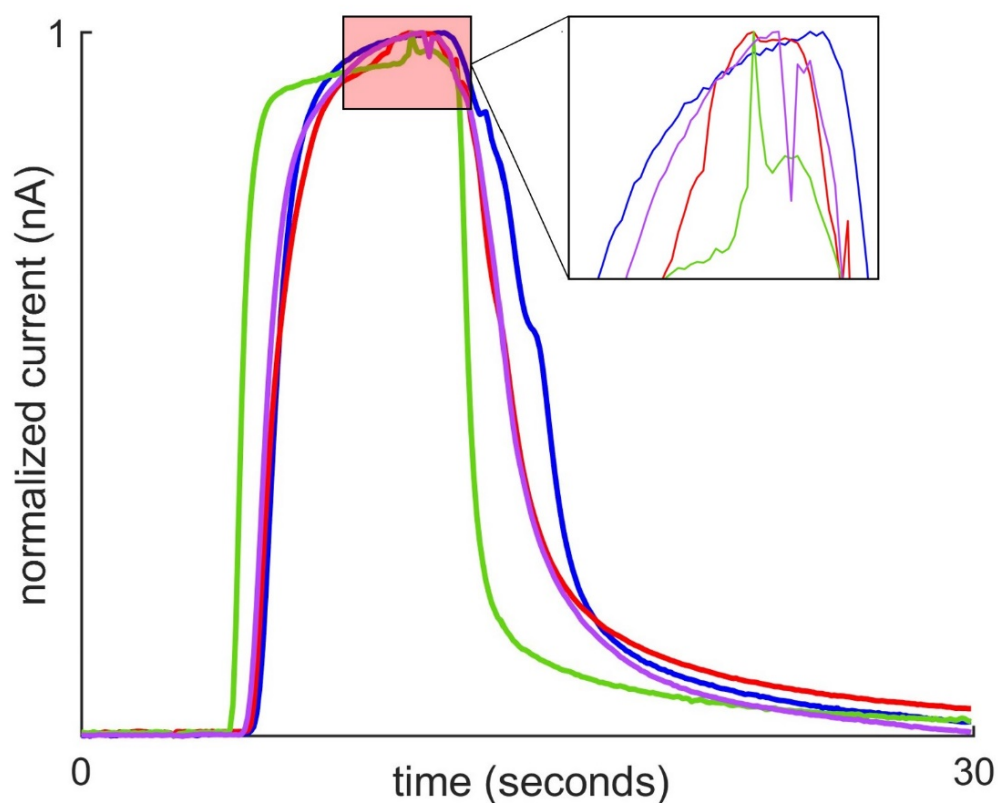
Figure 40

1 µM injections of serotonin onto CFMEs in the flow cell characterized in **Chapter 3** where current is normalized to values between zero and 1 to account for the variation in sensitivity of individual CFMEs. Each colour indicates a difference CFME. A magnified view of the area of maximum current for each electrode is provided to highlight the variation in this region.

This suggests that the CPE reacts with the entirety of the surrounding serotonin before the bolus of sample passes the electrode. This may occur due to the planar geometry of the CPE, which should induce faster reaction equilibrium. An electrode with a single electroactive plane will react faster than

one with multiple electroactive planes where the transport due to advection is coming from one direction. This effect could be exacerbated by the low pressure in the hollow fitting, which draws fluid upward towards the electrode in the direction of the CPE's electroactive plane. Finally, The CPE reaches a lower maximum current, which is expected because of a lower background current indicated by Figure 17 in **Chapter 4**.

Prototype 11 injection

Prototype 11 was tested with serotonin injections at carbon paste electrodes before CFMEs because the final desired integrated electrode geometry is planar. The results of these injections are illustrated in Figure 41 where either a 10µM injection or a 1 µM injection of serotonin at CPE is performed where the CV for the 1 µM injection is shown inset. The 1 µM injection did not yield a discernible injection profile as indicated by the red line in Figure 41, leading to the attempt at a higher concentration of 10 µM.
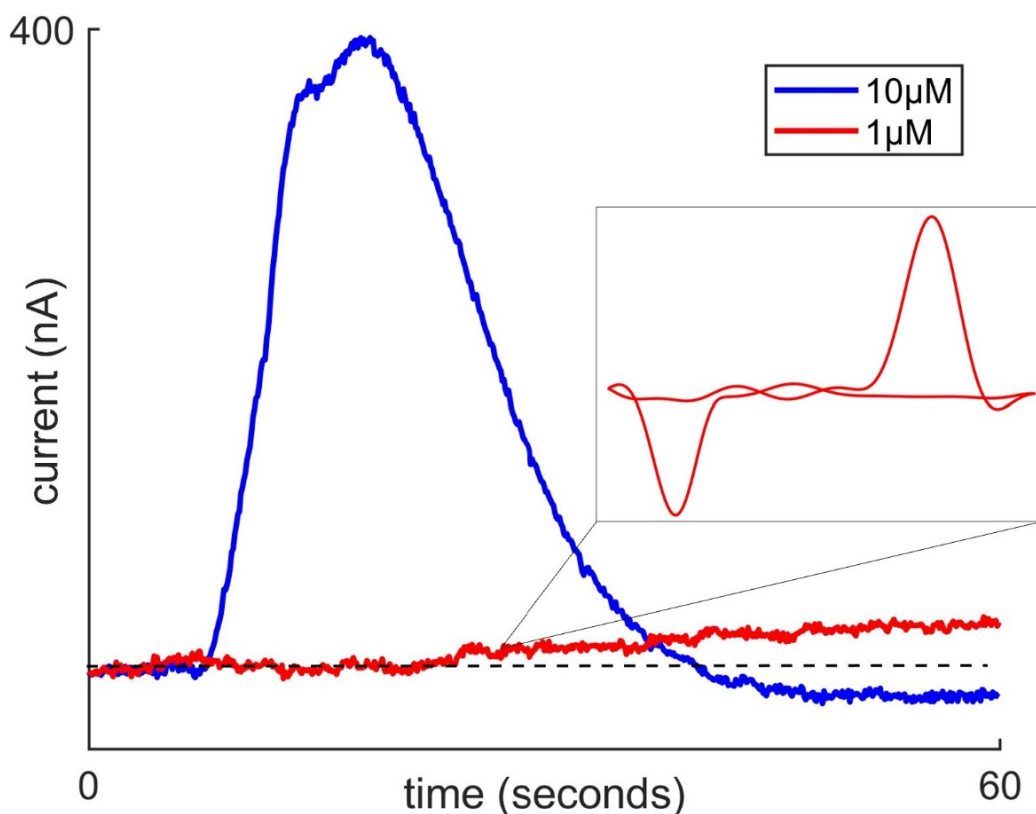
Figure 41

Serotonin injections of either 10 µM (blue) or 1 µM (red) at a CPE in prototype 11 with inset CV derived from the 1 µM injection. The dashed line indicates the baseline current at approximately at 0 nA.

Furthermore, the serotonin oxidative peaks corresponding to these injections are upshifted to 0.74V and occur on the backscan of the CV, which suggests slow adsorption kinetics. It is likely that this is an issue specific to this CPE, not the microfluidic, given that issues with fluid dynamics do not cause this type of shift based on the prototype 4 data. Additionally, CPEs are particularly prone to slow kinetics if the paste is not fully homogenized leading to areas rich in insulating material. Regardless of this experiment, the width of the channel in this device to permit insertion of the 3D-printed part creates excessive dead space that is avoided by the PDMS based design described in this chapter.

5.5 Conclusions

First, this chapter reviews the design considerations and iteration strategy in the development of a microfluidic device with integrated carbon electrodes for direct measurement of neurotransmitters

from cells. Next, we present 1 microfluidic prototype fabricated entirely *via* 3D-printing that can generate high quality flow injection profiles for serotonin FSCV. This device is designed for integration with a CFME or other any other electrode that can be fabricated with a capillary but could be further optimized for other electrode configurations. Additionally, the resin material of this device is determined to be biocompatible, which is critical for application. A second prototype with a fully closed configuration is also introduced with evidence for similar functionality. Finally, we offer a design for a novel PDMS based device fabricated with a combination of 3D-printing and moulding techniques that includes full integration with LINC electrodes. Both the device and the electrodes are simple and inexpensive to manufacture. The PDMS based design enables a controlled decrease in the distance between the electrodes and flow stream, which is crucial for sensing from cells with FSCV.

Chapter 6

6.1 Introduction

The brain is difficult to probe due to its chemical complexity and simultaneous processes, which has led to many mechanisms and pathologies remaining unknown. The monoamine hypothesis of depression implicates a deficiency in norepinephrine, dopamine, and serotonin as the primary cause of depressive symptoms, indicating a need to further study these chemicals. **Chapter 1** began by reviewing the non-genetic and genetic sensing techniques that have been developed to monitor neurotransmitters in the context of depression. In summary, microdialysis, electrophysiological, electrochemical, and optical methods are used to monitor neurotransmitters, with each method having its advantages and limitations. Most optical techniques use cellular machinery to express proteins of interest coupled to an optical reporter that is activated when the target analyte binds to the expressed protein. Other optical probes can be non-genetically to avoid challenges associated with the control of gene expression and off-target effects that impact experimental viability. Next, the electrochemical techniques of interest in this work, Fast-scan cyclic voltammetry (FSCV) and fast scan-controlled adsorption voltammetry (FSCAV), were presented and assessed for the scope of this project.

Briefly, FSCV is an electroanalytical technique used to measure neurotransmission with high temporal resolution and chemical selectivity. FSCV uses microelectrodes, typically made of carbon fiber, to minimize tissue damage and inflammatory responses that could affect experimental results. The technique can only quantify changes in analytes, making it appropriate for measuring the dynamic process of neurotransmission. FSCV has been used to make clinically relevant discoveries in neuroscience, such as the role of dopamine in addiction and the inhibitory effects of histamine on serotonin release. FSCV is complementary to FSCAV, a three-step technique developed to study the diffusion-controlled adsorption of analytes to the electrode and to measure tonic levels of extracellular neurotransmitters. Carbon-based materials, particularly carbon fiber microelectrodes

(CFMEs), are widely used for FSCV due to their excellent chemical properties and suitability for *in vivo* experiments. The unique properties of CFMEs, such as their anisotropic orientation and low noise, make them well-suited for measuring neurotransmission. Overall, FSCV and FSCAV are important tools for studying neurotransmission and have contributed to significant discoveries in neuroscience, making them invaluable in the development of a screening tool for neuropsychiatric illness.

Next, carbon-based electrode materials for electrochemical applications were reviewed to warrant their relevance to this work and reveal potential design considerations. In summary, carbon materials are preferred due to their low cost, biocompatibility, versatility, and potential window. Carbon fiber microelectrodes (CFMEs) are the most used material for *in vivo* experiments due to their excellent chemical properties and suitability for detecting neurochemicals. However, they are not ideal for *in vitro* applications due to their fragile nature and the likelihood of exposing the electrode to more than the targeted secretion. Surface modifications such as overoxidation or polymer coating can be used to improve the sensitivity or selectivity of CFMEs. Carbon composite electrodes and pyrolyzed substrates were also discussed as alternative materials for FSCV electrodes, but they also exhibit some limitations that must be appropriately managed. Finally, the potential of pyrolyzed substrates for the fabrication of FSCV electrodes compatible with microfabrication was reported based on promising previous work.

This chapter continued with the importance of electrode calibration in FSCV, which is performed using flow injection analysis (FIA) to mimic the dynamic changes in analytes that occur *in vivo*. This introduction provided the background and motivation for the flow cell developed in **Chapter 3**. In short, FIA involves introducing a bolus of sample to the electrode at a specified time with an injection switching mechanism, and a steady-state response indicates that the electrode has reached equilibrium and is suitable for collection. However, the variability of in-house made flow cells makes electrode calibration a tedious process, and generalized calibration factors or single-point calibrations are used instead of performing multi-point calibrations for each electrode. The mass transport of the

analyte to the electrode significantly impacts the reliability of electrode calibration, and optimization of fluid dynamics in the design of the flow injection system is required. Microfluidics have been used to address these issues, but standardization of calibration has not yet been achieved indicating a need for a harmonized protocol and consistent instrumentation.

Finally, this chapter specifically discussed the use of FSCV for monitoring dynamic neurotransmission in the brain, which is currently only possible in animal models. To create a translational model of the brain for human studies, somatic cells can be transformed into induced pluripotent stem cells, which can be differentiated into neurons, glia, and progenitor cells to create brain organoids. These organoids can be engineered to recapitulate psychiatric pathologies such as Parkinson's disease and schizophrenia and may serve as a precision/personalized medicine tool for drug screening in patients. However, current models suffer from differences in evoked signal amplitude and response to pharmacological treatment, which can be addressed with microfluidic devices to improve microenvironment control and introduce flow to enhance medium turnover mimicking tissue vascularization.

6.2 summary of chapter 2

The second chapter of this thesis described the general methods and highlights the successful methods used in the experiments in this work. The methods discussed in this chapter include electrochemical methods such as Fast-Scan Cyclic Voltammetry (FSCV), Fast-Scan Controlled-Adsorption Voltammetry (FSCAV), and Flow Injection Analysis (FIA). The specific equipment, reagents, and fabrication protocols used to perform these techniques are also discussed. Computational methods used to simulate the flow injection profile of the flow cell presented in **Chapter 3** were also described.

6.3 summary of chapter 3

This chapter described the design and optimization of a flow cell for flow injection analysis with FSCV. Creating a reliable and producible platform to characterize the response of electrodes with FSCV is

invaluable in elucidating the complex electrochemistry that occurs at these sensors. First, the flow regimes in the design are characterized by the Reynolds and Peclet numbers to inform critical design parameters and identify the primary contributors to issues with flow injection profiles. These primary issues include flow inconsistencies, leaks, and dead volume, which can cause dispersion of the sample plug and distort the injection profile. The flow cell design included features such as a dome-shaped outlet to reduce pulses, a reservoir to prevent overflow, and a tunnel for the reference electrode. These key features enabled square injections with reproducible and stable signals. Next, the reproducibility and robustness of the flow cell design were challenged through FSCV calibrations with serotonin under different conditions. Furthermore, the contribution of the variation between individual electrodes to the total variability in measurements was explored. Then, the stability of the flow cell injections was also evaluated on a scale of hours and days, which revealed key observation in the behaviour of CFMEs for the measurement of serotonin. More specifically, serotonin induced a decay in signal from the electrode with successive exposure. Next, it was determined that this decay in sensitivity was not an issue of the reproducibility of the flow cell based on a comparison with stability experiments using other analytes where the decay did not occur. These experiments indicated that this decay was specific to serotonin, and likely due to its electropolymerization on the electrode surface. Additional work revealed that this decay is reversible *via* overoxidation with the extended Jackson waveform. Finally, experiments were performed to test the compatibility of a flow cell with FSCAV for acquisition of seamless tonic and dynamic measurements. It was not possible to perform static measurements in the flow cell with serotonin, likely due to chemical interactions between this analyte and the material of the flow cell. Performing FSCAV with system flow solved this issue. In summary, these experiments validated the reliability and reproducibility of this fluidic device for performing FSCV with serotonin while uncovering chemical phenomena that occur at the electrode surface. Additionally, the design strategy in the development of this device may be extrapolated to future work with microfluidics for FSCV.

Future work could be pursued to integrate the FIA system directly with the flow cell. This would eliminate the need for an external switching mechanism (*i.e.* 6 port, two-way valve) that may cause signal artifacts in the baseline during injection. Further experiments with chemical coatings on the flow cell could verify the chemical hypothesis for the incompatibility of the flow cell with static FSCAV. Finally, the decay of CFMEs in the presence of serotonin could be further characterized to predict fouling and provide a response factor to provide more accurate quantification where electropolymerization occurs.

6.4 Summary of chapter 4

Chapter 4 discussed the development of an inexpensive and simple fabrication protocol for the manufacture of a novel laser-induced carbon electrode for FSCV of neurotransmitters. The optimization process identified the insulation, back connection, track material/geometry, and electroactive area as critical design considerations. During this optimization, it was observed that a material must be used to isolate the tracks from the pyrolyzed carbon due to its porosity. This process also led to the development of a diagnostic spectrum using the oscilloscope that is integrated into the FSCV data acquisition system. This diagnostic spectrum may be used in the future development of electrodes and electrode modifications with this system. In this chapter, both carbon paste electrodes and laser-induced carbon electrodes were compared with CFMEs using background current, FSCV measurements, and baseline noise. Baseline noise was determined to be a predictor of electrode suitability for FSCV measurements and eliminated carbon paste electrodes as an acceptable microelectrode material. After performing serotonin measurements, we determined that CFMEs have the largest signal to noise ratio, but the LINC electrodes were more sensitive per exposed area and exhibited superior electrochemical kinetics. Surface imaging with SEM revealed that these LINC electrodes could be further optimized to reduce noise and improve the signal to noise ratio. Furthermore, the complex and variable microstructure observed suggested the potential for the use coatings to control surface roughness, which induces variable electroactive areas. Next, a calibration with the LINC electrode was performed, which revealed a higher threshold for quantification and

similar decay behaviour as CFMEs. It was determined that overoxidation to rescue this decay generated a larger increase in sensitivity than that which is observed in CFMEs, but more experiments are required to validate this result.

The next step to improve the performance of the LINC electrode would be to remove the air pocket introduced by the fabrication procedure as illustrated *via* SEM. This alone should reduce the baseline noise of the electrode to generate a better signal to noise ratio. This may be achieved by modifying the grafting step of the fabrication protocol, which is what creates the air pocket. Other options include improving the sensitivity with coatings that dually smooth the surface of the electrode to better control the electroactive area. Future experiments acquiring the background CVs for different electrodes of the same material, where the capacitance may be assumed to be the same, may be performed to provide better estimations of the electroactive area.

6.5 Summary of Chapter 5

Chapter 5 was introduced with a brief review of design consideration for a microfluidic device, which included the desired resolution, complexity, and substrate materials. It was stated that these factors inform the choice of fabrication strategy. In sum, fabrication methods are categorized into 3D printing, etching/lithography-based techniques, machining, and moulding. 3D printing allows rapid prototyping but has low resolution and surface roughness, making it difficult to seal devices. Etching/lithography-based techniques produce high-resolution features but are not as simple or as inexpensive. Machining techniques are not suitable for creating microfeatures but is useful for the manufacture of macroscale features for device integration. Moulding techniques require the creation of a master mould, but the resulting device has high precision and reproducibility.

Next, we proposed the development of a device which replicates the functionality of the flow cell, but with compatibility with planar electrodes and measurement from cell culture. Such a device has never been fabricated for FSCV, which enables dynamic measurements of neurotransmission. Next, we introduced a microfluidic testing regime for the prototypes created in this work to define metrics for

this desired functionality. This testing regime included leak testing at a range of flow rates prior to electrode integration. If successful, the device was subject to injections of serotonin solutions to probe the fluid dynamics of the device. Finally, an experiment was performed on a sample of the 3D-printed resin to ensure biocompatibility of the material because it was not well-characterized in the literature.

After reviewing the testing protocol, this chapter presented the workflow of design iterations that may be used as a guide for future work. To summarize, the first prototype, a closed system two-part device, encountered backflow and leaking occurred that led to changes in the inlet configuration and sealing mechanism. Problems with flow and droplet formation initiated the addition of a reservoir, while continued challenges with sealing prompted the design of a single part device. A few successful injections with later prototypes were achieved before switching to a more suitable fabrication method and design material. With this switch, a promising design with integrated electrodes has been manufactured. This requires further testing before the addition of more complex features such as the proposed second channel for flow-positioning of cells.

6.6 Future Perspectives

The next step was to streamline the integration of the LINC electrode and the PDMS to enable experimentation with measurements from cells. Firstly, the fabrication protocol of the electrodes should be optimized to minimize any air encapsulated in the electrode, which may contribute to the noise observed in signals. The electrodes may be further modified with coatings or nanoparticles to improve their signal to noise ratio and specificity beyond that of a CFME. Next, the electrode fabrication protocol may be altered to expose the lateral plane of the electrode aerially to achieve a configuration where the electrode is flush with the channel of the device. This could be achieved most simply by removing and rotating the PDMS encapsulated carbon. A more elegant approach would include redesigning the protocol entirely where the laser pyrolyzed carbon is deposited onto a stable and conductive carbon substrate. This approach would have the additional advantage of being capable of creating an electrode where all dimensions are in the micron range to minimize the diffusion of off-

target chemicals to the electrode surface during measurements from culture. Formidable adhesion of the pyrolyzed carbon to this substrate and the use of a higher resolution laser could also eliminate the requirement for the encapsulation and re-exposure steps.

After addressing the optimization of the integration of the electrode into the microfluidic, efforts may be shifted to the design of the microfluidic device itself. The addition of a secondary channel for the positioning of the cells was suggested in **Chapter 5**. This may serve as an intermediary to collect preliminary data from cells to inform the development of more complex design features to nourish cells for timeframes longer than the duration of the experiment with the ultimate goal of on-chip culture. This possibility requires surmounting the obstacle of device sterility. The device may be designed as a closed system to enable storage in a non-sterile environment, or as open fluidic where the device is stored in a sterile system. Previous open designs[78] for cerebral organoids cite a lower prevalence of hypoxia as a notable advantage to this approach. Furthermore, the achievement of on-chip culture results in fewer disruptions to the cells, which provide a better recapitulation of their behaviour *in vivo*. Disruptions to cultures encountered with conventional cell culture causes unwanted variation in culture morphology and organization.

Appendix A: Permission to Reprint Chapter 3

Novel Experimental and Analysis Strategies for Fast Voltammetry: 2. A Troubleshoot-Free Flow Cell for FSCV Calibrations

Melissa Hexter, Joseph van Batenburg-Sherwood, and Parastoo Hashemi*

Article Views: 392 | Altmetric: 5 | Citations: -

LEARN ABOUT THESE METRICS

Share   Add to   Export   RIS

About CC Licenses

Creative Commons licenses give everyone from individual creators to large institutions a standardized way to grant the public permission to use their creative work under copyright law. From the reuser's perspective, the presence of a Creative Commons license on a copyrighted work answers the question, *"What can I do with this work?"*

The Creative Commons License Options

There are six different license types, listed from most to least permissive here:

CC BY: This license allows reusers to distribute, remix, adapt, and build upon the material in any medium or format, so long as attribution is given to the creator. The license allows for commercial use.

CC BY includes the following elements:
BY – Credit must be given to the creator

RightsLink

You have been directed to this webpage as a result of the type of license signed between the author and the American Chemical Society that provides users with some different terms of use.

Open Access licenses

If the article is open access and uses a Creative Commons public use license, e.g., CC-BY or CC-BY-NC-ND, rights and permissions questions should be directed to Creative Commons. Contact information can be found on their website at https://creativecommons.org/about/contact

If the article is open access and does not use a Creative Commons license, it is subject to the terms of an ACS public use license. For rights and permissions questions about ACS public use licenses, contact support@services.acs.org with your request, including the following information:

- A link to the ACS article from which you wish to reuse content
- The portion of content you wish to reuse (e.g., number of figures, entire article for thesis)
- A description of where the content will be reused (e.g., name of journal, book title, thesis)

References

1. organization, w.h. *Depressive disorder (depression)*. 2023; Available from: 1.
    https://www.who.int/news-room/fact-sheets/detail/depression

2. Penn, E. and D.K. Tracy, *The drugs don't work? antidepressants and the current and future pharmacological management of depression.* Ther Adv Psychopharmacol, 2012. **2**(5): p. 179-88.

3. Schildkraut, J.J., *The catecholamine hypothesis of affective disorders: a review of supporting evidence.* Am J Psychiatry, 1965. **122**(5): p. 509-22.

4. Rocher, C., et al., *Microdialysis monitoring of variations in extracellular levels of serotonin, GABA and excitatory amino acids in the frontal cortex of awake rats in response to a single peripheral or central administration of dexfenfluramine.* Brain Res, 1996. **737**(1-2): p. 221-30.

5. Yang, H., et al., *Physiologically relevant changes in serotonin resolved by fast microdialysis.* ACS Chem Neurosci, 2013. **4**(5): p. 790-8.

6. Lee, W.H., et al., *Microfabrication and in Vivo Performance of a Microdialysis Probe with Embedded Membrane.* Anal Chem, 2016. **88**(2): p. 1230-7.

7. Morton, R.A., Y. Yanagawa, and C.F. Valenzuela, *Electrophysiological Assessment of Serotonin and GABA Neuron Function in the Dorsal Raphe during the Third Trimester Equivalent Developmental Period in Mice.* eNeuro, 2015. **2**(6).

8. Guiard, B.P., et al., *Functional interactions between dopamine, serotonin and norepinephrine neurons: an in-vivo electrophysiological study in rats with monoaminergic lesions.* International Journal of Neuropsychopharmacology, 2008. **11**(5): p. 625-639.

9. Shepard, P.D. and D.C. German, *Electrophysiological and pharmacological evidence for the existence of distinct subpopulations of nigrostriatal dopaminergic neuron in the rat.* Neuroscience, 1988. **27**(2): p. 537-46.

10. Gubernator, N.G., et al., *Fluorescent false neurotransmitters visualize dopamine release from individual presynaptic terminals.* Science, 2009. **324**(5933): p. 1441-4.

11. Erritzoe, D., et al., *Serotonin release measured in the human brain: a PET study with [(11)C]CIMBI-36 and d-amphetamine challenge.* Neuropsychopharmacology, 2020. **45**(5): p. 804-810.

12. Hai, A., et al., *Molecular fMRI of Serotonin Transport.* Neuron, 2016. **92**(4): p. 754-765.

13. Jackman, S.L., et al., *Achieving high-frequency optical control of synaptic transmission.* J Neurosci, 2014. **34**(22): p. 7704-14.

14. Lee, C., et al., *Light Up the Brain: The Application of Optogenetics in Cell-Type Specific Dissection of Mouse Brain Circuits.* Front Neural Circuits, 2020. **14**: p. 18.

15. Beyene, A.G., et al., *Imaging striatal dopamine release using a nongenetically encoded near infrared fluorescent catecholamine nanosensor.* Sci Adv, 2019. **5**(7): p. eaaw3108.

16. Wu, Z., D. Lin, and Y. Li, *Pushing the frontiers: tools for monitoring neurotransmitters and neuromodulators.* Nat Rev Neurosci, 2022. **23**(5): p. 257-274.

17. Nguyen, Q.T., et al., *An in vivo biosensor for neurotransmitter release and in situ receptor activity.* Nat Neurosci, 2010. **13**(1): p. 127-132.

18. Kubitschke, M., et al., *Next generation genetically encoded fluorescent sensors for serotonin.* Nat Commun, 2022. **13**(1): p. 7525.

19. Marvin, J.S., et al., *A genetically encoded fluorescent sensor for in vivo imaging of GABA.* Nat Methods, 2019. **16**(8): p. 763-770.

20. Babl, S.S., B.P. Rummell, and T. Sigurdsson, *The Spatial Extent of Optogenetic Silencing in Transgenic Mice Expressing Channelrhodopsin in Inhibitory Interneurons.* Cell Reports, 2019. **29**(5): p. 1381-1395.e4.

21. Leopold, A.V., D.M. Shcherbakova, and V.V. Verkhusha, *Fluorescent Biosensors for Neurotransmission and Neuromodulation: Engineering and Applications.* Frontiers in Cellular Neuroscience, 2019. **13**.

22. Clark, L.C., Jr. and C. Lyons, *Studies of a glassy carbon electrode for brain polarography with observations on the effect of carbonic anhydrase inhibition.* Ala J Med Sci, 1965. **2**(4): p. 353-9.

23. Adams, R.N., *Probing brain chemistry with electroanalytical techniques.* Anal Chem, 1976. **48**(14): p. 1126A-1138A.

24. Kissinger, P.T., J.B. Hart, and R.N. Adams, *Voltammetry in brain tissue — a new neurophysiological measurement.* Brain Research, 1973. **55**(1): p. 209-213.

25. Millar, J., et al., *Electrochemical, pharmacological and electrophysiological evidence of rapid dopamine release and removal in the rat caudate nucleus following electrical stimulation of the median forebrain bundle.* Eur J Pharmacol, 1985. **109**(3): p. 341-8.

26. Hashemi, P., et al., *In vivo electrochemical evidence for simultaneous 5-HT and histamine release in the rat substantia nigra pars reticulata following medial forebrain bundle stimulation.* Journal of Neurochemistry, 2011. **118**(5): p. 749-759.

27. Giros, B., et al., *Hyperlocomotion and indifference to cocaine and amphetamine in mice lacking the dopamine transporter.* Nature, 1996. **379**(6566): p. 606-12.

28. Hashemi, P., et al., *Brain dopamine and serotonin differ in regulation and its consequences.* Proc Natl Acad Sci U S A, 2012. **109**(29): p. 11510-5.

29. Robinson, D.L., et al., *Detecting subsecond dopamine release with fast-scan cyclic voltammetry in vivo.* Clin Chem, 2003. **49**(10): p. 1763-73.

30. Jackson, B.P., S.M. Dietz, and R.M. Wightman, *Fast-scan cyclic voltammetry of 5-hydroxytryptamine.* Anal Chem, 1995. **67**(6): p. 1115-20.

31. Wonnenberg, P., et al., *Polymer Modified Carbon Fiber Microelectrodes for Precision Neurotransmitter Metabolite Measurements.* J Electrochem Soc, 2020. **167**(16).

32. Strand, A.M. and B.J. Venton, *Flame etching enhances the sensitivity of carbon-fiber microelectrodes.* Anal Chem, 2008. **80**(10): p. 3708-15.

33. Rodeberg, N.T., et al., *Hitchhiker's Guide to Voltammetry: Acute and Chronic Electrodes for in Vivo Fast-Scan Cyclic Voltammetry.* ACS Chem Neurosci, 2017. **8**(2): p. 221-234.

34. Phillips, P.E., et al., *Subsecond dopamine release promotes cocaine seeking.* Nature, 2003. **422**(6932): p. 614-8.

35. Hersey, M., et al., *Inflammation-Induced Histamine Impairs the Capacity of Escitalopram to Increase Hippocampal Extracellular Serotonin.* J Neurosci, 2021. **41**(30): p. 6564-6577.

36. Lu, Y., et al., *Modulating dopamine release by optogenetics in transgenic mice reveals terminal dopaminergic dynamics.* Neurophotonics, 2015. **2**(3): p. 031207.

37. Walton, L.R., et al., *Simultaneous fMRI and fast-scan cyclic voltammetry bridges evoked oxygen and neurotransmitter dynamics across spatiotemporal scales.* Neuroimage, 2021. **244**: p. 118634.

38. Wan, J., et al., *A genetically encoded sensor for measuring serotonin dynamics.* Nat Neurosci, 2021. **24**(5): p. 746-752.

39. Atcherley, C.W., et al., *Fast-scan controlled-adsorption voltammetry for the quantification of absolute concentrations and adsorption dynamics.* Langmuir, 2013. **29**(48): p. 14885-92.

40. Witt, C., *Optimization and Application of Electrochemical Probes for Neurotransmitter Detection*. 2021.

41. Gee, T.A., et al., *A pain-induced tonic hypodopaminergic state augments phasic dopamine release in the nucleus accumbens.* Pain, 2020. **161**(10): p. 2376-2384.

42. Michalkiewicz, S., A. Skorupa, and M. Jakubczyk, *Carbon Materials in Electroanalysis of Preservatives: A Review.* Materials (Basel), 2021. **14**(24).

43. Strein, T.G. and A.G. Ewing, *In situ laser activation of carbon fiber microdisk electrodes.* Analytical Chemistry, 1991. **63**(3): p. 194-198.

44. Zestos, A.G., *Carbon Nanoelectrodes for the Electrochemical Detection of Neurotransmitters.* Int J Electrochem, 2018. **2018**.

45. Puthongkham, P. and B.J. Venton, *Recent advances in fast-scan cyclic voltammetry.* Analyst, 2020. **145**(4): p. 1087-1102.

46. Purcell, E.K., et al., *Next-Generation Diamond Electrodes for Neurochemical Sensing: Challenges and Opportunities.* Micromachines (Basel), 2021. **12**(2).

47. Huffman, M.L. and B.J. Venton, *Carbon-fiber microelectrodes for in vivo applications.* Analyst, 2009. **134**(1): p. 18-24.

48. Hexter, M., J. van Batenburg-Sherwood, and P. Hashemi, *Novel Experimental and Analysis Strategies for Fast Voltammetry: 2. A Troubleshoot-Free Flow Cell for FSCV Calibrations.* ACS Measurement Science Au, 2023.

49. Kissinger, P.T. and W.R. Heineman, *Laboratory techniques in electroanalytical chemistry*. Monographs in electroanalytical chemistry and electrochemistry. 1984, New York: Dekker. 1 online resource.

50. Long, J.T. and S.G. Weber, *Noise at microelectrodes and microelectrode arrays in amperometry and voltammetry.* Analytical Chemistry, 1988. **60**(20): p. 2309-2311.

51. Heien, M.L., et al., *Overoxidation of carbon-fiber microelectrodes enhances dopamine adsorption and increases sensitivity.* Analyst, 2003. **128**(12): p. 1413-9.

52. Takmakov, P., et al., *Carbon microelectrodes with a renewable surface.* Anal Chem, 2010. **82**(5): p. 2020-8.

53. Hashemi, P., et al., *Voltammetric detection of 5-hydroxytryptamine release in the rat brain.* Anal Chem, 2009. **81**(22): p. 9462-71.

54. Swamy, B.E.K. and B.J. Venton, *Carbon nanotube-modified microelectrodes for simultaneous detection of dopamine and serotoninin vivo.* Analyst, 2007. **132**(9): p. 876-884.

55. Oni, J., P. Westbroek, and T. Nyokong, *Construction and characterization of carbon paste ultra-microelectrodes.* Electrochemistry Communications, 2001. **3**(9): p. 524-528.

56. McCreery, R.L., *Advanced Carbon Electrode Materials for Molecular Electrochemistry.* Chemical Reviews, 2008. **108**(7): p. 2646-2687.

57. Bolger, F.B., et al., *Characterisation of carbon paste electrodes for real-time amperometric monitoring of brain tissue oxygen.* J Neurosci Methods, 2011. **195**(2): p. 135-42.

58. Clark, K.M. and C.S. Henry, *Thermoplastic Electrode (TPE)-based Enzymatic Glucose Sensor Using Polycaprolactone-graphite Composites.* Electroanalysis, 2022. **34**(12): p. 1869-1876.

59. Oliveira, A., et al., *Laser-Induced Carbon Pyrolysis of Electrodes for Neural Interface Systems.* Eur J Transl Myol, 2016. **26**(3): p. 6062.

60. Nam, K.H., et al., *Laser direct write of heteroatom-doped graphene on molecularly controlled polyimides for electrochemical biosensors with nanomolar sensitivity.* Carbon N Y, 2022. **188**: p. 209-219.

61. Vomero, M., et al., *Graphitic Carbon Electrodes on Flexible Substrate for Neural Applications Entirely Fabricated Using Infrared Nanosecond Laser Technology.* Sci Rep, 2018. **8**(1): p. 14749.

62. Li, J., et al., *A tissue-like neurotransmitter sensor for the brain and gut.* Nature, 2022. **606**(7912): p. 94-101.

63. Miller, D.R., E.S. McClain, and D.E. Cliffel, *Electrochemical Microphysiometry Detects Cellular Glutamate Uptake.* Journal of The Electrochemical Society, 2018. **165**.

64. Delong, L.M., et al., *A microfluidic electrochemical flow cell capable of rapid on-chip dilution for fast-scan cyclic voltammetry electrode calibration.* Anal Bioanal Chem, 2020. **412**(24): p. 6287-6294.

65. Rodeberg, N.T., *IMPROVING THE COLLECTION AND CALIBRATION OF VOLTAMMETRIC MEASUREMENTS OF*

STRIATAL DOPAMINE RELEASE. 2017.

66. John, C.E., et al., *Neurochemical characterization of the release and uptake of dopamine in ventral tegmental area and serotonin in substantia nigra of the mouse.* J Neurochem, 2006. **96**(1): p. 267-82.

67. Holmes, J., et al., *Glutamate Electropolymerization on Carbon Increases Analytical Sensitivity to Dopamine and Serotonin: An Auspicious In Vivo Phenomenon in Mice?* Anal Chem, 2021. **93**(31): p. 10762-10771.

68. Kristensen, E.W., R.L. Wilson, and R.M. Wightman, *Dispersion in flow injection analysis measured with microvoltammetric electrodes.* Analytical Chemistry, 1986. **58**(4): p. 986-988.

69. Abdalla, A., et al., *In Vivo Ambient Serotonin Measurements at Carbon-Fiber Microelectrodes.* Analytical Chemistry, 2017. **89**(18): p. 9703-9711.

70. Sinkala, E., et al., *Electrode calibration with a microfluidic flow cell for fast-scan cyclic voltammetry.* Lab Chip, 2012. **12**(13): p. 2403-8.

71. Pereira, S.V., et al., *A microfluidic device based on a screen-printed carbon electrode with electrodeposited gold nanoparticles for the detection of IgG anti-Trypanosoma cruziantibodies.* Analyst, 2011. **136**(22): p. 4745-4751.

72. Seo, K.-D., et al., *Microfluidic neurotransmitters sensor in blood plasma with mediator-immobilized conducting polymer/N, S-doped porous carbon composite.* Sensors and Actuators B: Chemical, 2020. **313**: p. 128017.

73. Sansuk, S., et al., *Ultrasensitive Detection of Dopamine Using a Carbon Nanotube Network Microfluidic Flow Electrode.* Analytical Chemistry, 2013. **85**(1): p. 163-169.

74. Felici, E., et al. *Microfluidic Platform Integrated with Carbon Nanofibers-Decorated Gold Nanoporous Sensing Device for Serum PSA Quantification*. Biosensors, 2023. **13**, DOI: 10.3390/bios13030390.

75. Whulanza, Y., et al., *On-chip testing of a carbon-based platform for electro-adsorption of glutamate.* Heliyon, 2022. **8**(5): p. e09445.

76. Hiramoto, K., et al., *Electric and Electrochemical Microfluidic Devices for Cell Analysis.* Frontiers in Chemistry, 2019. **7**.

77. Takahashi, K. and S. Yamanaka, *Induction of pluripotent stem cells from mouse embryonic and adult fibroblast cultures by defined factors.* Cell, 2006. **126**(4): p. 663-76.

78. Ao, Z., et al., *One-Stop Microfluidic Assembly of Human Brain Organoids To Model Prenatal Cannabis Exposure.* Anal Chem, 2020. **92**(6): p. 4630-4638.

79. Cho, A.N., et al., *Microfluidic device with brain extracellular matrix promotes structural and functional maturation of human brain organoids.* Nat Commun, 2021. **12**(1): p. 4730.

80. Luo, C., et al., *Cerebral Organoids Recapitulate Epigenomic Signatures of the Human Fetal Brain.* Cell Rep, 2016. **17**(12): p. 3369-3384.

81. Smits, L.M. and J.C. Schwamborn, *Midbrain Organoids: A New Tool to Investigate Parkinson's Disease.* Front Cell Dev Biol, 2020. **8**: p. 359.

82. Holmes, J., et al., *Voltammetric Approach for Characterizing the Biophysical and Chemical Functionality of Human Induced Pluripotent Stem Cell-Derived Serotonin Neurons.* Anal Chem, 2022. **94**(25): p. 8847-8856.

83. Zhang, S., Z. Wan, and R.D. Kamm, *Vascularized organoids on a chip: strategies for engineering organoids with functional vasculature.* Lab Chip, 2021. **21**(3): p. 473-488.

84. Dunham, K.E. and B.J. Venton, *Improving serotonin fast-scan cyclic voltammetry detection: new waveforms to reduce electrode fouling.* Analyst, 2020. **145**(22): p. 7437-7446.

85. Gerhardt, G. and R.N. Adams, *Determination of diffusion coefficients by flow injection analysis.* Analytical Chemistry, 1982. **54**(14): p. 2618-2620.

86. O'Connell, L., *Determination of diffusion coefficients by flow injection analysis*. 2017, University of Lyon.

87. Samaranayake, S., et al., *In vivo histamine voltammetry in the mouse premammillary nucleus.* Analyst, 2015. **140**(11): p. 3759-65.

88. Taylor, I.M., et al., *Enhanced dopamine detection sensitivity by PEDOT/graphene oxide coating on in vivo carbon fiber electrodes.* Biosens Bioelectron, 2017. **89**(Pt 1): p. 400-410.

89. Dankoski, E.C. and R.M. Wightman, *Monitoring serotonin signaling on a subsecond time scale.* Front Integr Neurosci, 2013. **7**: p. 44.

90. Hensley, A.L., A.R. Colley, and A.E. Ross, *Real-Time Detection of Melatonin Using Fast-Scan Cyclic Voltammetry.* Anal Chem, 2018. **90**(14): p. 8642-8650.

91. Swamy, B.E. and B.J. Venton, *Subsecond detection of physiological adenosine concentrations using fast-scan cyclic voltammetry.* Anal Chem, 2007. **79**(2): p. 744-50.

92. Yang, Y., et al., *Real-time subsecond voltammetric analysis of Pb in aqueous environmental samples.* Anal Chem, 2013. **85**(15): p. 7535-41.

93. Venton, B.J. and Q. Cao, *Fundamentals of fast-scan cyclic voltammetry for dopamine detection.* Analyst, 2020. **145**(4): p. 1158-1168.

94. Kuzum, D., et al., *Transparent and flexible low noise graphene electrodes for simultaneous electrophysiology and neuroimaging.* Nat Commun, 2014. **5**: p. 5259.

95. Farahi, A., et al., *Silver particles-modified carbon paste electrodes for differential pulse voltammetric determination of paraquat in ambient water samples.* Journal of the Association of Arab Universities for Basic and Applied Sciences, 2016. **19**: p. 37-43.

96. Yi, W., et al., *3D carbon nanofiber microelectrode arrays fabricated by plasma-assisted pyrolysis to enhance sensitivity and stability of real-time dopamine detection.* Biomedical Microdevices, 2016. **18**.

97. Ding, B., et al., *Laser-Induced Carbon Electrodes in a Three-Dimensionally Printed Flow Reactor for Detecting Lead Ions.* ACS Omega, 2021. **6**(19): p. 12470-12479.

98. Mamleyev, E.R., et al., *Laser-induced hierarchical carbon patterns on polyimide substrates for flexible urea sensors.* npj Flexible Electronics, 2019. **3**(1): p. 2.

99. López-Honorato, E., et al., *Characterization of the anisotropy of pyrolytic carbon by Raman spectroscopy.* Carbon, 2010. **48**(3): p. 881-890.

100. Lu, L., et al., *The Electrochemical Behavior of Carbon Fiber Microelectrodes Modified with Carbon Nanotubes Using a Two-Step Electroless Plating/Chemical Vapor Deposition Process.* Sensors (Basel), 2017. **17**(4).

101. Manciu, F.S., et al., *Analysis of Carbon-Based Microelectrodes for Neurochemical Sensing.* Materials (Basel), 2019. **12**(19).

102. Xie, X. and R. Holze *Electrode Kinetic Data: Geometric vs. Real Surface Area*. Batteries, 2022. **8**, DOI: 10.3390/batteries8100146.

103. Cao, Q., P. Puthongkham, and B.J. Venton, *Review: new insights into optimizing chemical and 3D surface structures of carbon electrodes for neurotransmitter detection.* Analytical Methods, 2019. **11**(3): p. 247-261.

104. Abdulhafez, M., G.N. Tomaraei, and M. Bedewy, *Fluence-Dependent Morphological Transitions in Laser-Induced Graphene Electrodes on Polyimide Substrates for Flexible Devices.* ACS Applied Nano Materials, 2021. **4**(3): p. 2973-2986.

105. Zhao, L., et al., *Nitrogen-Containing Hydrothermal Carbons with Superior Performance in Supercapacitors.* Advanced Materials, 2010. **22**(45): p. 5202-5206.

106. Thompson, M.T., *Chapter 16 - Noise*, in *Intuitive Analog Circuit Design (Second Edition)*, M.T. Thompson, Editor. 2014, Newnes: Boston. p. 617-643.

107. Zhao, H., *Carbon nanospikes have improved sensitivity and anti-fouling properties for adenosine, histamine, and hydrogen peroxide*, in *Pittcon*. 2023: Philadelphia, PA.

108. Velický, M., et al., *Electrochemistry of the Basal Plane versus Edge Plane of Graphite Revisited.* The Journal of Physical Chemistry C, 2019. **123**(18): p. 11677-11685.

109. Chiaradia, I. and M.A. Lancaster, *Brain organoids for the study of human neurobiology at the interface of in vitro and in vivo.* Nature Neuroscience, 2020. **23**(12): p. 1496-1508.

110. Agboola, O.S., et al., *Brain organoid: a 3D technology for investigating cellular composition and interactions in human neurological development and disease models in vitro.* Stem Cell Research & Therapy, 2021. **12**(1): p. 430.

111. Melow, S.L., et al., *A low-interference, high-resolution multianalyte electrochemical biosensor.* Anal Methods, 2020. **12**(31): p. 3873-3882.

112.   Kuo, J.S. and D.T. Chiu, *Controlling mass transport in microfluidic devices.* Annu Rev Anal Chem (Palo Alto Calif), 2011. **4**: p. 275-96.

113.   Gilbert, D.F., et al., *Proliferation characteristics of cells cultured under periodic versus static conditions.* Cytotechnology, 2019. **71**(1): p. 443-452.

114.   Wikswo, J.P., et al., *Engineering challenges for instrumenting and controlling integrated organ-on-chip systems.* IEEE Trans Biomed Eng, 2013. **60**(3): p. 682-90.

115.   Sahin, O., M. Ashokkumar, and P.M. Ajayan, *3 - Micro- and nanopatterning of biomaterial surfaces*, in *Fundamental Biomaterials: Metals*, P. Balakrishnan, S. M S, and S. Thomas, Editors. 2018, Woodhead Publishing. p. 67-78.

116.   Wang, C.K., et al., *One-Step Approach to Fabricating Polydimethylsiloxane Microfluidic Channels of Different Geometric Sections by Sequential Wet Etching Processes.* J Vis Exp, 2018(139).

117.   Willems, S.B.J., et al., *COvalent monolayer patterns in Microfluidics by PLasma etching Open Technology – COMPLOT.* Analyst, 2020. **145**(5): p. 1629-1635.

118.   Wlodarczyk, K.L., D.P. Hand, and M.M. Maroto-Valer, *Maskless, rapid manufacturing of glass microfluidic devices using a picosecond pulsed laser.* Sci Rep, 2019. **9**(1): p. 20215.

119.   Deng, Y.L. and Y.J. Juang, *Polydimethyl siloxane wet etching for three dimensional fabrication of microneedle array and high-aspect-ratio micropillars.* Biomicrofluidics, 2014. **8**(2): p. 026502.

120.   Takayama, S., et al., *Topographical Micropatterning of Poly(dimethylsiloxane) Using Laminar Flows of Liquids in Capillaries.* Advanced Materials, 2001. **13**(8): p. 570-574.

121.   Xu, L.C. and C.A. Siedlecki, *4.18 Surface Texturing and Control of Bacterial Adhesion*, in *Comprehensive Biomaterials II*, P. Ducheyne, Editor. 2017, Elsevier: Oxford. p. 303-320.

122.   Baumberger, B., *Establishing a Biomarker-based Human Model of Depression that leverages the Brain-Skin Connection*, in *Pittcon*. 2023: Philadelphia,PA.

123.   McCormick, R.M., et al., *Microchannel electrophoretic separations of DNA in injection-molded plastic substrates.* Anal Chem, 1997. **69**(14): p. 2626-30.

124.   Anwar, K., T. Han, and S.M. Kim, *Reversible sealing techniques for microdevice applications.* Sensors and Actuators B: Chemical, 2011. **153**(2): p. 301-311.

125.   Hassanpour-Tamrin, S., A. Sanati-Nezhad, and A. Sen, *A simple and low-cost approach for irreversible bonding of polymethylmethacrylate and polydimethylsiloxane at room temperature for high-pressure hybrid microfluidics.* Scientific Reports, 2021. **11**(1): p. 4821.

126.   McDonald, J.C. and G.M. Whitesides, *Poly(dimethylsiloxane) as a Material for Fabricating Microfluidic Devices.* Accounts of Chemical Research, 2002. **35**(7): p. 491-499.

127.   Carrell, C.S., et al., *Sealing 3D-printed parts to poly(dimethylsiloxane) for simple fabrication of Microfluidic devices.* Analytica Chimica Acta, 2020. **1124**: p. 78-84.

128.   Sun, Y.S., *Comparison of Chip Inlet Geometry in Microfluidic Devices for Cell Studies.* Molecules, 2016. **21**(6).

129.   Atencia, J., et al., *Magnetic connectors for microfluidic applications.* Lab on a Chip, 2010. **10**(2): p. 246-249.

130.   Rafat, M., et al., *Fabrication of reversibly adhesive fluidic devices using magnetism.* Lab on a Chip, 2009. **9**(20): p. 3016-3019.

131.   Konda, A., et al., *Reconfigurable microfluidic systems with reversible seals compatible with 2D and 3D surfaces of arbitrary chemical composition.* Lab on a Chip, 2015. **15**(9): p. 2009-2017.

132.   Wang, W. and T.B. Jones, *Moving droplets between closed and open microfluidic systems.* Lab on a Chip, 2015. **15**(10): p. 2201-2212.

133.   Berthier, E., et al., *Open Microfluidic Capillary Systems.* Analytical Chemistry, 2019. **91**(14): p. 8739-8750.

134.   Wang, L., et al., *Steady flow of pressure-driven water-in-oil droplets in closed-open-closed microchannels.* AIP Advances, 2019. **9**: p. 125040.

135.   Feng, J. and J.P. Rothstein, *One-way wicking in open micro-channels controlled by channel topography.* Journal of Colloid and Interface Science, 2013. **404**: p. 169-178.